DYNAMICAL MODELING OF WATER TRANSPORT IN POLYMER ELECTROLYTE MEMBRANE FUEL CELL (PEMFC) DESIGNS

by
MUSTAFA FAZIL SERİNCAN

Submitted to the Graduate School of Engineering and Natural Sciences
in partial fulfillment of
the requirements for the degree of
Master of Science

SABANCI UNIVERSITY
Spring 2005

DYNAMICAL MODELING OF WATER TRANSPORT IN
POLYMER ELECTROLYTE MEMBRANE FUEL CELL DESIGNS

MUSTAFA FAZIL SERINCAN

APPROVED BY:

Dr. SERHAT YEŞİLYURT
(Thesis Advisor)

Dr. MEHMET ALİ GÜLGÜN

Dr. MAHMUT AKŞİT

DATE OF APPROVAL: 29.07.2005

Dynamical Modeling of Water Transport in Polymer Electrolyte Membrane Fuel Cell (PEMFC) Designs

Mustafa Fazıl Serincan

ABSTRACT

A two-dimensional finite element computational fluid dynamics (CFD) model, including coupled partial differential equations of mass, momentum and charge conservation inside a membrane electrode assembly of a polymer electrolyte membrane fuel cell (PEMFC) are developed. The CFD model is solved for PEMFCs with conventional and interdigitated gas flow fields. For the PEMFC with interdigitated flow fields both coflow and counterflow designs are studied. Furthermore a dynamic lumped model based on the formulation of Pukrushpan et al. (2003) is developed with the addition of membrane's transient water transport.

Models are validated by comparing the polarization curves with the experimental data of Ticianelli et al. (1988) for MEAs with conventional gas distributors and He et al. (2000) for MEAs with counterflow interdigitated gas distributors. The results of the lumped model and the CFD model for conventional design are shown to be comparable and lumped model proves to be a good substitute of CFD model for control studies. For the interdigitated case, coflow is found to be superior to counterflow in the performance of the cell. Transient and steady-state responses of the fuel cell system to changes in cell voltage, air pressure and relative humidity of air are investigated for each design. The effect of transient water transport is emphasized and it is observed that it plays a critical role in the operation of a PEMFC for both designs.

Polimer Elektrolit Membran Yakıt Hücresi (PEMYH) Tasarımlarında Su Geçişinin Dinamik Modellenmesi

Mustafa Fazıl Serincan

ÖZET

Polimer elektrolit membranlı yakıt hücresinin (PEMYH) membran elektrot birleşkesi içindeki kütle, momentum ve yük korunumu ile ilgili birbirine bağımlı kısmi türevli diferansiyel denklemler içeren, iki boyutlu hesaplamalı akışkanlar dinamiği (HAD) modeli geliştirilmiştir. HAD modeli geleneksel ve girişik kanal tasarımlı PEMYHler için çözdürülmüştür. Girişik kanal tipinde eş yönlü ve ters yönlü akış tasarımları incelenmiştir. Ayrıca membrandaki su geçişinin dinamiği de eklenerek Pukrushpan'ın formülasyonu üzerine kurulu bir noktasal model geliştirilmiştir.

Modellerden elde edilen polarizasyon eğrileri, Ticianelli'nin geleneksel tip yakıt hücresi ile ve He'nin girişik kanallı tip yakıt hücresi ile yaptıkları deney sonuçları ile karşılaştırılmıştır. Model sonuçlarının deney verileriyle örtüştüğü gözlemlenmiştir. Noktasal model sonuçlarının, HAD model sonuçlarıyla benzer olduğu ve noktasal modelin HAD modele iyi bir alternatif olabileceği gözlemlenmiştir. Girişik kanal tipli PEMYHlerde, eş yönlü akışın tersyönlü akışa oranla daha iyi performans sağladığı tespit edilmiştir. Farklı yakıt hücresi tasarımları için sistemin voltajdaki, hava basıncındaki ve havanın bağıl nemliliğindeki değişikliklere olan geçici rejim ve kararlı rejim cevapları incelenmiştir. Membranda su transferinin sistemin geçici rejim cevabına etkileri vurgulanmış ve bu etkilerin PEMYHnin çalışmasında önemli bir rol oynadığı gözlemlenmiştir.

“to my parents İrfan and Şefika for their

limitless efforts throughout my career”

ACKNOWLEDGEMENTS

I am grateful to Dr. Serhat Yeşilyurt for not only his valuable advises, but also his trust in my research capabilities. Studying with me on a particular problem for hours, proofreading my manuscripts, broadening my vision during the discussions and being available whenever I look for him, he has been more than respected.

I would like to thank Prof. Asif Sabanovic and Dr. Mustafa Ünel, for their supports when I had problems. Moreover, I express my gratitude to Dr. Mehmet Ali Gülgün who served as my juror.

From the very first days of my life, my parents who supported me both mentally and financially deserve the biggest appreciation.

Without my friends who were in touch with me whenever I needed, this thesis would totally be different. Server, Erdem, Çağdaş (of course), Okan (with his gentle hands), Teoman (with his rough hands), Shahzad (the Khan), Khalid (the deerest), Nusret, Burak, Mert and Cumhur are the ones whose assistance I will not forget.

TABLE OF CONTENTS

LIST OF TABLES

LIST OF FIGURES

LIST OF SYMBOLS

a	activity
A_{fc}	fuel cell active area
c	molar concentration
d	diffusional driving force
D	diffusivity
F	Faraday's constant
g	force per unit mass
i	exchange current density
I	current density
J	molar flux
k_a	anode transfer coefficient
k_a	cathode transfer coefficient
k_p	permeability
K	Henry's constant
m	molar concentration of total sulfonic acid groups
M	molecular weight
n	the direction normal to a surface
p	pressure
R	universal gas constant
t	time
T	temperature
u	velocity
V_{oc}	open circuit voltage
w	mass fraction
x	mole fraction
y	space coordinate
z	space coordinate

Greek

α	total water drag coefficient
β	reaction transfer coefficient
ε	fraction of a phase
ϕ	potential
γ	mass transfer coefficient
η	overpotential
κ	ionic conductivity
μ	viscosity
ρ	density
σ	electronic conductivity
τ	time constant

Superscripts

0	nominal
a	anode
c	cathode
eff	effective
sol	solute
T	total
w	water

Subscripts

+	proton
a	anode
c	cathode
ch	channel
d	diffusion
e	electrode
eo	electro-osmosis
g	gas
i	species
in	inlet

j	species
m	membrane
out	outlet
react	reaction
ref	reference
s	solid phase
sat	saturation
sh	shoulder
w	water

CHAPTER 1

INTRODUCTION

Recent awareness of environmental protection and fast growth of the world energy consumption has led public, policy makers, entrepreneurs, technology developers and scientists to search alternative means to carry and convert energy. Fuel cells are promising devices emerging as the substitutes for the conventional energy converters. Their superiorities concerning the environmental problems and high efficiency prop up the fuel cells to be employed for either small portable applications such as laptops and cell phones to large scale stationary applications for central heating facilities and electricity generation. As the fuel cell research advances, technological maturity and commercial viability of the fuel cell systems are imminent so as to facilitate a broad use of fuel cells in daily life.

A general overview of the fuel cells regarding the history, basic principles, types and characteristics will be discussed in this chapter. In this context polymer electrolyte membrane fuel cells (PEMFCs) will be emphasized.

1.1 Fuel Cell Overview

A fuel cell is an electrochemical energy conversion device that uses chemical energy to produce electricity. Like a battery electrodes are separated by an electrolyte in a fuel cell and electricity is generated due to the chemical reaction going on inside the cell. However, reactants are stored inside the battery thus, the performance of the battery decreases when the charge inside the battery drops until it eventually goes dead and needs to be recharged. On the other side reactants flow into the fuel cell continuously and the electricity is generated as the supply continues without recharging the cell.

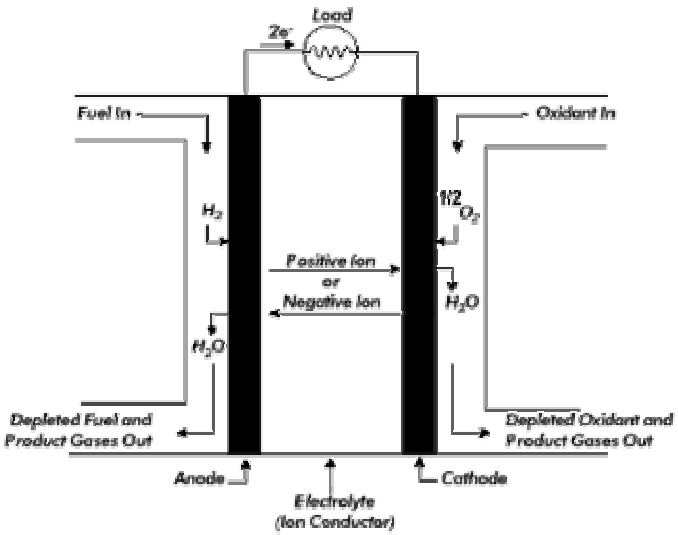

Figure 1.1: Schematic of a fuel cell [56]

A general cross-sectional view of a fuel cell is depicted in Figure 1. Fuel enters the negative electrode (anode) and oxidant enters the positive electrode (cathode) in gaseous state. Porous electrodes that allow the reactant gases to pass through are separated by an electrolyte. The chemical reactions occur at the electrode-electrolyte interface often with the help of catalysts especially for the oxidation reaction. Fuel entering the anode is separated into electrons and ions, which are protons when the fuel is Hydrogen. The ions pass through the electrolyte to the cathode side, while the electrons go through an external circuit connecting anode and cathode providing electricity. At the cathode ions combine with the oxidant and the electrons. The reaction taking place inside the cell produces a potential about 1 Volt. To get a reasonable voltage and current output, cells are combined in parallel and serial to form a fuel cell stack.

With respect to the electrolyte material different chemical reactions occur in the fuel cell and for particular reactions, different by-products are released besides heat. Types of fuel cells are defined by the electrolyte material, fuel and the conducting ions. Though each type of fuel cell has different properties, they share some characteristics. Energy conversion process from chemical reaction is common for all of them. Although other fuels such as methanol are used in fuel cells, hydrogen is used as the typical fuel. Finally each type of fuel cell stack generates direct current (DC) electricity.

1.2 History of Fuel Cells

The fuel cell effect was first discovered in 1838 by Christian Friedrich Schoenbein (1799 – 1868) a Swiss professor from the University of Basel. Schoenbein's description of the fuel cell effect first appeared in the English language in the January 1839 edition of "The London, Edinburgh, and Dublin Philosophical Magazine". After some experiments in 1839 William Robert Grove (1811 – 1896), a Welsh lawyer from the same university, first developed a fuel cell device. Grove's apparatus consisting of a platinum electrode immersed in nitric acid and a zinc electrode immersed in zinc sulphate took in hydrogen and oxygen to generate electricity and water. It generated a current of about 12 amperes at about 1.8 volts [8].

The term fuel cell was first used in literature in 1889 by Ludwig Mond and Charles Langer who attempted to build the first practical device using air and industrial coal gas. Chronologically the milestones of the fuel cell technology can be stated as:

- In 1886 William Jacques developed first fuel cell for household use.
- In 1900 Walther Nernst first used zirconia as a solid electrolyte.
- In 1932 Emil Baur constructed the first molten carbonate fuel cell.
- In 1930s Francis Bacon studied on alkaline electrolyte fuel cells while Emil Baur and H. Preis conducted experiments with solid oxide electrolytes.
- In the late 1950's NASA began experimenting with the technology to develop a power source for spacecrafts.
- In 1962 researches into solid oxide technology began to accelerate in the US and Netherlands; Allis-Chalmers Manufacturing Company demonstrated a 20-horsepower fuel-cell-powered tractor [8], [58].

The first fuel cells were too expensive for commercial success. In the early twentieth century with the development of the internal combustion engines which was a lower cost power source, the popularity of fuel cells declined. It had been 120 years since the discovery of the fuel cell effect when NASA was looking for a highly efficient power source for space flights and demonstrated some applications of fuel cells. [47] After this initiative, industry began to recognize the commercial potential of fuel cells. Being driven by technical, social and economic means and with the support from the governments, research and development of the fuel cell technology have been encouraged and many companies and research centers around the world are engaged with the technology.

Due to the environmental, economic and political concerns related to oil, coal and nuclear resources, growing energy demand and high mechanical integrity of conventional energy converters; fuel cells are seen as promising alternatives in unlimited number of applications thanks to their superior characteristics and nature friendly operation. Despite many potential benefits, the commercial deployment of fuel cells still faces many challenges such as high cost and the lack of hydrogen infrastructures. However, fuel cells are expected to be economically viable once the mass production begins, at least in the fields of distributed power generation and remote systems. [41]

1.3 Fuel Cell Applications

First application of the fuel cell systems was seen in Apollo and Gemini space programs where they are used to maintain electricity and drinking water for astronauts. More recently, three 12 kW Alkaline Fuel Cell (AFC) units have been used for at least 87 missions with 65,000 hours flight time in the Space Shuttle Orbiter [56]. Also they are expected to be used as regenerative power systems for space stations. Apart from this, terrestrial fuel cell applications can be mainly classified as stationary, portable and transportation applications.

1.3.1 Stationary Applications

Electricity generation for either buildings or rural areas, cogeneration systems and distributed power generation are some examples of stationary fuel cell applications. . Due to clean operation and low noise, fuel cells are niche applications especially for inner city buildings and hospitals. The power capacity of stationary plants is in the range of hundreds of kW to MW. Smaller plants (hundred kW to 1-2 MW) are used on-site and they are suitable for cogeneration operations which means the heat produced during the operation can be used in different thermal applications. Larger plants (1-10 MW) are used for distributed power generation. Hydrogen is generally supplied from natural gas or coal. Thus, the extant natural gas infrastructure can be used as fuel delivery. Many types of fuel cell operations have been demonstrated for stationary power generation.

The first commercial fuel cell plant PC-25 consisting of a 200 kW phosphoric acid fuel cell (PAFC) stack has been used for many on-site power generation applications in hospitals, hotels and manufacturing sites. This plant being an uninterrupted power supply provides independent power source and continuous power backup. The power quality is higher than that of conventional systems.

The heat produced during the fuel cell operation can be used in many applications. A promising one is the hybrid gas-turbine and solid oxide fuel cell (SOFC) where SOFC replaces the combustion chamber of a conventional turbine. The overall thermal efficiency of the system increased to 60% whereas it was 40% in a standalone gas turbine and 50% in the SOFC. Another cogeneration application is the incorporation of fuel cells in the site heating system in Toronto. Furthermore, Direct Fuel Cell claims that in a system of a molten carbonate fuel cell and a gas turbine, 70% efficiency is taken in the combined cycle [9].

Distributed power generation (DPG) is any small-scale power generation technology that provides electric power at a site closer to customers than central station generation. Fuel cells are capable to be used in DPG applications to provide thermal energy as a part of the cogeneration system, supply provide energy for remote locations where hook-up is difficult or expensive, solve quality and reliability problems, improve system efficiency, provide stand-by power during system outages and decrease power costs during on-peak periods. Typically the scale of the fuel cells used in DPG applications is less than 30 MW.

1.3.2 Portable Applications

Since fuel cells are modular devices they can be used in small portable applications as substitutes for batteries. The higher energy density characteristics of small fuel cells in comparison to batteries disclose the advantages of fuel cells in means of longer operation and higher power requirements of the devices. Thus, many device manufacturers have begun trying to integrate the fuel cell technology with the portable devices in order to wipe out the problem associated with the short battery life which is one of the biggest troubles they encounter.

Fuel cells have been used since 1960s in military portable applications. Though there had been few developments in the area until 1990s, since then it was estimated

that approximately 1700 operating systems in the power range of 1 W to 1500 W had been built as it was reported in a survey of 2002. [9].

Hitherto, PEMFCs have been used in portable applications most. However, direct methanol fuel cells show potential for the use in this area because hydrogen supply is methanol which is easier and safer to store.

Though there are many applications demonstrated the use of fuel cells in consumer electronics such as laptops and mobile phones, the commercialization of the systems are not completed due to the high cost of the systems and the regulations relating the distribution of them. Till the mass production begins portable fuel cell applications will be served to niche markets like military.

1.3.3 Transportation Applications

Low emission values, high efficiencies and simple mechanical integrities of fuel cells have been figure of merits to use them in light duty and heavy duty vehicle propulsion. Considering that in the United States, motor vehicles are responsible for 78% of CO, 45% of NO emissions and 37% of volatile organic compounds [57], the use of fuel cells in transportation applications alleviates the environmental problems like greenhouse effect and air pollution. Also taking into account the fact that consumption of oil by passenger vehicles exceeds all of the United State's domestic production, the search for an alternative propulsion system can be seen as an investment.

PEMFCs have been used widely for transportation applications because of their high power densities, high efficiencies, low corrosion characteristics and long cell and stack lives. With compared to internal combustion engine (ICE), PEMFC efficiency is higher at partial loads [34] and the efficiency at a nominal speed is two times higher in a cell with direct hydrogen feed from natural gas supply [40]. In a fuel cell energy stored in the chemical bonds are directly converted to electrical energy whilst in an ICE chemical energy is first converted to thermal energy and then it is converted to usable mechanical energy. Inclusion of the second process in ICE limits the efficiency of the system with Carnot Cycle. Thus, the efficiency of a fuel cell is greater than that of ICE. Further compared to the higher mechanical complexities of the conventional propulsion systems, the electricity generated in a fuel cell system can be used in motors then the motion can be transmitted easily to the wheels.

Transient behavior of the fuel cell vehicle for different power demands from the system in the presence of perturbations in the driving conditions is a key point in the context of replacing the ICE with fuel cell. The parameters affecting the fuel cell operation has to be optimized and necessary control schemes should be implemented in order to have a reliable operation during this transient. Thus, a fuel cell has to be integrated with other auxiliary systems to be used in automotive applications. The system integration will be discussed in the following sections.

1.4 Types of Fuel Cells

As mentioned earlier types of fuel cells are defined with respect to the electrolyte material. Types of fuel cells are explained briefly in this section. Each type has its own advantages and disadvantages making it proper for specific applications. A comparison of fuel cell types is shown in Table 1.1.

1.4.1 Polymer Electrolyte Membrane Fuel Cells (PEMFC)

In a PEMFC there is a proton conductor membrane sandwiched between two electrodes. For good conduction of the ions, membrane must be well humidified. By-product of the operation in this type is water and heat. Since the operating temperatures are low due limitations imposed by the polymer membrane, produced heat can not be used in cogeneration applications. Low temperature operation of PEMFC allows quick starts because of the shorter warm-up time and better durability due to the less wear on system components. However, high Pt catalyst loadings are required to promote the reactions at the operating temperatures. Moreover, the catalyst is sensitive to CO poisoning, thus pure hydrogen fuel is required. The following chemical reactions take place in the electrodes

Anode: $H_2 \rightarrow 2H^+ + 2e^-$

Cathode: $1/2O_2 + 2H^+ + 2e^- \rightarrow H_2O$

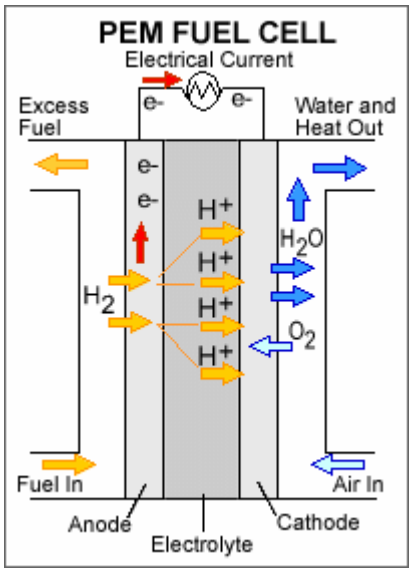

Figure 1.2: Schematic of a PEMFC [56]

Due to the fast startup time, low sensitivity to orientation, and favorable power-to-weight ratio, PEMFCs are preferred to be used in transportation applications. Currently, hydrogen storage is one of the technology issues limiting the use of PEMFCs in vehicles due to low energy density of hydrogen tanks (and other competing forms of on board storage) it is difficult for the vehicle to travel the same distance as the gasoline powered cars. In case of the utilization of hydrogen from higher energy density liquids like methanol or natural gas, onboard reformers must be used which increases cost, maintenance requirements and the complexity of the design. PEMFC will be discussed in details in section 1.6.

1.4.2 Alkaline Fuel Cell (AFC)

The electrolyte in this fuel cell uses a concentrated potassium hydroxide and can use a variety of non-precious metals as a catalyst at the anode and cathode. AFCs' high performance is due to the rate at which chemical reactions take place in the cell. They have also demonstrated high efficiencies in space applications. The reactions taking place in an AFC is,

Anode: $H_2 + 2(OH)^- \rightarrow 2H_2O + 2e^-$

Cathode: $1/2O_2 + H_2O + 2e^- \rightarrow 2(OH)^-$

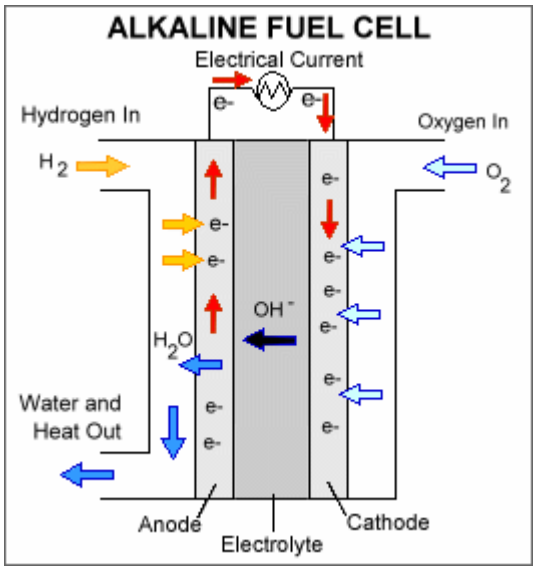

Figure 1.3: Schematic of an AFC [56]

The main problem encountered with AFCs is that catalysts can easily be poisoned by CO_2. Even small amounts of CO_2 in the air can poison the catalyst. Thus, air and hydrogen must be purified before they enter the cell. However, this process is expensive. Fuel cell's life is affected by the catalyst poisoning which will increase the costs. Up to 8000 hours of AFC stacks have AFC stacks have maintained sufficiently stable operation. However, they need to sustain the operation for at least 40000 hours to become economically viable, but that long operation has been regarded as impossible for AFCs due to material durability issues. This, being the most significant obstacle in commercializing this fuel cell technology, let AFCs only be used in niche applications.

1.4.3 Phosphoric Acid Fuel Cell (PAFC)

PAFCs also use liquid electrolyte. Phosphoric acid is contained in a Teflon-bonded silicon carbide matrix. As in PEMFC, the platinum catalyst is used to enhance the reaction. Chemical reactions taking place in PAFC is the same as those in PEMFC.

PAFC is the first fuel cell type that is used commercially for its technological maturity. As stated before the first stationary power generation application was established with a PAFC. Apart from stationary applications, PAFC is used in heavy duty transportation like city busses.

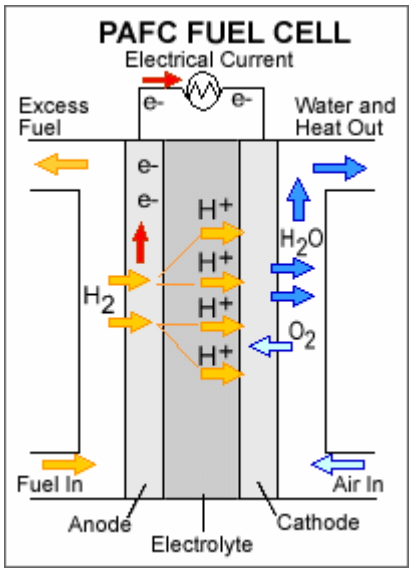

Figure 1.4: Schematic of a PAFC [56]

Effects of impurities in the fuel like CO poisoning are less in PAFC than that of PEMFC. Also, because the operating temperature is higher in this type of fuel cells, it is suitable for cogeneration applications thus PAFC can be utilized to be more efficient than PEMFC. However, the efficiency drops to 30 - 40% when the stack is used standalone. The main disadvantage of this fuel cell is that the power density is less than those of other fuel cell types. As a result, these fuel cells are typically large and heavy. PAFCs are also expensive because like in PEMFCs expensive platinum catalyst is used.

1.4.4 Molten Carbonate Fuel Cell (MCFC)

The electrolyte in this fuel cell is usually a combination of molten carbonate salt mixture suspended in a porous ceramic matrix of lithium aluminum oxide (LiAlO2). Alkali carbonates form a highly conductive molten ionic transfer salt at high operating temperatures of 600 to 700°C. At these temperatures Ni anode and NiO cathode is sufficient to promote reactions without any requisite of noble catalyst metals, reducing the cost. The reactions taking place in this type of fuel cell is

Anode: $H_2 + CO_3^{-2} \rightarrow H_2O + CO_2 + 2e^-$

Cathode: $1/2O_2 + CO_2 + 2e^- \rightarrow CO_3^{-2}$

Efficiency improvement in MCFCs is also another factor for cost reduction. Molten carbonate fuel cells can reach efficiencies approaching 60 percent, considerably higher than the 37-42 percent efficiencies of a phosphoric acid fuel cell plant. Cogeneration system efficiencies can rise up to 85%, by bleeding natural gas fuel to the exhaust of the fuel cell and feeding into a turbine.

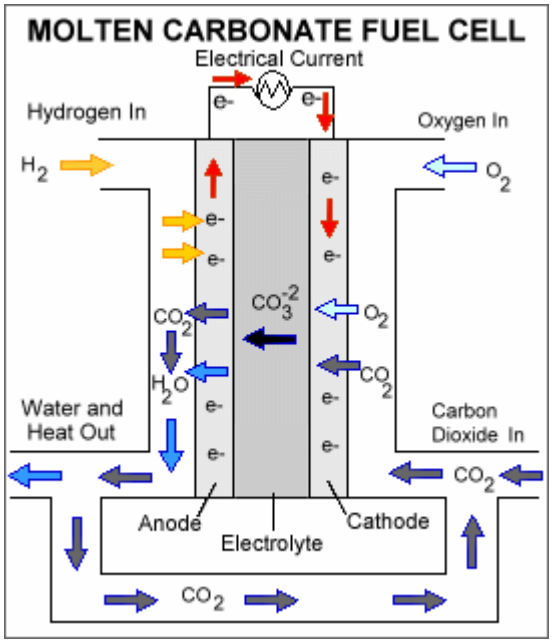

Figure 1.5: Schematic of a MCFC [56]

In the previous fuel cell types external reforming must be employed to produce hydrogen. However, in MFCFs, unlike alkaline, phosphoric acid, and polymer electrolyte membrane fuel cells, conversion to hydrogen can be carried out inside the fuel cell resulting in total cost reduction. MFCFs are less sensitive to impurities in the fuel like CO and CO_2 than the previous types. In fact, if the resistance of MCFC to other impurities such as sulfur is improved, even internal reforming of coal can be realized.

The tradeoff coming with the high operation temperatures is that while the high temperature enhances the efficiency and reduces the cost thanks to preclusion of noble metals, the corrosion and breakdown of the cell components decrease cell life. Corrosion-resistant materials for components and fuel cell designs are great interests of the researchers to increase cell life without decreasing performance.

1.4.5 Solid Oxide Fuel Cell (SOFC)

A Solid, nonporous ceramic compound, usually Y_2O_3 - stabilized ZrO2 electrolyte is employed in this type. Typically, the anode is Co-ZrO2 or Ni-ZrO2 cermet, and the cathode is Sr-doped LaMnO3. The governing reactions are,

Anode: $H_2 + O^{-2} \rightarrow H_2O + 2e^-$

Cathode: $1/2O_2 + 2e^- \rightarrow O^{-2}$

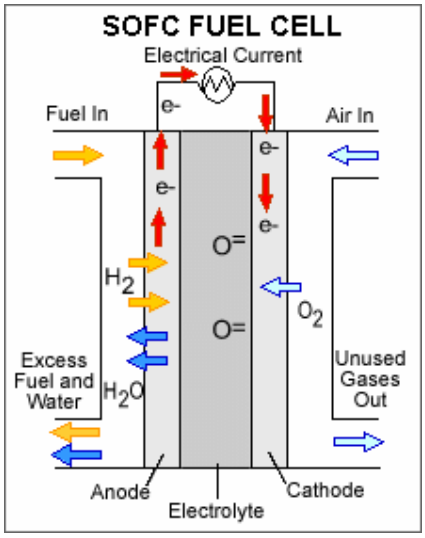

Figure 1.6: Schematic of a SOFC [56]

SOFC has the advantages of high operating temperatures such as high efficiencies, cogeneration capabilities and reduction of the cost due to the removal of the need for an expensive catalyst. Also the internal reforming capability should be appended in this perspective. In addition, the high resistance of SOFC to sulfur lets gases made of coal to be used within the fuel cell.

Along with the disadvantages listed for MCFCs, high temperature operation makes the startups of SOFCs slower. Also the safety requirements related to temperature makes SOFCs not convenient for transportation and portable applications. However they are acceptable for utility applications.

Scientists are currently exploring the potential for developing lower-temperature SOFCs operating at or below 800°C that have fewer durability problems and cost less. However, stack materials that will function in this lower temperature range have not been identified.

1.4.6 Direct Methanol Fuel Cell (DMFC)

Unlike the other types this type fuel cell does not use hydrogen as the fuel; instead methanol (CH_3OH) is fed directly to the anode where it is oxidized. DMFCs usually utilize a polymer electrolyte similar to proton-exchange membrane (PEM) fuel cells. An acidic electrolyte is necessary to reject the CO_2 that is produced during the electro-oxidation of methanol and because carbonate formation is a serious problem in alkaline solutions. The reactions in the cell are,

Anode: $$CH_3OH + H_2O \rightarrow CO_2 + 6H^+ + 6e^-$$

Cathode: $$3/2O_2 + 6H^+ + 6e^- \rightarrow 3H_2O$$

Since methanol is easily provided and transported using the extant infrastructure, DMFCs do not have fuel storage problems typical of the most types. Also the cost of the system is reduced because no reforming is needed though it operates at low temperatures and less catalyst is used.

Direct methanol fuel cell technology is relatively new compared to hydrogen air fuel cell technology. Technological maturity is not sufficient for commercial use. The main problem with this fuel cell is the higher system complexity. Besides a somewhat larger fuel cell, micro pumps and some controller functions are required [59]. Lastly, crossover of the methanol to the cathode side constitutes a cathode catalyst poisoning problem, which must be addressed to enhance DMFC's lifetime.

1.5 General Characteristics of Fuel Cells

The characteristics of fuel cells make them favorable to conventional energy converters in many applications. These characteristics which vary in different types of fuel cells determine the applications for they can be employed.

Efficiency: Direct conversion of the chemical energy to electrical energy is not limited by Carnot Cycle; hence, fuel cell stack efficiencies are greater than combustion type energy converters. Depending on the fuel cell type, stack efficiencies up to 50-60%

are available. If the surplus heat is utilized the efficiencies of the overall system up to 80-90% is realizable.

Power density: Higher power is maintained from a fuel cell which has the same size as that of a conventional energy converter, partly owing to higher efficiency.

Low emissions: When pure hydrogen is used, the fuel cell maintains zero emissions characteristics. However, in case of utilizing hydrogen from carbon-rich fossil fuels, oxides of nitrogen, sulfur and carbon are released; yet the emissions values are far below than those of conventional energy converters. Even when the hydrogen from natural gas is used in power, still due to higher efficiency of the conversion less CO_2 is released. For electrolysis, CO_2 emission does not constitute a problem.

Table 1.1 Comparison of the fuel cell types

Type	PEMFC	AFC	PAFC	MCFC	SOFC	DMFC
Electrolyte	Ion exchange membrane	Mobilized or Immobilized Potassium Hydroxide	Immobilized Liquid Phosphoric Acid	Immobilized Liquid Molten Carbonate	Ceramic	Ion exchange membranes
Mobile ion	H^+	OH^-	H^+	CO_3^{-2}	O^{-2}	H^+
Fuel	H_2, reformate	H_2	H_2, reformate	H_2,CO, CH_4	H_2, CO, CH_4	methanol, ethanol
Catalyst	Platinum	Platinum	Platinum	Nickel	Perovskites	Platinum
Operating temperature	60 - 80^{0}C	65 - 225^{0}C	~200^{0}C	~650^{0}C	800 - 1000^{0}C	~80^{0}C
Efficiency	25 - 35%	32 - 40%	35 - 45%	40 - 60%	45 - 55%	~20%
Power density	3.8 - 2.6 W/cm^2	0.7 - 8.1 W/cm^2	0.8 - 1.9 W/cm^2	0.1 - 1.5 W/cm^2	1.5-2.6 W/cm^2	~0.6 W/cm^2
Startup times	sec-min	Min	hours	hours	hours	sec-min
Applications	Electric utility Portable power Transportation	Military Space	Electric utility Transportation	Electric utility	Electric utility	Portable power Transportation
Stage of development	Commercially available	In use since 1960s	Commercially available	Demonstration	Prototype	Prototype
Advantages	Low corrosion Low temperature Quick startups	Cathode reaction is faster in alkaline electrolyte	Impure H_2 acceptable Less Pt needed	No noble metals needed Efficiency is improved	Less Pt needed Low corrosion Fuel flexibility High eff.	Direct feed of fuel Zero emission
Disadvantages	Cost of catalyst Sensitivity to fuel impurities	Expensive removal of CO_2 from fuel	Cost of catalyst Low power Large size	Thermal effects on cell component Corrosion Low power	Thermal effects on cell component	Higher system complexity

Reliability and availability: Since the only moving part in a fuel cell system is the auxiliary components and the integrity of a fuel cell to the system is simple, the maintenance requirements are reduced and the life of the fuel cell increase. Due to the low maintenance requirements, system availability increases. It is reported that a PC25 fleet consisting of more than 200 units have demonstrated 90% availability during 4 million operating hours [57]. Also power is available 99.9999% of the operating time. Reliability and lifetime fuel cells are limited by the catalyst performance in addition to occasional electrolyte failures. Fuel cell accidents do not pose hazards to the environment or to the public as much as nuclear reactors or fossil plants.

Thermal output and cogeneration capability: Depending on the type of the fuel cell, product heat can be utilized in means of domestic hot water applications or space heating. Also, in case of higher thermal outputs fuel cells can be used with other devices like turbines to enhance the system efficiency.

Size range: The output power from a fuel cell ranges between a few Watts to some Megawatts which gives flexibility of fuel cell for a broad range of applications.

Site flexibility: Fuel cells can be located in a variety of areas, indoor and outdoor, stationary and mobile, due to their quiet operation, zero to minimal emissions, reduced permitting requirements, and modularity.

Fuel flexibility: Direct hydrogen, direct methanol or reformed hydrogen from natural gas, methanol and different hydrocarbons can be used as fuel for different types of cells.

Despite these positive characteristics, there are also negative features of the fuel cells, such as high costs, insufficient infrastructure and immaturity of the technology.

1.6 Polymer Electrolyte Membrane Fuel Cell (PEMFC)

As stated before, being commercially available, PEMFC is the most used fuel cell type in a variety of applications. Competing with the ICE, incorporation of the PEMFC in transportation applications comes along with different challenges. Optimization of the operating conditions, transients of the system, robustness of the operation and system integration issues are the main concerns of the researchers in this context. This section is dedicated to give a broader perceptive about the design and operation of PEMFCs.

1.6.1 Design of the PEMFC

A PEMFC consists of two electrodes, a polymer electrolyte membrane, current collectors and gas flow fields. The combination of anode, electrode and cathode is referred as membrane electrode assembly (MEA).

1.6.1.1 Electrodes

All electrochemical reactions consist of two separate reactions: an oxidation half-reaction occurring at the anode and a reduction half-reaction occurring at the cathode. Both electrodes are porous structures. This property of the electrodes not only allows reactants to be transported easily but also increases the surface area and enhances the reaction rate. The electrolyte layer on the electrode surface is aimed to be sufficiently thin in order not to block the pores and impede the transport of the reactants to active sites. A stable three phase interface, consisting of gas, electrolyte and electrode surface is desired to be established. In case of an excessive amount of electrolyte is accumulated in the electrode, performance of the cell is reduced due to mass transport limitations.

The structure of the electrodes is composed of carbon black and polytetrafluoroethylene (PTFE). Pt catalyst is bounded to the high surface area carbon black which is an electronic conductor. PTFE is a hydrophobic material that lets the gases permeate inside the electrode. Depending on the surface properties of the material carbon black also acts like a wet-proofing agent. This composite structure establishes a stable three-phase interface in the electrode, which is regarded as the benchmark of PTFE bonding. An increase in the PTFE loading results in a decrease in the permeability of the liquid water and an increase in the volume fraction of the gas pores which then enhances the cell performance [4].

The only catalyst that reacts sufficiently with both H and O intermediates is Pt which has also high performance in releasing these intermediates. As in the anode half reaction, Pt first bond H atoms then release the intermediate as two protons and two electrons.

$$H_2 + 2Pt \rightarrow 2Pt - H$$

$$2Pt - H \rightarrow 2H^+ + 2e^-$$

Pt being the unique catalyst to be included in this process is an expensive material. The porous structure of the electrodes is favorable owing to the high surface area of carbon black.

1.6.1.2 Membrane

Membrane in PEMFC is a solid organic polymer usually polyperfluorosulfonic acid. The thickness of the membrane varies between 50 to 175 microns comparable to that of 2 to 7 sheets of paper. Nafion™ produced by DuPont is the most used membrane type. As in Nafion™, membranes have three regions: the Teflon™-like, fluorocarbon backbone which consists of lots of hundreds of repeating $–CF_2–CF–CF_2–$ units, the side chains, $–O–CF_2–CF–O–CF_2–CF_2–$, attached to the backbone and the ion clusters consisting of sulfonic acid ions, $SO_3^-H^+$.

Sulphonic groups, $-SO_3^-$, attached to the side chains are stationary. Protons can move in the presence of water in the membrane. Bonded to water molecules, protons can leap from one sulphonic group to another. This mechanism makes the membrane an ionic conductor in the presence of water.

The operating temperature of PEMFCs is limited by the range when the water remains liquid. Thus operating temperature of the cell is generally does not exceed 100^0C. In order to make the membrane not limited by the temperature, a new proton conducting mechanisms must be suggested.

Though it resembles a plastic wrap, selectively permeable membrane is relatively strong because of the Teflon™ backbone structure, and allows protons to pass through without mixing the reactants. Due to its organic nature, membrane does not conduct electrons, which is essential for the fuel cell operation.

1.6.1.3 Flow Fields and Current Collector Plates

A light weight, strong, gas permeable plate usually made of graphite or metals are pressed against the outer surface of the electrodes to serve as both current collector and gas flow field. Flow fields grooved on the plate have a big impact on the performance of the fuel cell which will be discussed in details in the following chapters. The width of the grooves also affects the produced current.

There are two flow field designs being used commonly in PEMFCs, conventional and interdigitated. As it is seen in Figure 1.7 in conventional flow fields, gases enter from the inlet port of the channel and it leave the cell from outlet port which is at the other end of the same channel. However in the interdigitated flow field design, the grooved channels are dead ended. Inlet and outlet channels are aligned like a comb. Thus, this design forces gases to flow from inlet to outlet through the porous electrodes resulting in a convection dominant mass transport, whereas in the conventional flow field diffusion was the motive force for mass transport. As it has been reported in the literature, when the fuel cell performance is considered interdigitated flow fields have some advantages over the conventional type.

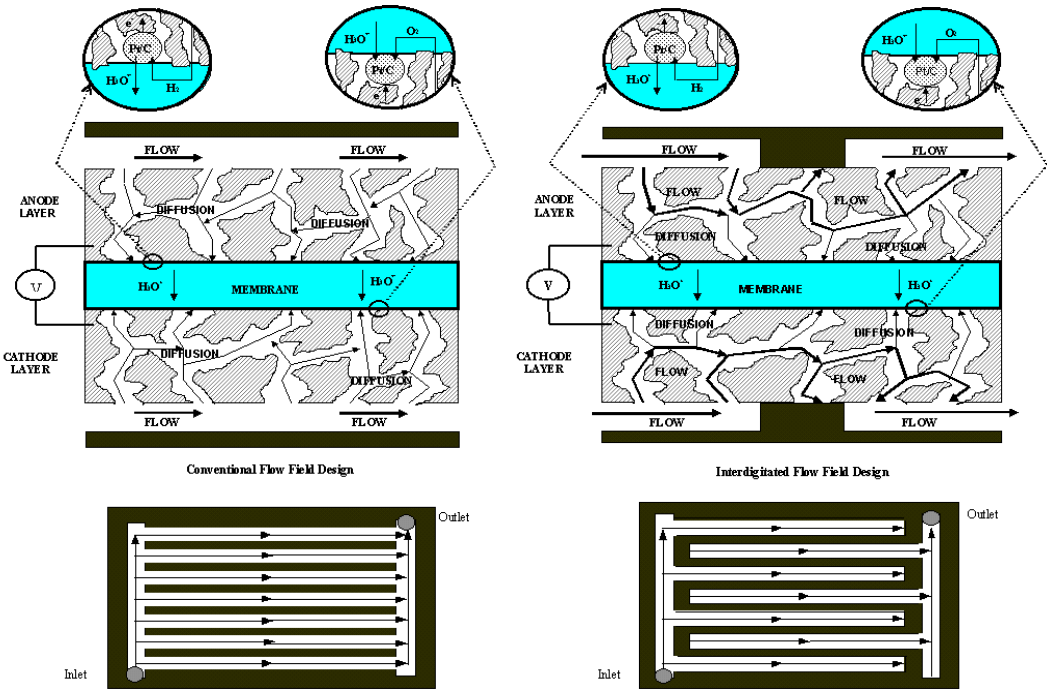

Figure 1.7: Conventional (left) and interdigitated (right) flow field designs. [60]

Also, with respect to the direction of the flow in the interdigitated flow fields, PEMFC designs are defined as coflow and counterflow. Considering that inlet and outlet channels of the anode are grooved just across the inlet and outlet channels of the cathode respectively, if both anode and cathode flow channels have the same direction from inlet to outlet, the design is called coflow else if the channels have the opposite direction, it is called counterflow.

1.6.2 Performance Issues

The operation of the PEMFC is dependent on many parameters, which strongly interact with each other. These parameters should be manipulated in order to sustain a desirable fuel cell operation. The main performance issues of the PEMFC operation are expressed as following.

Water management: Fuel cell operation and performance notably depend on water management. However there is a tradeoff for the water content in the fuel cell such that while membrane is desired to be humidified with liquid water, excess amount of liquid water on the electrode surface reduce the cell performance by clogging the pores. Thus water management in the membrane is one of the main concerns. Humidity values of entering gases and the liquid water generated during the reaction are the water sources which should be utilized well in order to maintain the reliable operation of the PEMFC.

Heat management: The exothermic reaction taking place inside the PEMFC, the irreversibility due to cathode over potential and the ohmic losses in the membrane and electrodes are the main heat sources during the operation. It is important to remove the heat from the system to maintain liquid water in the membrane and avoid the possible deformation of the cell components especially the membrane material. Homogenized temperature distribution is desired over the cell to keep away from thermal stresses, and local hot spots.

Power management: The power produced by the stack is used for the auxiliary components like the compressor which is used to increase the pressure of the air. Generally speaking, an increase in the air pressure also enhances the power output. Nevertheless, the parasitic power due to the compressor demand also increases, reducing the net power. Thus the air pressure should be utilized with respect to the power demand from the system.

Oxygen excess ratio: The ratio of the oxygen supplied to the oxygen depleted is known as the excess ratio and it is a key parameter in determining the cell performance. At different operating voltages, maximum power output is satisfied for an optimum value of the excess ratio. This should also be taken into account during the operation of the fuel cell.

1.6.3 System Integration

Among the various applications of PEMFC transportation applications have the main attraction. In order to be used in automotives PEMFC must be incorporated with many auxiliary components and systems. In Figure 1.8 the automotive fuel cell propulsion system laid out by Pukrushpan is seen. The control inputs u seen in the figure represent the control algorithms which take care of the performance issues stated in the previous section.

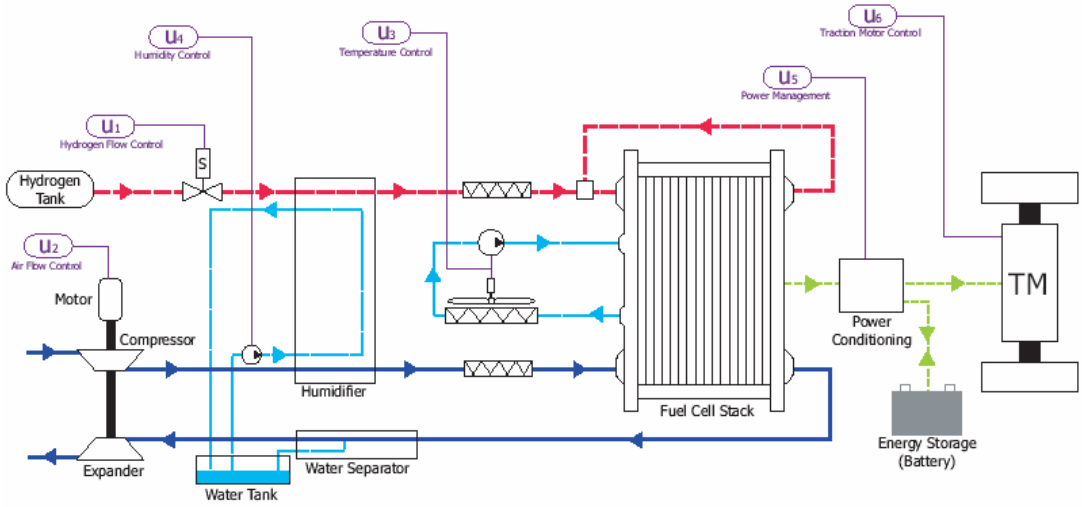

Figure 1.8: Automotive fuel cell propulsion system [37]

A compressor is used in the system to supply pressurized air to the fuel cell stack because in particular cases, it enhances the power output of the system. Since the temperature of the air increases during the compression process, a heat exchanger is used to reduce the temperature of the air entering the stack. Air entering the stack is humidified for water management purposes. Water produced at the stack is used in humidifiers after it is separated from the exhaust gases. On the other side, a valve is used to control the flow of hydrogen from the pressurized tank. Humidifier is to humidify the hydrogen entering the stack. Excessive heat is removed from the stack by using a deionized water coolant. To supply a suitable voltage for the traction motor and other system components, a power conditioner is necessary also.

The parameters affecting the system performance are utilized by the control systems taking care of reactants flow rates, humidity values of the reactants and temperature of the system. However, change in one parameter may affect another. For

example change in the pressure of the reactants varies the temperature and humidity of the gases entering the stack. The humidity of the membrane directly affects the output power. Also the temperature of the stack affects the rate of the chemical reactions and consequently the power produced. Thus, a robust control system is required to ensure the optimal values of these parameters so that degradation of the fuel cell performance is avoided.

CHAPTER 2

BACKGROUND ON MODELING

A detailed mathematical implementation is required to lay out the interactions between the mechanisms governing the operation of a fuel cell and to optimize the device in terms of performance, design, operating conditions and system integration. A combination of modeling and experimentation has reduced the cost and accelerated the pace of building and understanding fuel cell systems.

In the presence of a valid mathematical model, fuel cell systems can be analyzed to understand the governing physics inside the fuel cell and the performance issues like the electrical output, water and thermal management and reactant concentrations. As a result, system goals such as optimizing the system design and configuration, evaluating the power output and system efficiency, determining the sub-system requirements for system integration, understanding the system performance at various loads, assessing the controller performance and finding out the optimum operating conditions are comfortably achievable. Modeling is also expected to provide valuable information about the life prediction, stack structural and electrical reliability, electrochemical and mechanical degradation, and residual stresses due to fabrication which are key issues in reducing the cost of the fuel cell systems [26].

PEMFC modeling has been gaining interest as the hydrogen economy research is promoted by the governments and funding agencies. A number of modeling efforts related to PEMFC performance and design will be overviewed here in their own category and application area.

This chapter is organized in such a way that first the modeling efforts taking into account the dimensions will be discussed. Then, the studies which reflect on the design of gas flow fields used in PEMFC will be discussed. The latter one has significance to be mentioned because the design of the gas flow fields is a key feature of the thesis.

2.1 Dimensional Complexity in Modeling Efforts

2.1.1 Lumped Models

In lumped models system dynamics are studied while the spatial deviations of the variables are neglected. Constructed by only ordinary differential equations, this kind of models need relatively low computational effort and are good for practical modeling of the system dynamics and control applications.

Pukrushpan and Stefanapolou (2003) [18], [37], [38], [39],

In the lumped model of Pukrushpan et al. temperature is assumed to be controlled perfectly so that the processes in the system are isothermal. Water is assumed to exist in the fuel cell only in vapor phase and the gases are fully humidified. Differential equations relating the mass transport are written by simple mass balances such that rate of change of the mass inside a control volume is equal to the net mass flow rate entering the domain. Concentrations of reactants are obtained by using ideal gas law and they are used in the electrochemical relations that define the cell potential. Water transport in the membrane is employed as a diffusion equation with a source term that is lumped over the membrane. However, dynamics of the water transport inside the membrane is neglected.

The model is used to show the basic characteristics of a PEMFC and the effects of the parameters on the system performance. In this study a fuel cell stack is investigated at the system level rather than a single cell and the models of auxiliary components are also included. The model is used in a control simulation in which the oxygen amount that is depleted in the operation and the current demand form the power management system is regulated to achieve the desired power output as well as to avoid oxygen starvation problem, which is seen in case of insufficient oxygen supply and reduces the life of the stack.

Yerramalla et al. (2003) [54]

In this study, both a nonlinear and a linearized model of a PEMFC are developed based on the energy, mass and electrochemical equations similar to those of Pukrushpan's. In the linear model PEMFC is represented by a transfer function. Simulations are carried out for the variations in the inverter load. Similar results are

taken for both nonlinear and the linear model. It is concluded in this study that for the varying currents from the inverter load, voltage response has fluctuations which might cause problems when PEMFC is used as a major power source. The need for a control action is emphasized in the study. Also it is addressed that due to the leakage currents between the internal cells of a stack voltage output is not smooth.

2.1.2 One Dimensional Models

Springer, Zawodzinski, Gottesfeld (1991) [44]

In this study, an isothermal, steady state model of a MEA for a PEMFC is used. The study is supported with experiments. Many well-known expressions for the PEMFC parameters such as membrane water content, water diffusion coefficient and electro-osmotic drag coefficient, which are used in the literature frequently, are stated from the results of these experiments. Single phase of water is assumed in the study and an equilibrium condition between the membrane water and the water vapor in the electrodes are supposed. The model gives useful information about the water transport in the membrane and its effects on the cell performance. The main conclusion is that the convective water transport in the membrane is limited to the drag force of protons on water molecules. It also predicts an increase in membrane resistance for higher currents. Water profiles through membrane thickness are also obtained from the model.

Bernardi and Verbrugge (1992) [5]

On the basis of their previous model in 1991 a more rigorous one is developed for a PEMFC taking into account the electrodes, catalyst layers and the membrane. This model is isothermal and steady state. Liquid phase of the water is taken into consideration besides the vapor phase. While modeling the water transport in the membrane, drag force on the water molecules is not accounted. The simulations are done for two types of membrane. It is claimed that evolutions of gas and liquid pressures differ due to the capillary forces. In this study the factors that limit the fuel cell performance are outlined and it is asserted that the volume fraction of the pores in the electrodes must be more than 20% in order to avoid undesired performance degradations. The model is also used to explain the species transport in the network of solid, liquid and gas phases. Catalyst layer utilization is discussed for different

operating current density values and it is concluded that for higher current densities approximately 10% of the catalyst is utilized.

2.1.3 Two Dimensional Models

Nguyen and White (1993) [33]

A steady state, non isothermal, two phase model is developed to study the water and heat management in a PEMFC consisting of flow channels and MEA. Efficacies of different humidity values of the inlet gases are investigated. Water transfer across the membrane is calculated as the difference between the electro-osmotic drag and the diffusion. Liquid water is assumed to exist in small droplets so that obstruction of reactants due to the liquid water is neglected. Heat transfer from the solid phase to gas along the flow channels is also incorporated. Though the model is mentioned as non-isothermal, the temperature of the electrodes, plates and the membrane is assumed to be uniform and constant due to the high thermal conductivities of solids. Current is given as the input and cell potential is calculated as the difference between the open circuit voltage and the voltage losses. Overpotential is assumed to be distributed over the cathode membrane boundary as a function of oxygen concentration. The main conclusion of this study is that inlet gases should be humidified in order to minimize the ohmic loss, which is prevailing at relatively higher current densities because the water diffusion is insufficient to hydrate the membrane.

Fuller and Newman (1993) [17]

A steady-state, single phase, non-isothermal model is developed for the MEA. Water and heat management and utilization of fuel are examined. It is claimed that produced in gaseous phase at the catalyst surfaces. The limit of validity of the model is that there should be no condensation of water within the catalyst layer. Analysis is held for both isothermal and non-isothermal cases. Water and thermal managements are interrelated to consider the dependence of the equilibrium sorption of water between the membrane and the gas phase. The importance of the heat removal is stated to be a critical parameter in the operation of the PEMFC.

Um, Wang and Chen (2000) [48]

In this study, a CFD based transient, isothermal, single phase model is developed. Though it is a transient model, steady state analysis is carried out more than dynamic analysis. In the model, a single set of differential equations valid for flow channels, electrodes, catalyst layers and the membrane is developed. The differences of the governing physics are taken into consideration by the sink and source terms in the equation system. The model equations account for continuity, species conservation, momentum conservation and the charge conservation. Effects of the reactant concentrations are shown on polarization curves. Distributions of the variables inside the MEA are sketched. The model is also used to simulate the hydrogen dilution effects on the system performance in the presence of impurities in the anode gas.

Berg, Promislow, St. Pierre, Stumper, Wetton (2004) [3]

A steady state, isothermal model is developed. No phase change of water is taken into consideration. However, water transport from gas phase in the electrode to liquid phase in the membrane is implemented in a novel way different than extant methods. Non-equilibrium kinetics of the membrane electrode interface is the key feature of the model. A water flux across the membrane which is proportional to the difference between the equilibrium sorption values and the local water content is considered rather than assuming equilibrium on the water content. To develop a reliable model, some parameters of the PEMFC like exchange current density and water mass transfer coefficient which is introduced in this model to associate with the non-equilibrium kinetics are fit to a set of data. The effects of these parameters on the polarization curves, distributions of reactant concentrations and current densities are examined and the results are compared with the experimental data. The main results are that a majority of current is produced at the reaction sites in the membrane and oxygen diffusion in the membrane water has significant effects on mass transfer losses.

2.1.3 Three Dimensional Models

Berning, Liu, Djilali (2002) [6]

Incorporating gas flow channels and the MEA, a non-isothermal, steady state, single phase CFD model is developed. The model takes into account for all major

transport phenomena without the phase change of the water. In the modeling of water transport through the membrane, Schlögl equation is used which takes into account a convective term due to the pressure gradient across the membrane apart from diffusion and electro-osmotic drag. Like in most of the previous models in the literature electrochemistry in this model also relies on the first order kinetics and empirical data. Simulations are presented with an understanding of 3D distributions of concentrations, current densities, temperatures and water flux. Temperature differences of a few K degrees are observed within the MEA. 3D effects are experienced especially under the collector plates land area and it is seen that it has significant effects on current distribution and limiting current density.

Wang and Wang (2005) [52]

A CFD based transient, isothermal, single phase model is developed. The regions accounted in the model are the flow channels, electrodes, catalyst layers and the membrane. Like in the model of Um et al. a single domain approach is used while building the equation system and sink and source terms are used to account for the different phenomena in different regions of the fuel cell. Time scales are estimated for diffusion of the species in the electrodes, water transport across the membrane and charging of the electrochemical double-layer. It is observed with both time scales and simulations that the transient associated with the membrane water transfer is dominant and the other transients are negligible compared to it. Overshoot and undershoot dynamics are explained on the basis of simulations. Dynamic responses in average current density to various changes in cell voltage and inlet humidity of the air is outlined. Also the evolutions of water profiles are depicted.

2.2 Modeling Efforts Considering the Design of Flow Fields

As it was discussed in the previous chapter, the design of the gas flow fields has significant effect on the performance of the fuel cell. However, modeling efforts so far mainly consider the conventional flow fields design. Modeling efforts considering the interdigitated flow fields which is a relatively more novel design, has not reached the maturity yet and many of the modeling techniques that have been used for the conventional design is not implemented for interdigitated flow fields yet. Some of the

models that give useful information about this novel design and some models that compare both designs are cited below.

Kazim, Liu and Forges (1999) [25]

A two dimensional, steady state, isothermal model of the cathode is developed to compare the performance of a PEMFC with both conventional and interdigitated flow fields. Water management is not included in the model. Same equation system is used for both designs and boundary conditions are changed in order to associate with each one. The results show that the limiting current density of a PEMFC with interdigitated flow fields is three times more than that of the fuel cell with conventional flow fields due to mass transfer enhancements. It is also observed that interdigitated design doubles the maximum power density of a PEMFC with conventional flow field design.

Yi and Nguyen (1999) [55]

In this two dimensional, isothermal, single phase, steady state model only the cathode of a PEMFC with interdigitated flow fields are taken into account. Similar governing equations are used as the ones in the models for conventional designs. Since the model does not cover the membrane estimated values of parameters considering the water transfer is used. Steady state simulations are carried out to outline the distributions of current density and oxygen concentrations and the effects of differential pressure on these variables. It is experienced that diffusion layer is greatly reduced by the forced convection inside the cathode. However, diffusion is found to play a significant role in reactant concentration distribution. It is also observed that with the higher gas flow rates, thinner electrodes and narrower shoulder widths, the average current density generated at the cathode increases.

He, Yi and Nguyen (2000) [23]

Again the only cathode of the PEMFC is modeled in this study. The difference of the model from the previous one is that it accounts for the phase change of water in the cathode. The effect of the liquid water on the volume fraction of the pores is handled with a normalized parameter and the porosity is assumed to be a function of this parameter. It is concluded that higher pressure differences over the cathode results in an effective way of liquid water removal. Different than the previous one, mainly discussing the optimal design of the flow fields, this model suggests that electrode

thickness should be optimized because thinner electrodes may reduce the gas flow rate. With an addition to the conclusion of the previous model on the shoulder sizes, in this study it is suggested that flow fields should be designed with more shoulders. In this study experiments are conducted with an interdigitated gas distributor and the model is validated with the experimental data.

Hu, Fan, Chen, Liu, Cen (2004) [24]

A three dimensional, isothermal, steady state model is developed to compare the performance of both flow field designs. No phase change is considered in the model. All the regions of the fuel cell are incorporated. Three dimensional distributions of the variables and flow fields in each case are outlined. Similar results of Kazim et al. are obtained. Also it is stated in this study that the higher pressure drop inside the electrodes is the main obstacle in front of the interdigitated flow field design.

Wang and Liu (2004) [51]

A three dimensional, non-isothermal, steady state model is developed to carry out a parametric study along with the experiments. Phase change of water is not included. It is concluded in the steady state analysis that the increase in the pressure enhances the PEMFC performance when the sufficient humidification is supplied; otherwise the increase in the temperature deteriorates the performance. Also, it is asserted that unlike in the conventional design, humidification an increase in temperature of the anode and cathode gases improves the fuel cell performance until the temperature is 20^0C above the cell temperature.

2.3 Modeling Approach and Contribution in this Thesis

Considering the models stated above, which serve as a basis for the other ones in the literature, it can be seen that most of the studies that account for spatial variations are for steady-state. A rigorous dynamic analysis of a PEMC lacks in the literature for the interdigitated flow fields. Also for the conventional design there are much less transient models than the stationary ones.

Water management in a PEMFC is employed in these models as either equilibrium kinetics or non-equilibrium kinetics model. In both cases, a diffusive, an electro-osmotic and a convective term may exist in the equation governing the water transport

through the membrane. However in certain cases, this equation can be simplified by neglecting the recessive term.

Water management has not been carried out rigorously for interdigitated flow field design. The ones with simple water transport models all assume the equilibrium-kinetics. Also, transient analysis of non-equilibrium kinetics has not been studied yet either for conventional or for interdigitated design.

The thesis, emphasizing transient modeling and non-equilibrium water management for the interdigitated flow field design will more than likely to have valuable contribution to the literature.

CHAPTER 3

MATHEMATICAL MODEL

While developing the model the anode, the cathode and the membrane of a PEMFC are considered as three distinct subdomains and conservation of mass, conservation of momentum and conservation of charge equations are used in these subdomains to associate with the physical phenomena in the cell. A two dimensional computational fluid dynamics (CFD) model is developed along with a zero dimensional lumped model. The CFD model is used for both conventional and interdigitated flow fields by imposing appropriate boundary conditions. With the same reasoning two different designs for interdigitated flow fields taking into account the direction of the flow are analyzed.

3.1 CFD Model Definition

Maxwell-Stefan equations, (in the form developed by Curtiss and Bird (1999)) are used to model the transport of reactants in the electrodes. Darcy's equation for momentum transfer and Ohm's Law of electronic and ionic conduction are used in the electrodes and in the membrane. Water transport in the membrane including electro-osmotic drag and back diffusion is modeled.

3.1.1 Governing Equations

3.1.1.1 Gas Diffusion Electrodes

Conservation of momentum

The conservation of momentum in the porous gas diffusion electrodes can be approximated as Darcy's Law which replaces the equations of continuity and motion.

$$\frac{\partial}{\partial t}(\rho\varepsilon_g) + \nabla.(\rho\varepsilon_g \boldsymbol{u}) = 0 \tag{3.1}$$

$$\boldsymbol{u} = -\frac{k_p}{\mu}\nabla p \tag{3.2}$$

where ε_g is the porosity, the ratio of pore volume to total volume, k_p is the permeability of the porous electrode, ρ is the density of the mixture and μ is the viscosity of the fluid. $\boldsymbol{u}$ is the superficial velocity, which is defined as the volume rate of flow through a unit cross-sectional area of the solid plus fluid, averaged over a small region of space. This region is small with respect to the dimensions of the flow system but large with respect to the pore size. Darcy's equation is proposed empirically to describe the slow seepage of fluids through granular media by homogenization of the porous and fluid media into one single medium so that detailed geometric description of the pore structure is not required [20].

Conservation of mass

Momentum balance is coupled with mass balance through Maxwell-Stefan equation which is a better approximation than Fick's Law for interdiffusion of species and multicomponent transport. Fick's Law is based on the assumption that species dissolved in a solution only interact with the solvent. However, in a solution the solvent is affected by the solute species and they interact with each other.

In binary diffusion the movement of any species is proportional to the negative of the concentration gradient of this species. In multicomponent diffusion other interesting things can arise such that (i) the species can move against its concentration gradient known as reversed diffusion, (ii) the species can move in the absence of its concentration gradient called osmotic diffusion and (iii) the species may not diffuse though its concentration gradient is nonzero.

Maxwell-Stefan equations are shown to be a very good approximation for multicomponent diffusion in gases *at low density* [27], [10]. Indeed it is shown to be a better approximation than Fick's Law such that Fick's Law underestimates the fluxes for multicomponent transport by 5-10% [1].

In this model the formulation of the Maxwell-Stefan equations that is derived by Curtiss and Bird is used. In their study, Curtiss and Bird suggested different diffusivities to validate the equations for dense gases, liquids and polymers [11]. Unlike the

conventional one, their formulation incorporates the pressure dependence and the temperature dependence (Soret effect) of the concentration gradient of the species. The formulation is briefly explained as following:

The mass balance for each species, except one, in a solution is given by the general transport equation,

$$\frac{\partial}{\partial t}(\rho \varepsilon_g w_i) + \nabla.(\boldsymbol{j_i} + \rho w_i \boldsymbol{u}) = 0 \tag{3.3}$$

where w_i is the mass fraction of the species. The second term in this equation is the combined mass flux consisting of molecular mass flux vector $\boldsymbol{j_i}$ and the convective mass flux vector. With the thermodynamics of irreversible processes $\boldsymbol{j_i}$ is defined as

$$\boldsymbol{j_i} = -D_i^T \nabla(\ln T) - \rho w_i \sum_{j=1}^{N} D_{ij} \boldsymbol{d}_j \qquad \text{(i=1,2,…,N)} \tag{3.4}$$

where D^T is the thermal diffusivity, T is the temperature, D_{ij} is the symmetric diffusivities proposed by Curtiss and $\boldsymbol{d_j}$ is the difusional driving force for the species j which is defined as

$$\boldsymbol{d_i} = \frac{1}{cRT}\left(\nabla p_i - w_i \nabla p - \rho w_i \boldsymbol{g_i} + w_i \sum_{j=1}^{N} \rho w_j \boldsymbol{g_j} \right) \tag{3.5}$$

where c is the concentration of the mixture, R is the universal gas constant and $\boldsymbol{g_i}$ is the force per unit mass acting on the ith species. The first two terms on the right side describe the effects of the intermolecular forces, and the last two terms describe the effects of the external forces. If the only external forces are gravity forces, the last two terms cancel each other. Noting that from the ideal gas law $p = cRT$ and the mole fraction of the species i is

$$x_i = \frac{p_i}{p} \tag{3.6}$$

[3.5] can be written as

$$\boldsymbol{d_i} = \left(\nabla x_i + (x_i - w_i)\frac{\nabla p}{p} - \rho w_i \boldsymbol{g_i} + w_i \sum_{j=1}^{N} \rho w_j \boldsymbol{g_j} \right) \tag{3.7}$$

Finally with the assumptions that the process is isothermal and there is no external force acting on the species apart from the gravity forces, final transport equation can be written as

$$\frac{\partial}{\partial t}(\rho \varepsilon_g w_i) + \nabla . \left[-\rho w_i \sum_{j=1}^{N} D_{ij} \left\{ \left(\nabla x_j + \left(x_j - w_j \right) \frac{\nabla p}{p} \right) \right\} + \rho w_i \boldsymbol{u} \right] = 0 \tag{3.8}$$

This equation is the generalized form of the Maxwell's idea that concentration gradients result from the friction between the molecules of different species. Maxwell suggested this idea for binary mixtures on the basis of kinetic theory and Stefan generalized them to describe the diffusion in a gas mixture with N species. The formulation above, suggested by Curtiss and Bird, is developed using kinetic and continuum theory incorporated into Jaumann's entropy balance equation [11].

The model takes into account two species in the anode as H_2 and H_2O and three species in the cathode as O_2, H_2O, and N_2. Equation (3.8) is solved for mass fraction of H_2 at the anode and mass fractions of O_2 and H_2O at the cathode. Mass fractions of H_2O at the anode and N_2 at the cathode are calculated via,

$$\sum_i w_i = 1 \tag{3.9}$$

In the Maxwell-Stefan equation ρ is the density of the mixture given by

$$\frac{1}{\rho} = \frac{\sum_i \frac{w_i}{M_i}}{p/(R.T)} \tag{3.10}$$

The symmetric diffusivities in the Curtiss-Bird formulation can be determined from Maxwell-Stefan diffusivities $\tilde{D}_{ij}$ which are used in the conventional formulation. For a nominal value at reference conditions Maxwell-Stefan diffusion coefficients,

which depends only on the intermolecular force for the binary pair of gases, can be extrapolated for any operation temperature and pressure as,

$$\widetilde{D}_{ij} = \widetilde{D}_{ij}^{0}(p_0, T_0)\frac{p_0}{p}\left(\frac{T}{T_0}\right)^{1.5} \tag{3.11}$$

The nominal values at reference temperatures and pressures are listed in Table 3.1. To account for the porosity an effective diffusion coefficient is calculated with a Bruggeman type relation [7],

$$\widetilde{D}_{ij}^{eff} = \widetilde{D}_{ij}\varepsilon_g^{\,1.5} \tag{3.12}$$

Defining

$$C_{ij} = \frac{x_i x_j}{\widetilde{D}_{ij}^{eff}} \tag{3.13}$$

the relation between symmetric diffusivities and the Maxwell Stefan diffusivities is given as,

$$C_{ij} = w_i w_j \frac{\sum_{k\neq i}(adjB_i)_{kj}}{\sum_{k\neq i} D_{ij}(adjB_i)_{kj}} \tag{3.14}$$

where the matrix $(B_i)_{kj} = -D_{kj} + D_{ki}$. The explicit expressions are listed in Table 3.2. for binary and ternary systems. It should be noted that due to the symmetry $D_{ij} = D_{ji}$ and additional entries to this table may be generated by cyclic permutations of the indices.

Table 3.1 Maxwell-Stefan diffusivities at reference temperatures and 1 atm [7]

Gas Pair	**Reference Temperature T_0**	**Binary diffusivity constant (m^2/s)**
H_2 - H_2O	307.1	0.915×10^{-4}
O_2 - H_2O	308.1	0.282×10^{-4}
O_2 - N_2	293.2	0.220×10^{-4}
H_2O - N_2	307.5	0.256×10^{-4}

Table 3.2 Explicit relations between the symmetric diffusivities and the reciprocal of the Maxwell Stefan diffusivities.

Binary	$D_{11} = w_2^2 / C_{12}$ $D_{22} = w_1^2 / C_{12}$ $D_{12} = - w_1 w_2 / C_{12}$
Ternary	$D_{11} = [w_3^2 C_{12} + w_2^2 C_{13} + (w_2 + w_2)^2 C_{23}] / \Delta_3$ $D_{12} = [w_3^2 C_{12} - w_2(w_1 + w_3) C_{13} - w_1(w_2 + w_3) C_{23}] / \Delta_3$ $\Delta_3 = C_{12}C_{13} + C_{12}C_{23} + C_{13}C_{23}$

Conservation of charge

For the charge conservation in the conductive media at the electrodes Ohm's Law is used.

$$\nabla.(-\sigma^{eff} \nabla \phi_s) = 0 \tag{3.15}$$

where ϕ_s is the electric potential of the solid phase. Current density can be found as

$$\boldsymbol{I}_s = -\sigma^{eff} \nabla \phi_s \tag{3.16}$$

Since not whole of the electrodes are conductive, an effective conductivity is used which is defined as,

$$\sigma^{eff} = \sigma \varepsilon_s^{1.5} \tag{3.17}$$

where ε_s is the volume fraction of electronically conductive solid in the electrodes.

3.1.1.2 Membrane

The main governing equation in the membrane is the transport of the water. There are two distinct mechanisms that govern the transport of water in the membrane [33], [44]: (i) electro-osmotic drag due to protons from anode to cathode; (ii) diffusion due to a concentration gradient inside the membrane. When the current is drawn from the cell, protons move from anode to cathode through the membrane and water molecules are

carried by protons. This process is called the electro-osmotic drag and average number of water molecules carried by one proton is called electro-osmotic drag coefficient. When the water concentrations are different at the anode and the cathode there is a concentration gradient which drives the diffusion of the water molecules from higher concentration sites to lower concentration sites.

Total mass flux of water transported inside the membrane is defined as

$$\boldsymbol{J}_{\boldsymbol{w}}^{\boldsymbol{T}} = \boldsymbol{J}_{\boldsymbol{w}} + \boldsymbol{J}_{+} = -m.D_w \nabla c_w + n_d \frac{\boldsymbol{I}_{\boldsymbol{m}}}{F} \tag{3.18}$$

where $\boldsymbol{I}_{\boldsymbol{m}}$ is the local current density in the membrane, c_w is the normalized molar fraction of water with respect to the concentration of total sulfonic acid groups in the membrane, m is the molar concentration of total sulfonic acid groups and is defined as

$$m = \frac{\rho_m}{M_m} \tag{3.19}$$

where ρ_{mem} is the density of the dry membrane and M_{mem} is the molecular weight of the dry membrane. D_w, water diffusivity, and n_d, electro-osmotic drag, are dependent on water content c_w and the expressions for them are provided in Table 3.3 for Nafion membranes.

In [3.18], the first term represents the so called back-diffusion and the second term stands for electro-osmotic drag. Conservation of mass for water implies that

$$\frac{\partial}{\partial t}(\varepsilon_m .m.c_w) + \nabla .\boldsymbol{J}_{\boldsymbol{w}}^{\boldsymbol{T}} = 0 \tag{3.20}$$

where ε_m is the water fraction in the membrane.

Most of the models in the literature imposed equilibrium water sorption value, a function of water activity, as the boundary condition [33], [44], [52]. However, water exists in liquid phase in membrane whereas it is assumed to exist in vapor phase in the electrodes. Thus, as suggested by Berg et al. [3] to incorporate the phase change of water, a two mode water transfer mechanism is used in the membrane assuming that the flux in and out of the membrane is proportional to the differences between the local

water content and equilibrium sorption values. This will be discussed in details in the following section.

Time Scales

Time scales associated with diffusion and electro-osmotic term can be estimated by equating rate of change in 3.18 to water production related to the corresponding term. For diffusional time scale

$$\varepsilon_m m \frac{\Delta c_w}{\tau_d} = \frac{m.D_w \frac{\Delta c_w}{t_m}}{t_m} \tag{3.21}$$

$$\tau_d = \varepsilon_m \frac{t_m^{\,2}}{D_w} \tag{3.22}$$

With the parameters used for the conventional design, time scale is found to be around 4-8 s for membrane water contents of 14 and 7 respectively. Diffusional time scale can be used to estimate the transients of species transport at the electrodes.

$$\tau_e = \frac{t_e^{\,2}}{D_g} \tag{3.23}$$

For the diffusivities of gases at the order of 10^{-5} m^2/s, time scale is estimated at the order of 0.01 s which is negligible with respect to the time scale of water transport.

Equating the rate of change to the electro-osmotic term

$$\varepsilon_m m \frac{\Delta c_w}{\tau_{eo}} = \frac{n_d \frac{I}{F}}{t_m} \tag{3.24}$$

$$\tau_{eo} = \frac{\varepsilon_m m \Delta c_w t_m F}{n_d I} \tag{3.25}$$

With the parameters used for the conventional design, at a constant current density I = 1 A/cm^2, time scale is found to be around 4-5 s for membrane water content increasing from 10 to 14.

In the membrane the conduction of protons are modeled using the Ohm's Law for the conservation of charge:

$$\nabla.(-\kappa\nabla\phi_m) = 0 \tag{3.26}$$

where ϕ_m is the electric potential and the current density can be found by,

$$\boldsymbol{I_m} = -\kappa\nabla\phi_m \tag{3.27}$$

κ, membrane's ionic conductivity, is water content dependent via a well known equation for Nafion-type membranes as given in Table 3.3.

3.1.2 Boundary Conditions

This study covers the analysis of geometry of the flow fields and the direction of the flow in interdigitated flow field design. In order to incorporate the particular cases into the model, boundary conditions associated with each case is imposed specifically. In this section, first the boundary conditions for conventional flow field design will be explained and then the differences of interdigitated design from conventional one will be discussed.

3.1.2.1 Boundary Conditions for Conventional Flow Fields Design

In the conventional design the channels connecting to the cell conveys the flow into the MEA. Thus, all the openings of MEA to the flow fields serve as inlets. Also, a little pressure drop and difference in reactant concentrations between consecutive openings are assumed. So, the inlets at either anode or cathode are equivalent. Thus, MEA has a symmetry axis passing from the midpoints of anode and cathode

Table 3.3 Membrane water content dependent terms

Parameter	Expression	Reference
D_w	$3.5\text{x}10^{-7}\exp(-2436/T)c_w$	West and Fuller (1996)
n_d	$0.0029c_w^2 + 0.05c_w$	Dutta et al. (2001)
κ	$\exp(1268(1/303-1/T))(0.5139c_w - 0.326)$	Springer (1991)

Maxwell-Stefan Equations

For the inlets of the electrodes Dirichlet type boundary conditions are used as mass fractions of H_2, H_2O and O_2. At the membrane interface Neumann type boundary conditions are imposed as mass fluxes and elsewhere they are set to insulation/symmetry.

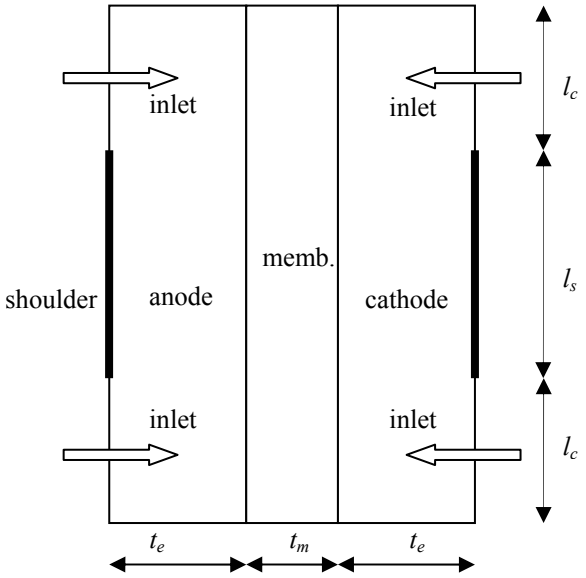

Figure 3.1: Computational domain and dimensions

Following Dirichlet boundary conditions are imposed at the inlets,

$$w_{H_2} = w_{H_2}^{in} \tag{3.28}$$

$$w_{O_2} = w_{O_2}^{in} \tag{3.29}$$

$$w_{H_2Oc} = w_{H_2Oc}^{in} \tag{3.30}$$

At the anode membrane interface hydrogen is depleted and the direction of water transport is assumed to be from anode to cathode so mass fluxes of H_2 and H_2O both serve as sink terms.

$$n_{H_2Oa} = -\alpha \frac{i_a}{F} M_{H_2O} \tag{3.31}$$

$$n_{H_2} = -\frac{i_a}{2F} M_{H_2} \tag{3.32}$$

The boundary condition of Maxwell-Stefan equation for H_2 is

$$-\boldsymbol{n_a}\bullet\left[-\rho.w_{H_2}\sum_{j=1}^{N}D_{H_2-j}\left\{\left(\nabla x_j+\left(x_j-w_j\right)\frac{\nabla p}{p}\right)\right\}+\rho.w_{H_2}.\boldsymbol{u}\right]=n_{H2} \tag{3.33}$$

where $\boldsymbol{n_a}$ is the normal vector shown in Figure (3.2). Minus sign in front of the normal vector is used for specifying inward fluxes to the subdomains. It should be noted that Maxwell-Stefan equation is solved only for H_2 at the anode and the mole fraction of H_2O is calculated with eq.(3.9). However, mass flux of H_2O at the membrane is taken into consideration in the boundary condition of Darcy's Law; thus, this flux is involved in the mass balance through the coupled momentum equation as it will be seen in eq. (3.42).

In the cathode membrane interface mass fluxes of O_2 and H_2O are,

$$n_{O_2}=-\frac{i_c}{4F}M_{O_2} \tag{3.34}$$

$$n_{H_2Oc}=(2\alpha+1)\frac{i_c}{2F} \tag{3.35}$$

$$-\boldsymbol{n_c}\bullet\left[-\rho.w_{O_2}\sum_{j=1}^{N}D_{O_2-j}\left\{\left(\nabla x_j+\left(x_j-w_j\right)\frac{\nabla p}{p}\right)\right\}+\rho.w_{O_2}.\boldsymbol{u}\right]=n_{O_2} \tag{3.36}$$

$$-\boldsymbol{n_c}\bullet\left[-\rho.w_{H_2Oc}\sum_{j=1}^{N}D^c_{H_2O-j}\left\{\left(\nabla x_j+\left(x_j-w_j\right)\frac{\nabla p}{p}\right)\right\}+\rho.w_{H_2Oc}\boldsymbol{u}\right]=n_{H_2Oc} \tag{3.37}$$

In equations (3.31 and 3.35) α is the net water transfer coefficient and it is defined as

$$\alpha=\frac{F.(\boldsymbol{n}\bullet\boldsymbol{J_w^T})}{i_{a,c}} \tag{3.38}$$

Along with eq.(3.18) α can be rewritten as

$$\alpha=-\frac{F}{i_{a,c}}m.D_w\frac{\partial c_w}{\partial y}+n_d \tag{3.39}$$

i_a or i_c terms appearing in the above equations are the boundary conditions for Ohm's Law either at the anode membrane or cathode membrane boundary which will be discussed later.

Apart from the electrode inlets and membrane interfaces, zero flux boundary condition is used to exploit the symmetry of the system,

$$-\boldsymbol{n}_{\xi} \bullet \left[-\rho . w_i \sum_{j=1}^{N} D_{O_2-j} \left\{ \left(\nabla x_j + \left(x_j - w_j \right) \frac{\nabla p}{p} \right) \right\} + \rho . w_i . \boldsymbol{u} \right] = 0 \tag{3.40}$$

Darcy's Law

For the inlets of the electrodes Dirichlet type boundary conditions are used to specify the pressures at the gas flow channels. At the membrane-electrode interfaces flux boundary conditions are imposed as velocities of the gas mixture. The boundary conditions elsewhere are set to zero flux.

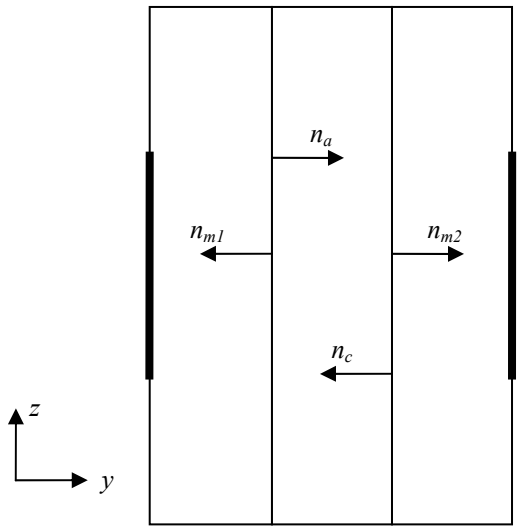

Figure 3.2: Normal vectors associated with each subdomain of MEA.

At the anode and cathode inlets boundary conditions are

$$p = p_{a,c}^{in} \tag{3.41}$$

At the anode membrane and cathode membrane interfaces the velocities are respectively defined as,

$$u_a = (n_{H_2} + n^a_{H_2O}) / \rho_a \tag{3.42}$$

$$u_c = (n_{O_2} + n^c_{H_2O}) / \rho_c \tag{3.43}$$

where ρ_a and ρ_c are anode and cathode mixture densities and calculated from eq. (3.10). Then the boundary conditions can be specified as,

$$-\boldsymbol{n_a} \bullet \boldsymbol{u} = u_a \tag{3.44}$$

$$-\boldsymbol{n_c} \bullet \boldsymbol{u} = u_c \tag{3.45}$$

And elsewhere zero flux conditions are imposed,

$$-\boldsymbol{n_a} \bullet \boldsymbol{u} = 0 \tag{3.46}$$

Water Transport

As described before, unlike the other models, flux boundary conditions are imposed at the electrode interfaces instead of Dirichlet boundary conditions.

Since there is a phase change of water between the electrodes and membrane, it may happen that at the liquid surface water vapor is lost to a surrounding stream resulting in jumps of concentrations across the electrode membrane boundary [7]. At anode and cathode sides two water uptake mechanisms of the form

$$\frac{j^a}{m} = -\gamma(c_w - c^a_w) \tag{3.47}$$

$$\frac{j^c}{m} = \gamma(c_w - c^c_w) \tag{3.48}$$

are used. Here the equilibrium sorption values, c^a_w and c^c_w at anode and cathode which depend on water activity at the boundaries are the concentrations in the bulk stream and c_w is the surface concentration. γ the proportionality constant is the mass transfer coefficient for water.

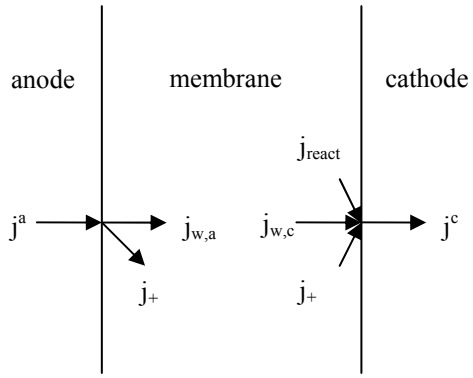

Figure 3.3: Inward and outward fluxes at the membrane.

As it is seen in Figure 3.3 water flux associated with electro-osmotic drag acts as a sink term at anode and a source term at cathode. Also with the inclusion of the flux term related to the water generated in the reaction, mass balances across the interfaces imply that fluxes at anode and cathode boundaries will be [3];

$$j^a = j_{w,a} + j_+ \tag{3.49}$$

$$j^c = j_{react} + j_{w,c} + j_+ \tag{3.50}$$

along with the equations (3.47), (3.48)

$$j_{w,a} = -m.\gamma.(c_w - c_w^a) - n_d \frac{i_a}{F} \tag{3.51}$$

$$j_{w,c} = m.\gamma.(c_w - c_w^c) - (n_d + 1/2)\frac{i_c}{F} \tag{3.52}$$

In these expressions, local equilibrium value of water content is used which is calculated as a function of local water activity $a = p_{H_2O} / p_{sat}$,

$$c_w^{a,c} = 0.043 + 17.81a - 39.85a^2 + 36a^3 \quad \text{, for } a \le 1$$

$$c_w^{a,c} = 14 + 1.4(a-1) \quad \text{, for } 1 < a \le 3 \tag{3.53}$$

Finally the boundary conditions at the anode membrane and at the cathode membrane interfaces can be written as,

$$-\boldsymbol{n_{m1}} \bullet (-D.\nabla c_w) = j_{w,a} \tag{3.54}$$

$$-\boldsymbol{n_{m2}} \bullet (-D.\nabla c_w) = j_{w,c} \tag{3.55}$$

Electrochemical Relations

Since the catalyst layers are very thin with respect to the other domains of membrane electrode assembly, they can be treated as reactive boundaries. At both anode membrane and cathode membrane interfaces Butler-Volmer equation is used to find the transfer current densities either at the anode side or at the cathode side [2].

$$i = i_0 \left(\exp(\frac{\beta_1 .F}{R.T}\eta) - \exp(-\frac{\beta_2 .F}{R.T}\eta) \right) \tag{3.56}$$

where i_0 is the exchange current density found for particular reactant concentrations, $\beta_{1,2}$ is the transfer coefficient for each direction of the reaction, η is the local overvoltage either at the anode or at the cathode. Scaling the exchange current density the from reference value found for reference concentrations [5].

$$i_{0,a} = i_{0,a}^{ref} . \left(\frac{c_{H_2}^{sol}}{c_{H_2}^{ref}} \right)^{\gamma_{H_2}} \left(\frac{c_{H_+}^{sol}}{c_{H_+}^{ref}} \right)^{\gamma_{H_+}^{a}} \tag{3.57}$$

$$i_{0,c} = i_{0,c}^{ref} . \left(\frac{c_{O_2}^{sol}}{c_{O_2}^{ref}} \right)^{\gamma_{O_2}} \left(\frac{c_{H_+}^{sol}}{c_{H_+}^{ref}} \right)^{\gamma_{H_+}^{c}} \tag{3.58}$$

if the concentration of the protons are assumed constant at the catalyst surfaces above equations can be simplified as [43],

$$i_{0,a} = k_a . (c_{H_2}^{sol})^{\gamma_{H2}} \tag{3.59}$$

$$i_{0,c} = k_c . (c_{O_2}^{sol})^{\gamma_{O2}} \tag{3.60}$$

The concentrations of the species that are dissolved in the catalyst layers differ from the values for the bulk flow. Thus, the solute species concentrations are corrected with a known thermodynamic relation,

$$c_{H_2}^{sol} = \frac{p_{H_2}}{H_{H_2}} \tag{3.61}$$

$$c_{O_2}^{sol} = \frac{p_{O_2}}{H_{O_2}} \tag{3.62}$$

where H is Henry's constant. For oxygen as a function of temperature it is found from the following expression [4] whereas for hydrogen as a constant it is given in Table 3.4

$$K_{O_2} = 1.3473e5 * \exp(-\frac{666}{T}) \tag{3.63}$$

In Butler-Volmer equation the parameters depend strictly on the geometry and the catalyst layers and they are found experimentally. As it is taken into account in (3.57), if the concentrations of the reactants decrease, the current density also decreases.

Activation overpotential arises from the losses associated with the kinetics of the reaction and is found as,

$$\eta = V_{oc} - \phi_m - \phi_s \tag{3.64}$$

where ϕ_s is the potential of the electrode ϕ_m takes care of the ohmic losses in the membrane and V_{oc} is the open circuit voltage of the electrode which is zero at the anode whereas is a function of temperature at the cathode as [35].

$$V_{oc} = 0.0025T + 0.2329 \tag{3.65}$$

Open circuit voltage represents the theoretical voltage of the cell without any irreversibilities like activation losses, ohmic losses and concentration overpotential. It is found from the Gibbs free energy which represents the maximum available work that the system does.

Along with these discussions boundary conditions at the electrode membrane interface can be imposed as; for Ohm's Law at the electrodes,

$$-\boldsymbol{n}_a \bullet \boldsymbol{I}_s = -i_a \tag{3.66}$$

$$-\boldsymbol{n}_c \bullet \boldsymbol{I}_s = i_c \tag{3.67}$$

Table 3.4 Parameters used in the model for both designs

Parameter	Symbol	Value	Unit	Reference
universal gas constant	R	8.3143	J/(mol.K)	
Faraday's constant	F	96487	Coulomb/m	
conductive portion of electrode	ε_s	0.3		[4]
water fraction in membrane	ε_m	0.26		[52]
dry density of membrane	ρ_{mem}	1980	kg/m^3	[15]
equivalent weight of membrane	M_{mem}	1.1	kg/mol	[15]
H_2 concentration parameter	γ_{H2}	0.25		[5]
Henry's constant for H_2	K_{H2}	4.5585e3	$Pa.m^3/mol$	[4]

Table 3.5 Parameters used in the model for conventional design

Parameter	Symbol	Value	Unit	Reference
hydraulic permeability	k_p	$1.76x10^{-11}$	m^2	[17]
viscosity of anode gas	μ_a	$1.638x10^{-5}$	kg/(m.s)	[42]
viscosity of cathode gas	μ_c	$1.307x10^{-5}$	kg/(m.s)	[42]
dry porosity of electrode	ε_g	0.6		[46]
conductivity of electrode	σ	570	S/m	[32]
water mass transfer coefficient	γ	$1.1x10^{-4}$	m/s	estimated
anode transfer coefficient	$\beta_{1,2}$	0.5		[5]
cathode transfer coefficient	$\beta_{1,2}$	1		[5]
O_2concentration parameter	γ_{O2}	1		[5]
anode current constant	k_a	533	$A/(m.mol)^{0.5}$	[20]
cathode current constant	k_c	0.15	A.m/mol	estimated

and the same for Ohm's Law at the membrane only with the sign changes in order to assure the continuity with the inward outward flux convention. The shoulder at the anode is assigned as ground and cell voltage is applied to the shoulder at the cathode. All the other boundaries at the electrodes and the membrane are assigned zero flux condition taking care of electric insulation and symmetry of the system.

$$\phi_s = 0 \tag{3.68}$$

$$\phi_s = V_{cell} \tag{3.69}$$

$$-\boldsymbol{n}_\xi \bullet \boldsymbol{I}_s = 0 \tag{3.70}$$

3.1.2.2 Boundary Conditions for Interdigitated Flow Fields Design

Unlike the conventional flow fields design in this case, flow enters the MEA in one opening from the inflow channel and goes out of the MEA from another opening to the outflow channel. Thus, the only difference of interdigitated design from conventional case is one opening at both anode and cathode is assigned as outlet.

In an interdigitated PEMFC, having a gas distributor as the one in Figure 3.4, if both anode and cathode flow channels have the same direction from inlet to outlet, the design is called coflow and if the channels have the opposite direction, it is called counterflow. Roughly saying, if flow in both electrodes is either downward or upward the design is called coflow.

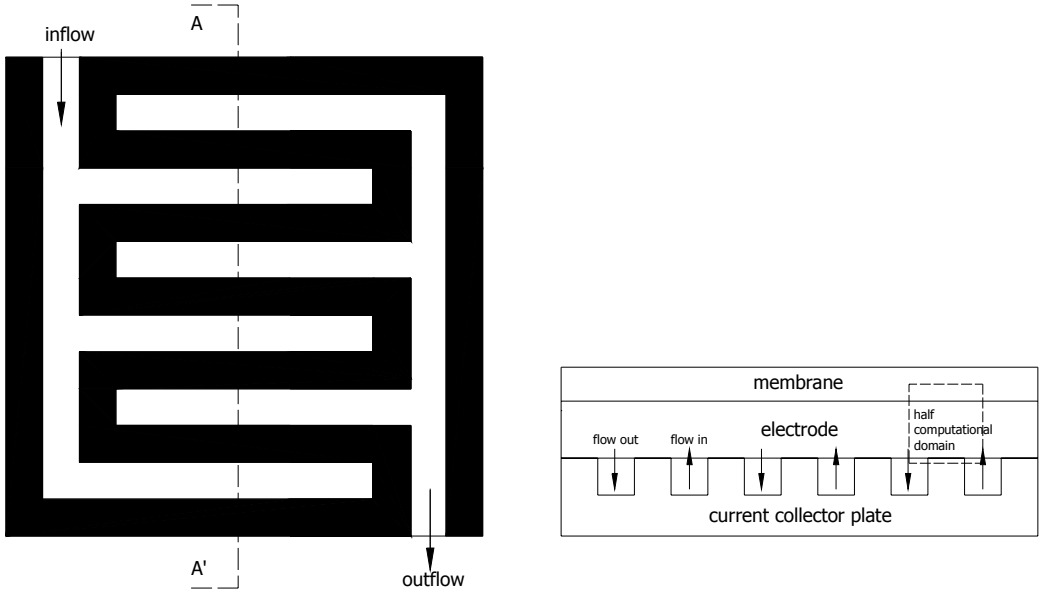

Figure 3.4: Top view of an interdigitated gas distributor (left) and A-A' cross section of half cell (right). The region enclosed with dashed lines is the half of the computational domain.

Coflow and counterflow cases distinguish in anode inlet and outlet boundary conditions (Figure 3.5). The only difference is what the anode inlet boundary condition for counterflow is the anode outlet boundary condition for coflow and vice versa.

For Darcy's Law, in both anode and cathode outlet, Dirichlet type boundary conditions are specified like the inlet boundary conditions that are used in conventional design.

$$p = p_{atm} \tag{3.71}$$

For Maxwell-Stefan equations, outlet boundary conditions are set as convective flux which means any mass transport through that boundary is convection dominated and there is no mass flux due to diffusion.

$$-\boldsymbol{n}\bullet\left[-\rho w_i\sum_{j=1}^{N}D_{O_2-j}\left\{\left(\nabla x_j+\left(x_j-w_j\right)\frac{\nabla p}{p}\right)\right\}\right]=0 \tag{3.72}$$

where normal vector, $\boldsymbol{n}$, is either for the anode outlet or the cathode outlet.

For Ohm's Law boundary conditions at the outlets are set as the same as those set for inlets in conventional design.

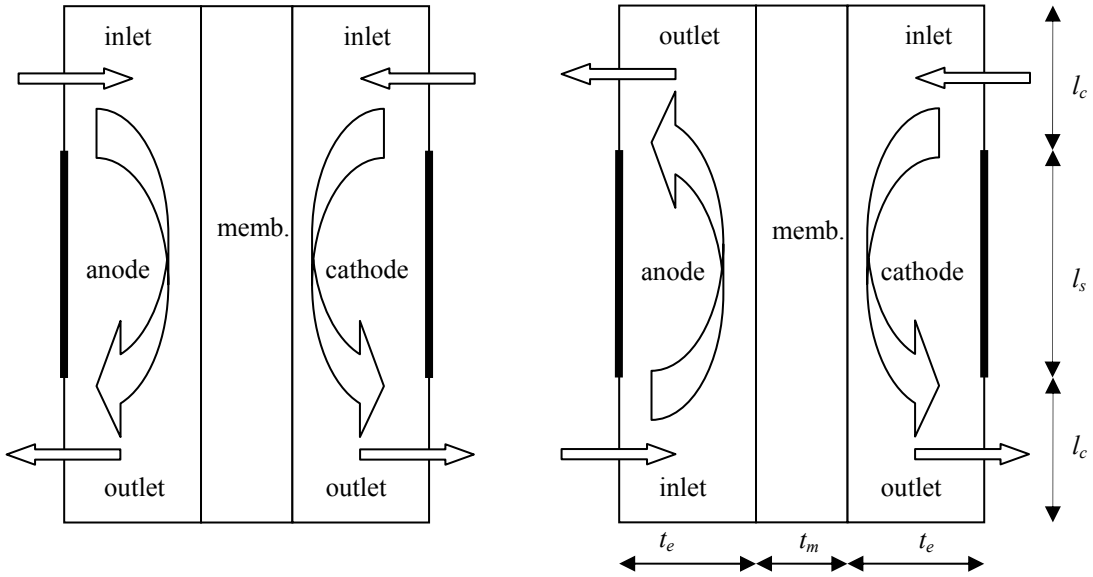

Figure 3.5: Computational domain and dimensions of the fuel cell for coflow (left) and counterflow (right).

3.2 Lumped Model Definition

The lumped model used in this study is mainly built on the model developed by Pukrushpan et al. (2004) [37]. The model consists of four subsystems: anode flow model, cathode flow model, cell voltage model and membrane hydration model. In anode and cathode flow models, simple mass balances are used to define the dynamics

Table 3.6 Parameters used in the interdigitated design

Parameter	Symbol	Value	Unit	Reference
hydraulic permeability	k_p	$1.2\text{x}10^{-12}$	m^2	[23]
viscosity of gas	μ	$2.03\text{x}10^{-5}$	kg/(m.s)	[23]
dry porosity of electrode	ε_g	0.3		[23]
conductivity of electrode	σ	727	S/m	[28]
water mass transfer coefficient	γ	$5\text{x}10^{-4}$	m/s	estimated
anode transfer coefficient	$\beta_{1,2}$	1		
cathode transfer coefficient	β_1	0.5		[23]
cathode transfer coefficient	β_2	0		[23]
anode current constant	k_a	$17\text{x}10^7$		[43]
exchange current density	k_c	43	A/m^2	estimated

of the reactants considering the humidity and pressure changes. In cell voltage model, the relation between reactant concentrations and cell voltage is modeled as well as ohmic losses in the membrane are calculated. Finally, in the membrane hydration subsystem, transient water transfer across the membrane is modeled.

3.2.1 Anode and Cathode Flow Models

Conservation of mass is applied for each substance at the anode and the cathode such that net mass flow rate across the electrode is equal to the rate of change in the mass. Calculated mass flow rate is, then, used to find the partial pressures of the substances, henceforth the relative humidity of the gases, assuming that all the gasses obey the ideal gas law and water exists only in the gas phase in the porous electrodes. At the electrodes, mass balances imply that,

$$\frac{dm_i}{dt} = W_i^{in} - W_i^{out} + W_i^{source} - W_i^{sink} \tag{3.73}$$

where i stands for H_2 and H_2O at the anode and O_2, H_2O and N_2 at the cathode. Inlet and outlet mass flow rates in this equation are determined from the mass fractions of each substance. Here, it is assumed that all hydrogen entering the anode is depleted during the reaction and water is accumulated in the anode thus, $W^{out}=0$ for anode. Inlet flow rate of anode is calculated as,

$$W_{an}^{in} = K_1.(p_{sm} - p_{an}) \tag{3.74}$$

where K_1 is hydrogen valve constant. The total mass flow rate entering and exiting the cathode are calculated as,

$$W_{ca}^{in} = k_{sm}^{out}.(p_{sm} - p_{ca}) \tag{3.75}$$

$$W_{ca}^{out} = k_{ca}^{out}.(p_{ca} - p_{rm}) \tag{3.76}$$

where k_{sm}^{out} and k_{ca}^{out} are supply manifold and cathode orifice constants respectively; p_{sm} and p_{rm} are the supply manifold and return manifold pressures, which are calculated from dynamics of the other system components, such as a compressor and heat exchangers which are not included in this model. Here, p_{sm} is given as the pressure of inlet of the gas flow channel, whereas p_{rm} is the pressure of the outlet gas flow channel. A 90% of the inlet pressure due to pressure drop is assumed to be reasonable.

Water generated at the cathode during reaction enters (3.73) as a source term. Oxygen and hydrogen depleted during the reaction serve as sink terms for each species. Sink and source terms accompanying with the reaction can be calculated by,

$$W_{O_2}^{reacted} = \frac{I}{4F} M_{O_2} A_{fc} n \tag{3.77}$$

$$W_{H_2}^{reacted} = \frac{I}{2F} M_{H_2} A_{fc} n \tag{3.78}$$

$$W_{H_2O_c}^{generated} = \frac{I}{2F} M_{H_2O} A_{fc} n \tag{3.79}$$

Here n is the number of cells in the stack, A_{fc} is the cell active area and I is the current density drawn from the system. Note that, lumped model is for the full stack; hence the flow rates are for the inlet and outlet of the complete stack rather than a single cell.

Finally, assuming the direction from anode to cathode as positive, water transferred through the membrane enters (3.73) as a sink term at the anode and a source term at the cathode.

3.2.2 Membrane Hydration Model

The same governing physics as in the CFD model is considered for the lumped model also. However, the implementation of the phenomena is different. Unlike in 2D model, membrane water content is found from equilibrium sorption values. Also, it is assumed that there is variation of water content only in the direction from anode to cathode. Thus, total flux inside the membrane ∇J_w^T is taken as dJ_w^T / dy. In the lumped model this expression may be approximated as

$$\nabla J_w^T = \frac{dJ_w^T}{dy} = \frac{\left(J_w^T\right)_a - \left(J_w^T\right)_c}{t_m} \tag{3.80}$$

Moreover with the same reasoning, membrane water content gradient ∇c_w in $\left(J_w^T\right)_a$ and $\left(J_w^T\right)_c$ is taken as dc_w / dy. A free node is introduced in the middle of the membrane and water concentration is assumed linear over each half of the membrane domain. Hence the derivative dc_w / dy is approximated at both anode and cathode side. (Figure 3.6)

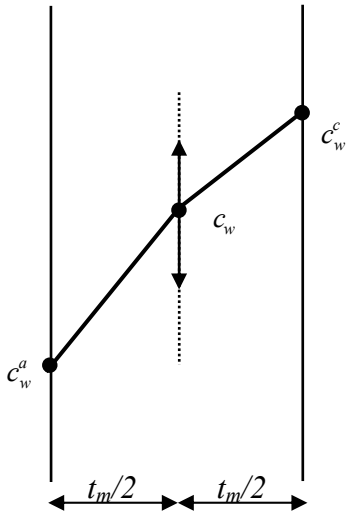

Figure 3.6: Assumed water concentration profile inside the membrane

$$\left(\nabla c_w\right)_a = \left(\frac{dc_w}{dy}\right)_a = \frac{2(c_w - c_w^a)}{t_m} \tag{3.81}$$

$$\left(\nabla c_w\right)_c = \left(\frac{dc_w}{dy}\right)_c = \frac{2(c_w^c - c_w)}{t_m} \tag{3.82}$$

With these equations, Eq. 3.18 can be lumped over the membrane as following,

$$\left(J_w^T\right)_a = -m.\left(D_w\right)_a \frac{2(c_w - c_w^a)}{t_m} + \left(n_d\right)_a \frac{I}{F} \tag{3.83}$$

$$\left(J_w^T\right)_c = -m.\left(D_w\right)_c \frac{2(c_w^c - c_w)}{t_m} + \left(n_d\right)_c \frac{I}{F} \tag{3.84}$$

$$\frac{d}{dt}\left(m.c_w\right) = \frac{1}{\varepsilon_m t_m}\left[\left(-m.D_w \frac{2(c_w^c - c_w)}{t_m} + n_d \frac{I}{F}\right)_c - \left(-m.D_w \frac{2(c_w - c_w^a)}{t_m} + n_d \frac{I}{F}\right)_a\right] \tag{3.85}$$

In these equations subscripts *a* and *c* of the parentheses refer to anode and cathode respectively. D_w and n_d are calculated separately at anode and cathode by the expression in Table 3.3. In (3.73), sink and source terms accompanying with the water transfer through the membrane is calculated as,

$$\left(W_{H_2O}^{memb}\right)_{a,c} = \left(J_w^T\right)_{a,c} M_{H_2O} A_{fc} n \tag{3.86}$$

3.2.3 Cell Voltage Model

Voltage of the cell is calculated from eq.(3.64),

$$V_{cell} = V_{oc} - \eta_c - I.R \tag{3.87}$$

where ϕ_m is replaced by $I.R$ where R is the resistance of the membrane which is found as

$$R = \frac{t_m}{\kappa} \tag{3.88}$$

Since current density is the set parameter in this model, η_c as a function of drawn current density is found by reformulating the Butler-Volmer equation (3.56) at the cathode,

$$\eta_c = \frac{R.T}{\beta_c.F} asinh\left(\frac{I}{k_c.(c_{O_2})^{\gamma_{H2}}}\right) \tag{3.88}$$

Table 3.7 Parameters used in the lumped model

Parameter	Symbol	Value	Unit	Reference
supply manifold orifice	$k_{sm,out}$	0.363×10^{-5}	kg/(s.Pa)	[37]
cathode orifice constant	$k_{ca,out}$	0.218×10^{-5}	kg/(s.Pa)	[37]
proportional gain	K_1	0.21×10^{-4}	kg/(s.Pa)	[37]

Table 3.8: Geometrical and operational parameters used as the base case for conventional design [46]

Property	Value
Gas channel width l_c	0.10 cm
Shoulder width l_s	0.10 cm
Electrode height t_e	0.026 cm
Membrane thickness t_m	0.023 cm
Inlet mol fraction of oxygen	0.1904
Inlet mol fraction of water at cathode	0.0934
Inlet mol fraction of hydrogen	0.844
Anode side pressure	3 atm
Cathode side pressure	5 atm
Operation temperature	80^0C

Table 3.9: Geometrical and operational parameters used as the base case for interdigitated design [22]

Property	Value
Inlet channel width l_c	0.05 cm
Shoulder width l_s	0.10 cm
Outlet channel width l_c	0.05 cm
Electrode height t_e	0.025 cm
Membrane thickness t_m	0.0125 cm
Inlet mol fraction of Oxygen $x_{O2,in}$	0.21
Inlet mol fraction of Nitrogen $x_{N2,in}$	0.79
Inlet mol fraction of Hydrogen $x_{H2,in}$	0.83
Anode and cathode inlet pressure $p_{a,in}$	1.0133 atm
Anode and cathode outlet pressure	1 atm

CHAPTER 4

NUMERICAL IMPLEMENTATION

4.1 Lumped Model

The lumped model is implemented into MATLAB-Simulink and the ordinary differential equations are solved with the fixed-step ode1 MATLAB function. Fixed-step continuous solvers of Simulink compute a model's continuous states at equally spaced time steps from the simulation start time to the simulation stop time. The solvers use numerical integration to compute the continuous states of a system from the state derivatives specified by the model. Each solver uses a different integration method: ode1 uses Euler's approximation and it is very efficient for initial value problems due to the low computational effort, but it trades accuracy.

ode1's Euler's method uses the derivative at a point to calculate the value of the corresponding function at the succeeding point with the expression,

$$y_{n+1} = y_n + \frac{df(t)}{dt}(t_{n+1} - t_n) \tag{4.1}$$

Choosing the step time t_{n+1}- t_n small enough, the approximation will be more accurate.

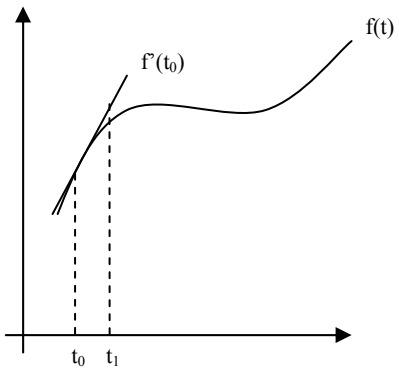

Figure 4.1: Euler's method

For the step time equal to 1 ms, the lumped model simulations took less than 30 seconds. To verify the results, model is tested for different solver types: ode1's results are found to be consistent with the results of other integration methods including stiff solvers ode15s and ode23s and higher order methods, ode45 and ode23. Within the scope of our simulations, neither stiffness nor the stability poses an issue.

4.2 CFD Model

The complete mathematical model was implemented into a commercial computational fluid dynamics package, FEMLAB® which is equipped with predefined partial differential equations (PDEs). It allows the user to change the coefficient of predefined PDEs or generate new ones from the general equation forms. FEMLAB® uses finite element method (FEM) to approximate the solutions for the conservation form of the equations for mass, momentum, energy and multi species transport. FEM is not the only way for solving the continuum fluid dynamics problems. Methods like boundary element, finite difference and finite volume are widely used in CFD models. The primary advantage of using FEMLAB®'s FEM implementation is it's flexibility to employ a Galerkin weak formulation to improve the accuracy akin to flux boundary conditions used in our model.

4.2.1 Background on Finite Element Method

The Finite Element Method (FEM) is a numerical technique for solving field equations by *discretization* of an object into very small pieces called *finite elements* so as to calculate their individual behavior reasonably accurately based on fairly simple analysis. As illustrated in Figure 4.2 for a wrench, a complicated structure is modeled as an assembly of large number of simple pieces or elements. The subdivision of the object into the elements is called *mesh*. The physics of one element is approximately described by so called *degrees of freedom* (*DOFs*), a finite number of dependent variables of the unknown functions on the *nodes* of the mesh. Each element is assigned a set of characteristic equations describing physical properties, boundary conditions, and imposed forces, which are then solved as a set of simultaneous equations to predict the object's behavior.

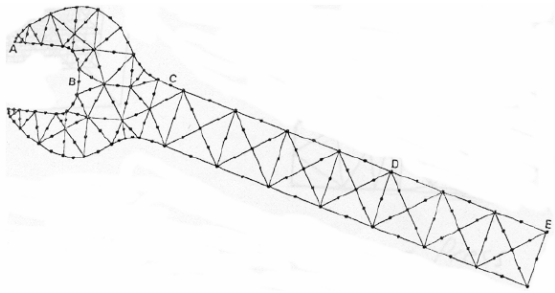

Figure 4.2: FE model of a wrench for displacement and stress analysis (Schwards, 1980)

4.2.2 Mesh

To solve our model, we used quadratic Lagrange triangular elements. A Lagrange element with the order of *k*, the nodes of the element have the coordinates that are integer multiples of k. For a quadratic triangular Lagrange element this means that there are nodes at the corners and side midpoints of each triangle element as it is seen in Figure 4.3.

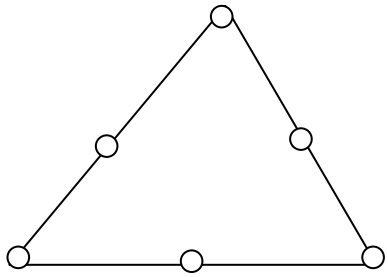

Figure 4.3: A quadratic Lagrange triangular element

The mesh structures that are used for the conventional and the interdigitated designs can be seen in Figures 4.4. A finer mesh is used for the membrane subdomain and mesh is refined at the corners of the electrode inlets and outlets. Mesh for conventional design consists of 4404 elements whereas the one for interdigitated design consists of 3392 elements. With 7 DOF at each node, there are 3654 nodes for the conventional design and 3048 nodes for the interdigitated design.

4.2.3 Solution

FEMLAB®'s stationary nonlinear solver, time dependent solver and parametric solvers were used for the steady state analysis, dynamic analysis and parametric studies respectively. Many of the parameters used in the model depend on the solution sought and there are stringent couplings between the governing partial differential equations which make the model highly nonlinear.

FEMLAB®'s nonlinear solver has two alternatives: one breaks down the nonlinear problem into the solution of one or several linear systems of equations. In other words, the software approximates the nonlinear model with a linear model, and the approximation is valid when the solution is near the linearization point, which is updated in each iterative step, hence, usually, guaranteeing a convergence. Then the linear solver solves the corresponding linearized model at each iteration.

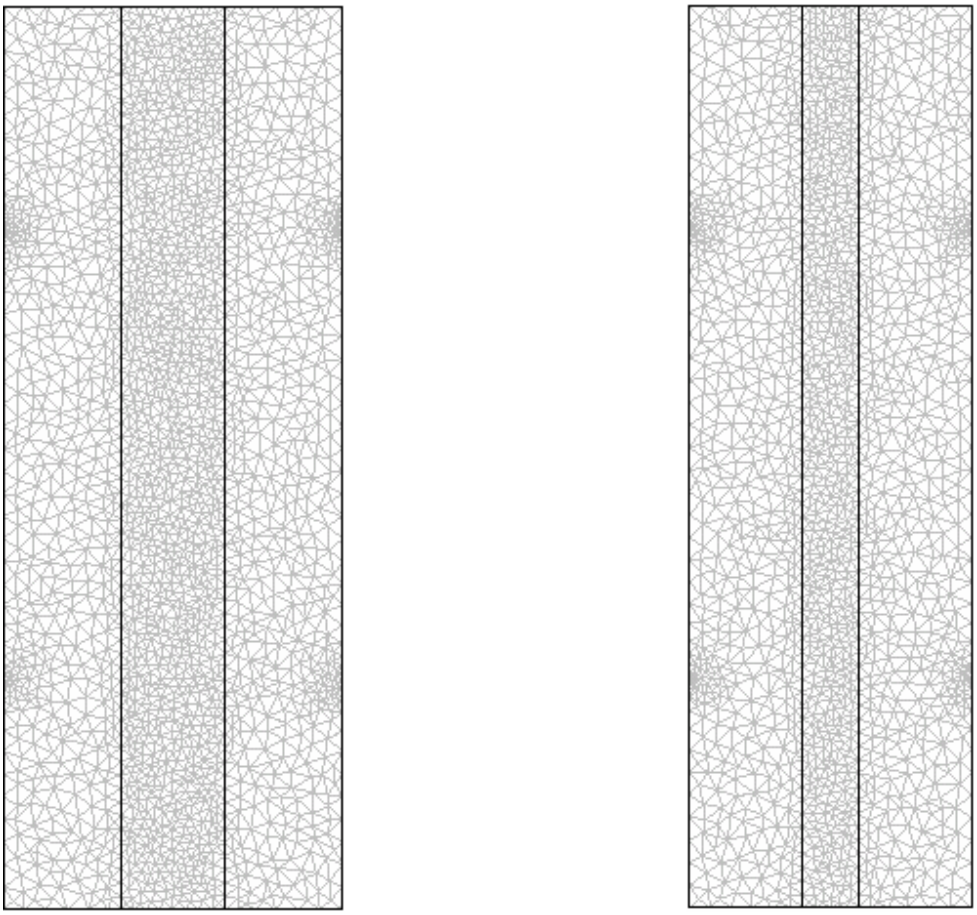

Figure 4.4: Mesh structures for the conventional (left) and the interdigitated (right) designs

The other alternative for the nonlinear solver uses an affine invariant form of the damped Newton Raphson method as described in [13]. After the finite element discretization model equations can be written like

$$\boldsymbol{f(U)}=0 \tag{4.2}$$

where $\boldsymbol{f(U)}$ is the residual vector and $\boldsymbol{U}$ is the solution vector. FEMLAB® generates the linearized equation system around the initial guess $\boldsymbol{U_0}$ which is the solution vector at the linearization point. The software solves the linearized model

$$\boldsymbol{f'(U_0)}\delta U = -\boldsymbol{f(U_0)} \tag{4.3}$$

for the δU Newton step with a linear system solver. Here $\boldsymbol{f'(U_0)}$ is the Jacobian matrix. Iteratively, U_1 is computed by

$$\boldsymbol{U_1}=\boldsymbol{U_0}+\lambda.\delta U \tag{4.4}$$

where $\lambda \in (0,1]$ is the damping factor. If the relative error calculated at this step is larger than the error calculated in previous iteration, solver reduces the damping factor and calculates $\boldsymbol{U_1}$ again and it continues this procedure until the error becomes less than the previous one. When it finds a successful step it goes on with the new iteration.

Equation 4.3 is solved with UMFPACK linear solver. UMFPACK solves general systems of the form

$$\boldsymbol{A.x = b} \tag{4.5}$$

by Gaussian elimination. It employs the COLAMD and AMD approximate minimum degree preordering algorithms to permute the columns. The code uses level-3 BLAS (Basic Linear Algebra Subprograms) for optimal performance. The solver differs from the naive Gaussian elimination by implementing a multi-frontal strategy for sparse systems as outlined in [12].

Time dependent solver of FEMLAB® discretizes the time dependent PDE problem to form either an ordinary differential equation system (ODE) or a differential-algebraic

equation (DAE) system. The solver uses variable-order variable-stepsize backward differentiation formulas (BDF) to solve. Thus the solver is an implicit time-stepping scheme, which implies that it must solve a possibly nonlinear system of equations at each time step. It solves the nonlinear system using a Newton iteration, and it then solves the resulting systems with a linear system solver [16].

Parametric solver is used to study the model behavior for different values of a specific parameter such as determining current density as a function of cell voltage or cathode pressure. The parametric solver consists of a loop around the usual stationary solver and where it estimates the initial guess based on the solution for the previous parameter value. If the nonlinear solver does not converge it tries a smaller parameter step; if it does converge it determines the size of the next parameter step based on the speed of the convergence of the Newton iteration [16].

4.2.4 Formulation of the Equation System

Before the solution, FEMLAB® converts a PDE and its boundary conditions into some formulations. There are general, coefficient, and weak formulations of PDE in FEMLAB®. Weak form was used in our simulations. The weak form is very effective for the convergence of the solution because it generates the exact Jacobian and the assembly is somewhat faster than in the coefficient and general forms. The Jacobian here is the one used in the Newton's algorithm, which is $f'(U_0)$ in equation 4.3. General and coefficient forms can generate incorrect Jacobian matrices if the model involves coupling variables or there are derivatives in the boundary conditions or some of the coefficients depend on the solution. As a consequence of the incorrect Jacobian the nonlinear solver or the time-dependent solver result in a slower convergence to the correct solution, and in some cases the solver even fails to find a solution.

A PDE is transformed into the weak form as following: A PDE for a single dependent variable u is considered in two space dimensions.

$$\nabla \bullet \boldsymbol{\Gamma} = F \qquad \text{in a subdomain } \Omega \tag{4.6}$$

Let v be an arbitrary function on Ω. Multiplying the PDE with v and integrating both sides leads to

$$\int_{\Omega} v\nabla \bullet \boldsymbol{\Gamma} dA = \int_{\Omega} vF dA \tag{4.7}$$

Using Green's Formula to integrate by parts

$$\int_{\partial\Omega} v\boldsymbol{\Gamma} \bullet \boldsymbol{n} ds + \int_{\Omega} \nabla v \bullet \boldsymbol{\Gamma} dA = \int_{\Omega} vF dA \tag{4.8}$$

where $\partial\Omega$ is represents the boundary and n is the normal vector. Using the Neumann boundary condition,

$$-\boldsymbol{n} \bullet \boldsymbol{\Gamma} = G + \frac{\partial R}{\partial u}\mu \tag{4.9}$$

the following equation is obtained

$$0 = \int_{\Omega} \left(\nabla v \bullet \boldsymbol{\Gamma} + vF\right) dA + \int_{\partial\Omega} v\left(G + \frac{\partial R}{\partial u}\right)\mu ds \tag{4.10}$$

which is the weak formulation of the original problem 4.4. Instead of Neumann boundary condition, Dirichlet boundary condition may also be used in the formulation. Here *v* is called the test function and it must be chosen from an appropriate function class. The weak formulation is a weaker condition on the solution as opposed to the strong form posed by equation 4.6. [16]

4.2.5 Convergence

Nonlinear models may converge to more than one solution or there may not be a solution. The converged solution also depends on the refinement of the mesh. The finer the mesh is the more accurate is the solution. In our model the reliability of the converged solution was tested by checking the variables on the boundaries where the exact solution is given to the equation system by the user. The contour plots of scalars such as concentration, temperature and pressure, as well as components of vectors such as velocity, hint at the reliability of the converged solution, as discontinuous contours

clearly suggest a poor solution, yet the smooth ones do not ensure convergence. Weak formulation of the FEM can only ensure that the solution is a "best" one within the specified space of test functions. Finally, a good way to ensure convergence is directly confirming the physics, such as conservation of mass, momentum, species and charge. For all the simulations presented here, mesh convergence, smoothness and physical verification of the results are ensured.

In a relative tolerance of 10^{-4} the for the time dependent problems, solution converged in about 400-1500 seconds depending on the problem on a Pentium 4 2.6 GHz CPU machine equipped with 1.5 GB RAM with 23744 and 25578 DOF for the interdigitated and conventional designs respectively.

For the convergence of the steady state problems, first Conductive Media application mode is solved for membrane. Then application modes, "Conductive Media" for the membrane and the electrodes, "Darcy's Law", "Maxwell-Stefan Equation" for the anode and "Diffusion" for the membrane are solved simultaneously. Then with the replacement of the application mode "Maxwell-Stefan Equation" for the anode with the "Maxwell-Stefan Equation" for the cathode the model is solved again. Finally all the application modes are involved in the model and the solution converged.

4.2.6 Postprocessing

Average values of variables and parameters are found by using *integration coupling variables* of the software. To find the average of any variable or parameter on a boundary,

$$\zeta_{av} = \frac{1}{L}\int_{\partial\Omega} \zeta .dl \tag{4.11}$$

is used. In this expression L is the length of the boundary. To find the average value in a subdomain,

$$\zeta_{av} = \frac{1}{A}\int_{\Omega} \zeta .dA \tag{4.12}$$

is used where A is the area of the subdomain.

CHAPTER 5

RESULTS

Simulations are carried out with lumped and CFD models for PEM fuel cell with conventional flow fields. CFD model is also utilized for the interdigitated design for both counterflow and coflow. In this chapter results of lumped and CFD models are compared for conventional design. Moreover, steady state and transient results are obtained from CFD model for different designs. Distributions of current density, reactant concentrations, water content …etc are plotted. Responses to the inputs in cell voltage, relative humidity of air, pressure of air are discussed.

5.1 Analysis of a PEMFC with Conventional Flow Fields

For the base case, operating conditions are taken from the experiments of Ticianelli et al. (1988) [46]. These parameters are listed in Table 3.8. The polarization curves associated with the lumped model and CFD model results are compared to the experimental data of Ticianelli et al. Figure 5.1 shows that lumped model results are close to the results of Ticianelli's. However there are some discrepancies between the polarization curves. On the other hand 2D model results agree with the experimental data very well. Since lumped model does not consider the spatial variations of the model variables, it is sure that the results differ from the actual ones. For instance, letting the mole fraction of oxygen at the cathode inlet 0.21, it is most probably less than 0.21 at the catalyst layer due to the spatial variations inside the cathode. However, the value at the cathode inlet enters the lumped model equations resulting in overestimate of the results of the lumped model.

For the lower current densities polarization curve of the model is above the actual values as expected whereas for current densities higher than 0.7 A/cm^2 the model results are below the actual values. As a result the slope of the polarization curve of the lumped

model is different than the actual polarization curve. The differences in the slopes can be attributed to the membrane water content. As a matter of fact, Figure 5.2 shows that in the lumped model membrane water content decreases more rapidly with the increasing current density than that of 2D model resulting in a greater slope in the polarization curve.

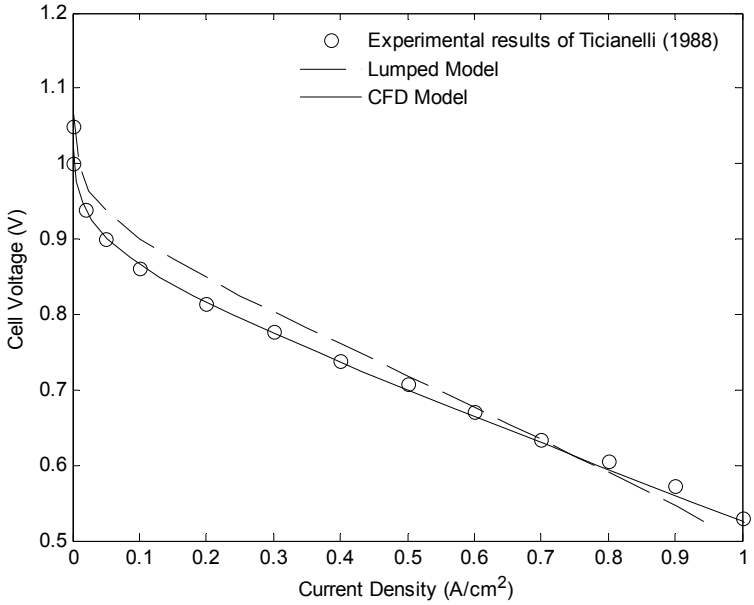

Figure 5.1: Polarization curve for lumped (dashed line) and CFD (solid line) models

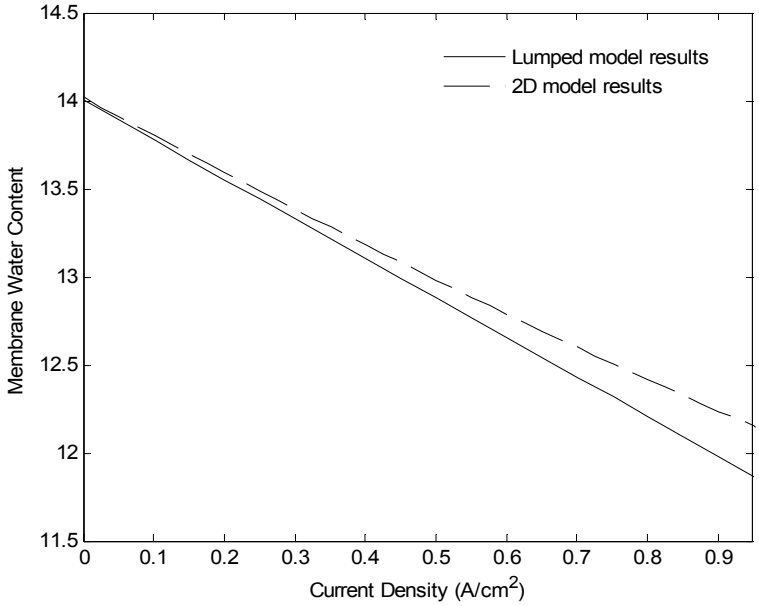

Figure 5.2: Membrane water content at different operating conditions

5.1.1 Dynamic Analysis with Lumped Model

Full dynamics of the water transport is included in the lumped model. Figure 5.3 shows the voltage response to a step input such that the current density increases from 0.35 A/cm^2 to 0.6 A/cm^2 for base case. It should be noted that the curves are shifted intentionally to set apart the responses. The effect of water transport on the dynamics of the system can be seen by comparing the settling times of two responses. When the dynamics of the water transport is included in the model, the system settles down after about 8 seconds, whereas it takes less than 1 second for the system to settle down in the case when the dynamics of the water transport is not included. Thus, it can be said that the dynamics of the fuel cell is mainly governed by the water transport. The time scale of the response is in the same order with the theoretical estimate

$$\tau \sim \varepsilon_m \frac{t_m^2}{D_w}$$

By using the expression for D_w given in Table 3.3 time scale is found to be 5 and 10 s for the membrane water contents 14 and 7 respectively. Preceding the transient associated with water transport, sudden jumps are observed for both models. These are due to the instantaneous chemical reactions.

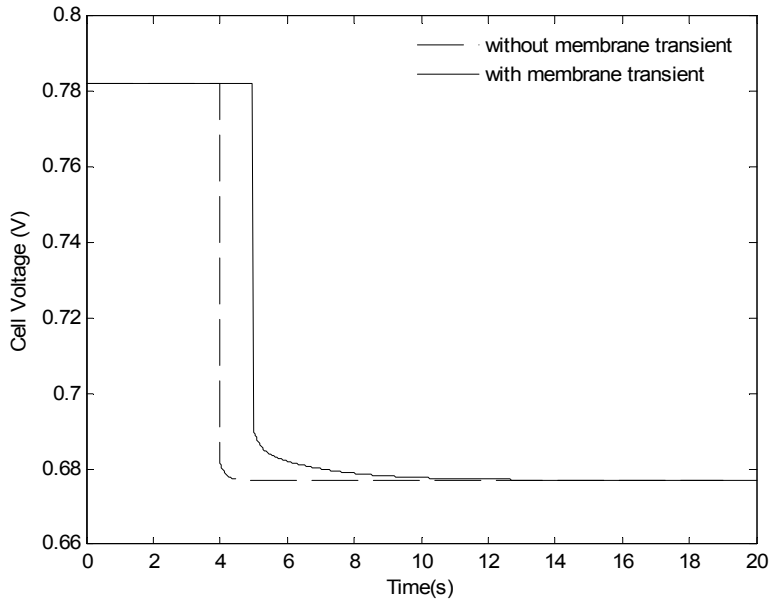

Figure 5.3: Dynamic response of cell voltage to the step input in current density such that it increases from 0.35 to 0.6 A/cm^2.at t=5 s. Results are taken with the inclusion of membrane water transient (solid line) and without the inclusion of membrane water transient (dashed) in the model

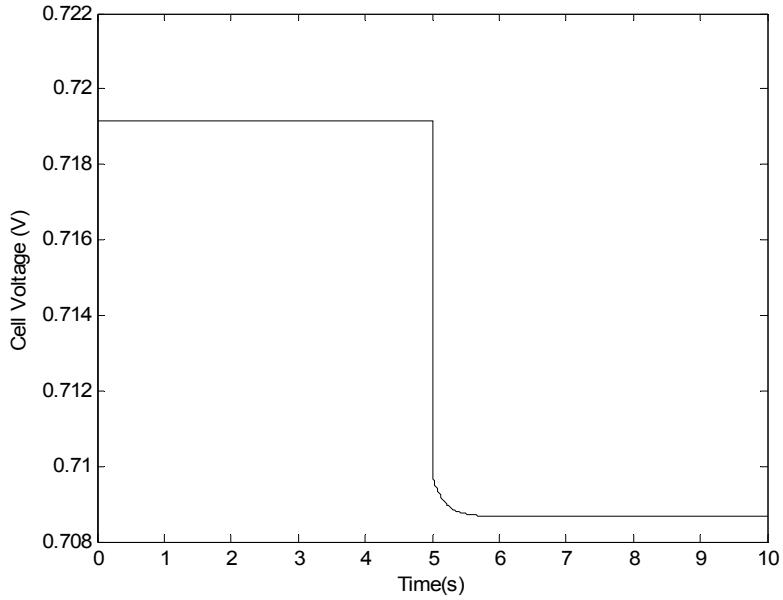

Figure 5.4: Dynamic response of cell voltage to a step input in air pressure such that it decreases from 5 atm to 4 atm at t=5 s.

Figure 5.4 shows the response of the cell voltage to a step input in pressure such that the pressure of the air is decreased from 5 atm to 4 atm at 0.5 A/cm^2 steady operating point. The transient of the system is shorter than that of the previous case. This is because inlet gases are assumed to be always fully humidified. In other words, the relative humidity of the gases at the cathode does not change. Relative humidity is the main parameter that determines the transient of the membrane water transport. Thus, longer transients are not observed in the response. The effect of the pressure input is reflected to the output with the change in oxygen concentration. The dynamics of the system in this case is governed by the mass transport inside the electrodes. The same response for CFD model will be discussed later (Figure 5.21).

Figure 5.5 shows the dynamic response of the system for the ramp input in current density such that at t=5 s it starts increasing from 0.35 A/cm^2 till t=10 s when it reaches 0.5 A/cm^2. In the previous step responses the effect of instantaneous chemical reaction has been observed as sudden jumps. For the ramp response, fast transient is observed such that cell voltage starts decreasing linearly as soon as the input is given. After this linear decrease, cell voltage changes gradually until the system settles down. This transient is shorter than those observed in step responses.

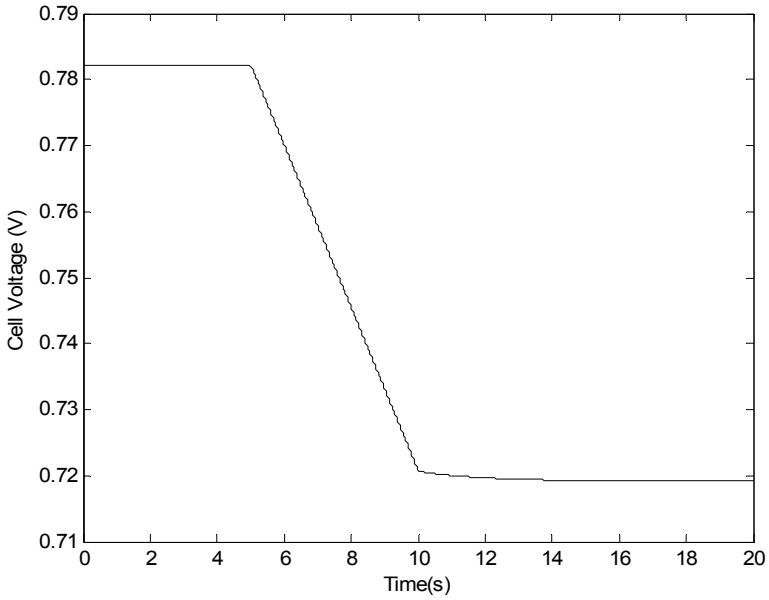

Figure 5.5: Dynamic response of cell voltage to a ramp input in current density such that it changes from 0.35 to 0.5 A/cm^2 in 5 s.

Control Application with Lumped Model

As a control problem, it is desired to maintain the output voltage constant when current is drawn from the system so that always more power is provided from the system when current is increased. To achieve this goal a control system is designed such that the current density perturbations in the system are compensated by adjusting the inlet pressure of the air. Block diagram of the fuel cell control system is depicted in Figure 5.6.

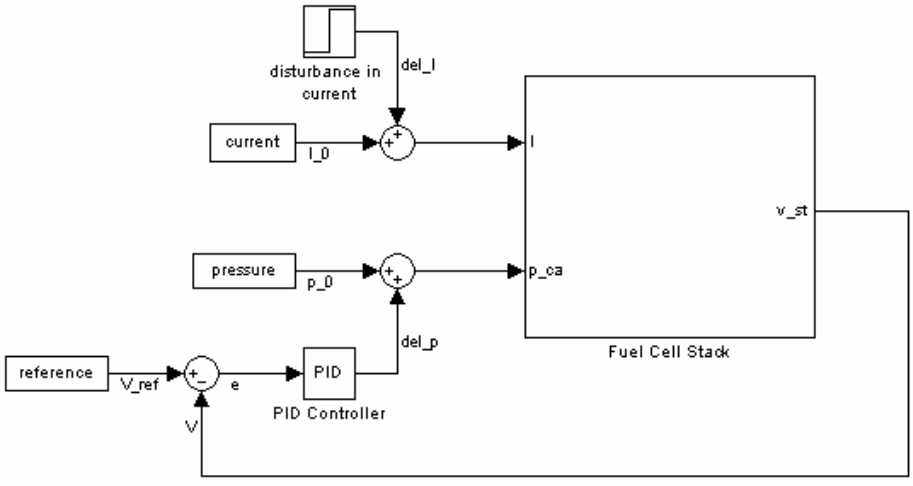

Figure 5.6: Block diagram of the closed loop system

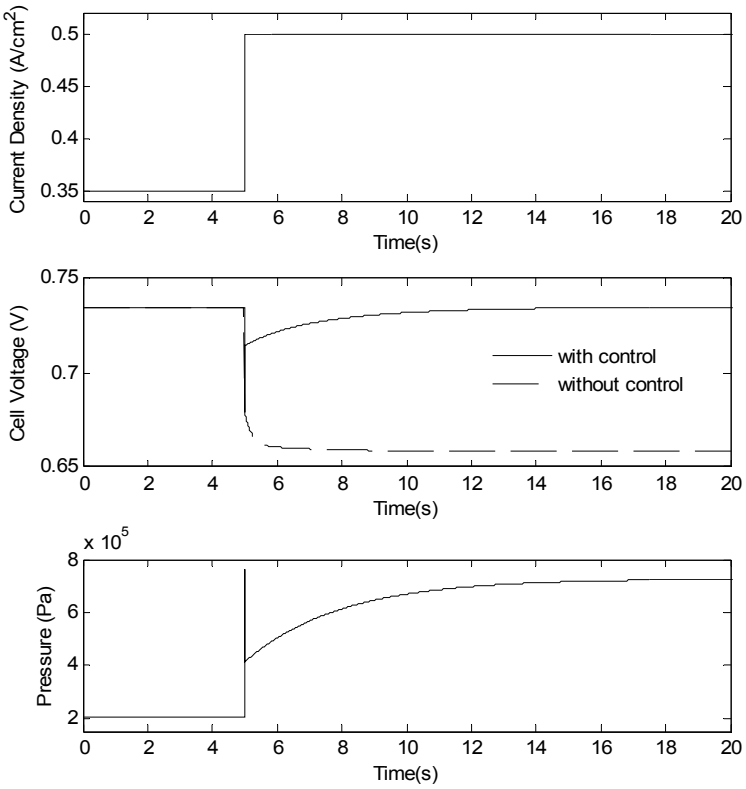

Figure 5.7: Dynamic response of the system to the step disturbance in current density

A step disturbance is given to the system such that the current density is increased from 0.35 A/cm^2 to 0.5 A/cm^2 for initial conditions as 1.5 atm anode and 2 atm cathode pressures. If there is no control, cell voltage decreases gradually and it reaches 0.66 V in a few seconds. When PI controller is introduced, cell voltage increases gradually after the sudden drop due to the chemical reaction and it reaches the reference value after about 10 seconds. Adjustments to the air pressure to realize the control objective is seen in Figure 5.7 c.

Proportional gain which makes the system faster is chosen as 10^7. Integral gain, responsible for compensating the steady state error, is also chosen as 10^7. Tuning the proportional gain will make the response of the controlled system faster. However, choosing greater controller gains require more compressor power which is taken from the fuel cell output reducing the net power. The control system is to be designed in the presence of this tradeoff.

In [37] similar control problems are outlined. It is asserted that for oxygen excess ratio equal to 2, maximum power is taken from the system at different operating points. Thus, a control scheme adjusting the air pressure to maintain the desired excess ratio is implemented.

5.1.2 Steady-State Analysis with CFD Model

Figure 5.8 shows the electric potential distribution at the electrodes at 0.5 V operating point. Anode current collector is assigned as ground and voltage is applied to the cathode current collector. Current flows from anode side to cathode side (Fig. 5.8), therefore voltage drop is continuous along this direction. These voltage drops are considered as conductive media losses in the overall cell voltage output.

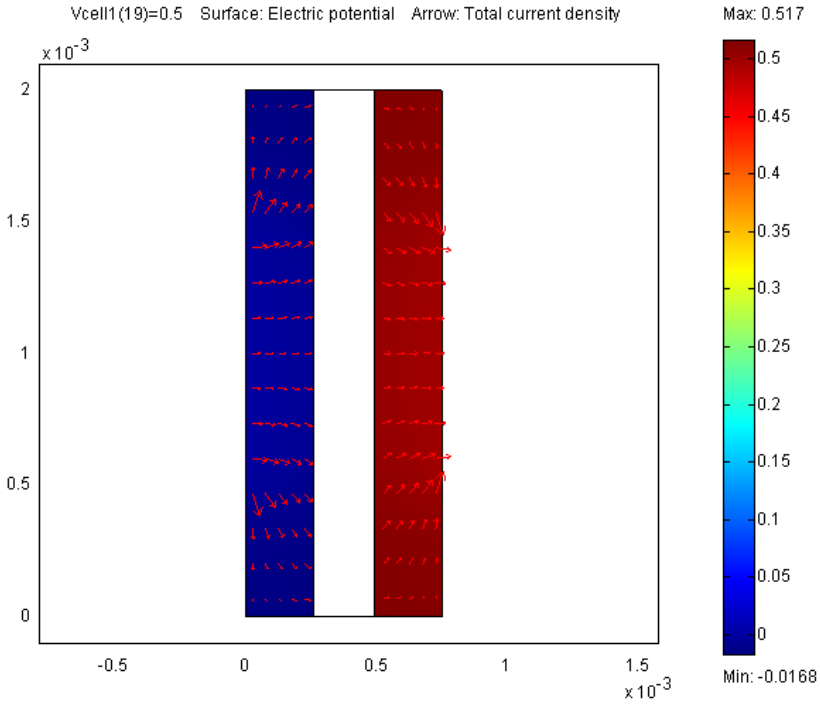

Figure 5.8: Distribution of the electric potential and the vector field of current density

Figure 5.9 shows the current density profile on the membrane cathode interface. Exchange current density which can also be interpreted as the reaction rate, is higher near the middle of the cathode. However, in the middle of the cathode, current density decreases. This can be explained by the parameters that take part in Butler-Volmer equation which states that exchange current density is a function of reactant concentration and the overpotential. Overpotential increases near the middle of the cathode because as it is seen in Figure 5.10 more current is passing at these points making the voltage drop get bigger. On the other hand since there is more water in the middle of the cathode, oxygen concentration gets smaller at these points. Considering the roles of these two parameters in Butler-Volmer equation, this current density profile on the membrane interface is acceptable.

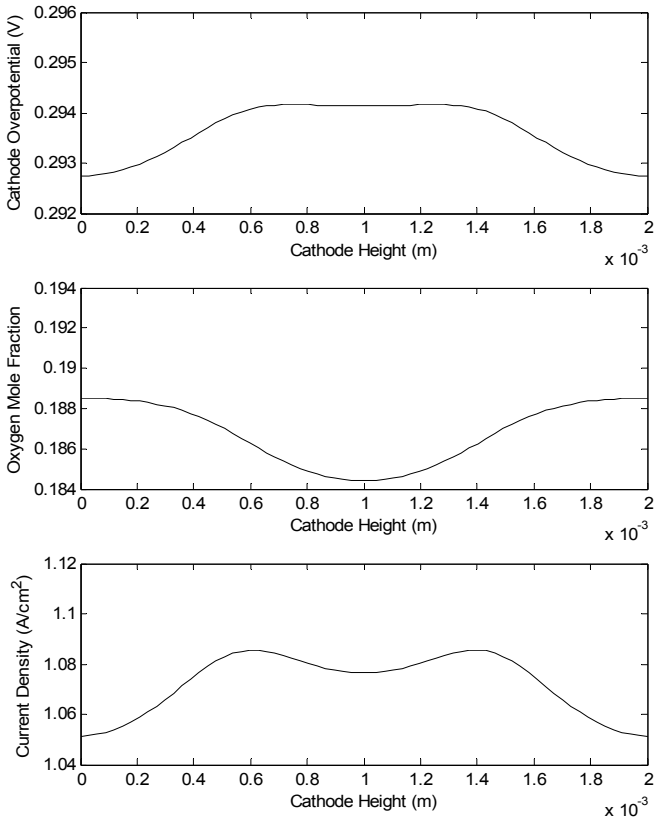

Figure 5.9: Exchange current density profile on the cathode membrane interface

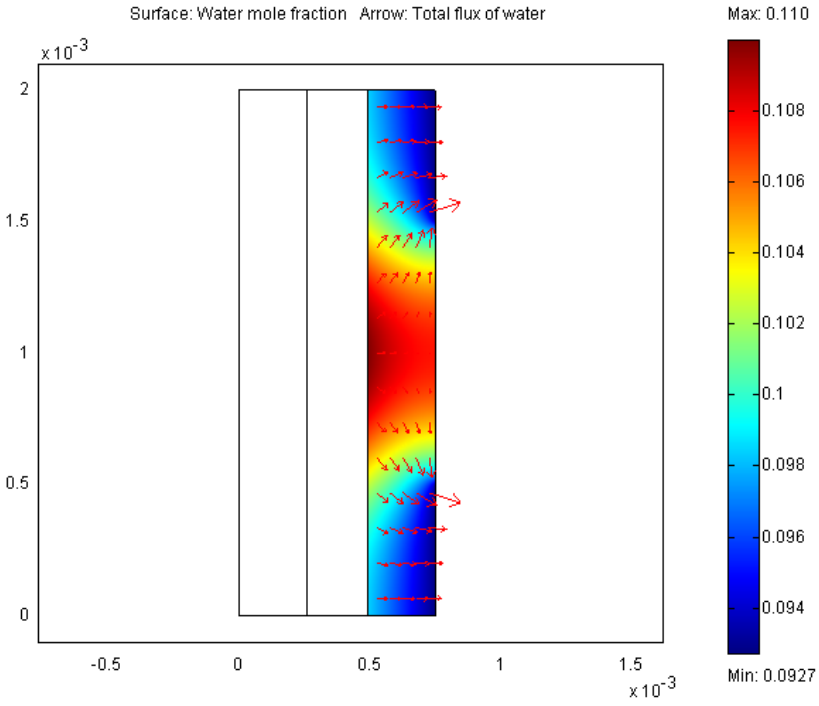

Figure 5.10: Distribution of water mole fraction and the vector field of total water flux at the cathode

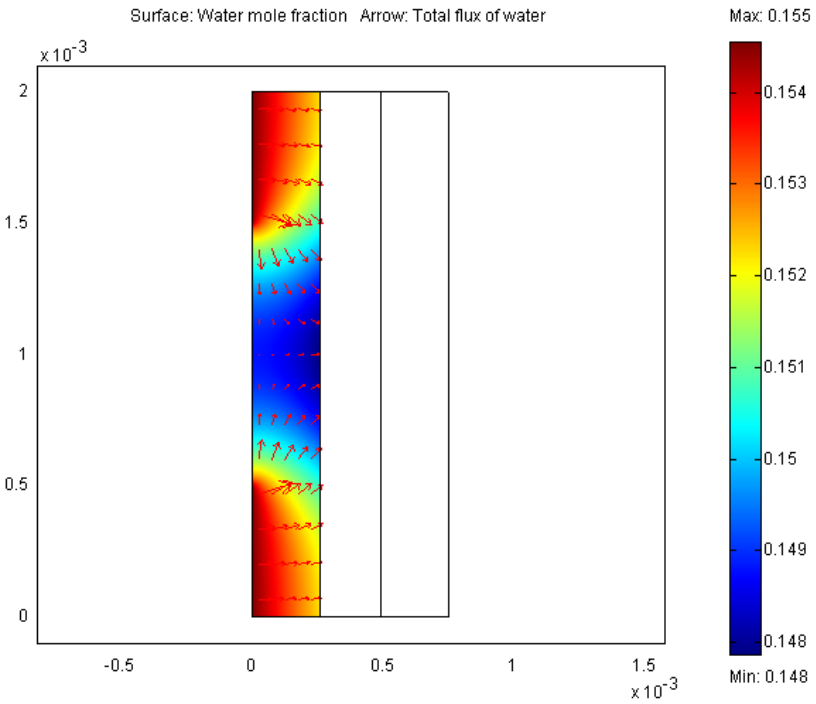

Figure 5.11: Distribution of water mole fraction and the vector field of total water flux at the anode

The current density profile affects the species distribution as shown in Fig. 5.10. Near the mid-points of the cathode the chemical reaction is enhanced and as a result at these points more water is generated while more oxygen is depleted. The distribution of water mole fraction is shown in Figure 5.10. In the same figure, flux of water can be seen as the arrow plot. Since the pressure gradient inside the cathode is so small, the transport of the species is diffusion dominated. Thus the total flux vectors of water point from the higher concentration points to the lower concentration points. The arrow plot shows that water tends to leave the cathode from the inlet channels of the gas distributor.

A similar exchange current density profile is expected on the anode membrane interface due the conservation of charge inside the membrane. A current density profile with higher values in the middle promotes the reaction near the middle of the anode. As a result more hydrogen is depleted at these points resulting in a distribution of water mole fraction like the one shown in Figure 5.11. Arrow plot in this figure shows that water is transported from the inlet channels to the membrane interface.

Considering these two figures, it is observed that water mole fraction is greater at the anode side than that at the cathode side. However, concentration of water at the cathode side is greater, because the pressure at the cathode side is more than that at the

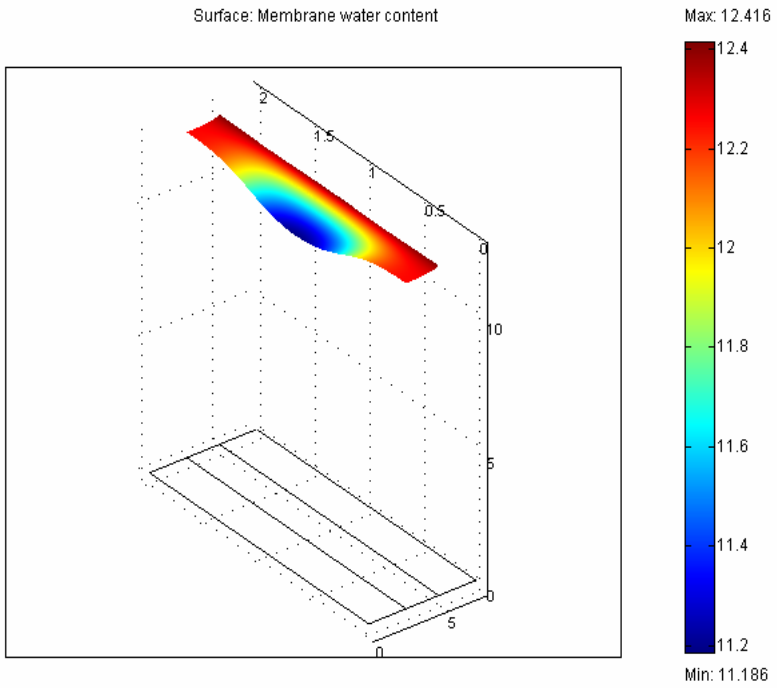

Figure 5.12: Distribution of membrane water content

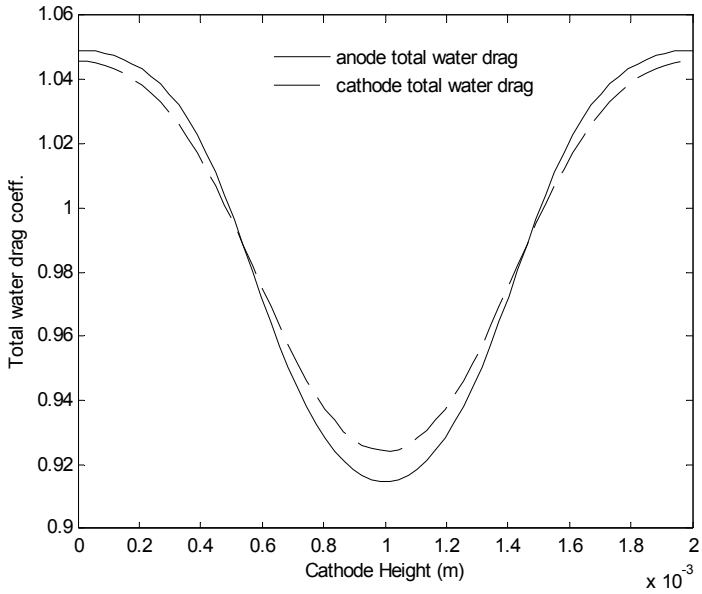

Figure 5.13: Profile of total water drag coefficient (α) on the electrode membrane interfaces.

anode side. Thus water is transported by diffusion from cathode to anode. As a result, as it is shown in Figure 5.12 membrane water content is more near the cathode side. On the other hand, electro-osmotic drag is from anode to cathode and it is the dominant phenomenon in the total water transport as shown by the direction of the arrows in Figures 5.10 and 5.11 from anode to cathode.

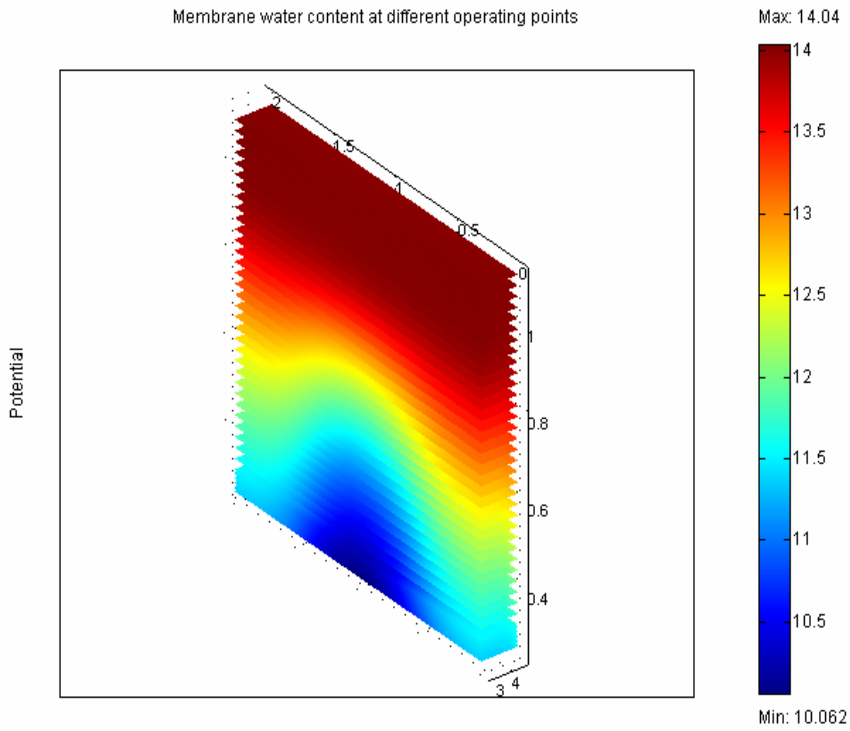

Figure 5.14: Distribution of membrane water content for different cell voltages

Figure 5.13 shows the total water drag coefficient (α) profile on the membrane electrode interfaces. α was defined as

$$\alpha = -\frac{F}{i_{a,c}} m.D_w \frac{\partial c_w}{\partial y} + n_d$$

Assuming the positive direction from anode to cathode, it can be seen from this figure that the effect of electro-osmotic drag is very strong. The reason of the bump in the profile for the anode side is that electro-osmotic drag coefficient is smaller in the middle parts due to the lower membrane water content at these points. Though the membrane water content is relatively greater at the cathode side there is a bump in the profile also for the cathode side. This is because diffusive term in α is relatively bigger. It tends to switch the direction of the water transport from cathode to anode; thus total water drag coefficient decreases at the middle parts of the cathode. Also, it should be noted that the profiles both on anode and cathode interfaces are similar thanks to the conservation of mass for water. These profiles explain the water mole fraction distributions shown in Figure 5.10 and 5.11 exactly.

Figure 5.14 shows the distribution of membrane water content for different cell voltages. It is observed that for lower cell voltages, membrane water content decreases. This is because at higher current densities, electro-osmotic drag is enhanced and the

water inside the membrane is transported to the cathode. Due to the concentration gradient inside the cathode water diffuses through the gas channels and leaves the cell.

5.1.3 Dynamic Analysis with CFD Model

A step input in voltage is given as it is shown in Figure 5.15. Simulations are carried out with the two modeling approaches for water transport. First, equilibrium of water is assumed across the membrane-electrode interface and equilibrium sorption values are chosen as boundary conditions for the equations governing the water transport inside the membrane. Secondly, non-equilibrium assumption is considered and flux boundary conditions are imposed as it was explained in the modeling section. For the equilibrium case the current density is found to be bigger than that of the non-equilibrium case. As it was explained in the modeling chapter, for non-equilibrium assumption there may be possible losses of water vapor to the surrounding stream; thus it is expected that there is less water in the membrane for non-equilibrium case which lowers the current density output of the cell. Also, it is observed from Figure 5.22 that for the non-equilibrium case, undershoot is deeper.

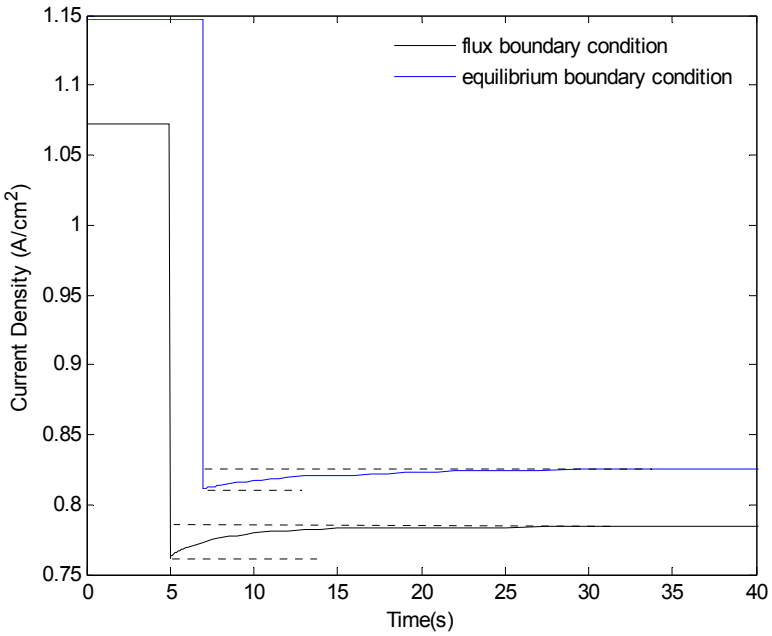

Figure 5.15: Dynamic responses of average current density to a step change in cell voltage such that it increases from 0.5 V to 0.6 V at t=5 s.

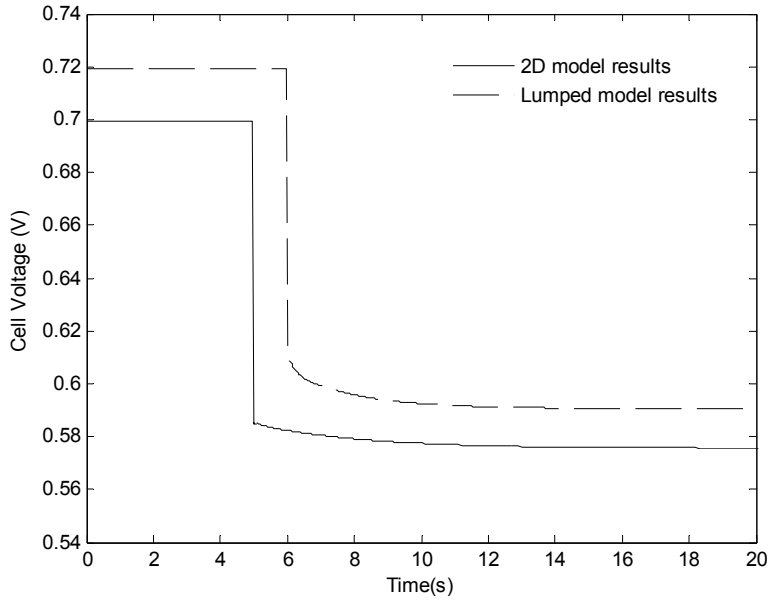

Figure 5.16: Dynamic responses of the average cell voltage for CFD model (solid) and lumped model (dashed) to a step change in cell voltage such that it increases from 0.5 V to 0.6 V at t=5 s.

Figure 5.16 shows dynamic responses of cell voltage for both lumped and 2D models to a step input in current density such that it increases from 0.5 A/cm^2 to 0.85 A/cm^2. Responses for both models are similar. As it was explained before, initial jumps are due to instantaneous electrochemical reactions. Transients following the jumps are chiefly due to the transient of the water transfer mechanism across the membrane. Both curves settle down after about 10 seconds consistent with the theoretical diffusional time scales.

Figure 5.17 shows the distributions of water mole fraction and the membrane water content at initial and final states associated with this input. It is observed that there is less water in the membrane at the final state, which is responsible for the gradual decrease in cell voltage after the initial jump. It is also seen that anode water content also decreases due to the water transported from anode to cathode by electro-osmotic drag which is enhanced at higher current densities. Along with the water transported from anode to cathode side, water is produced more at the final state. As a result cathode water content increases. It should be noted that the color scale given in the figure is related to the membrane water content. The color scales for water mole fractions at the electrodes are different and they are not given.

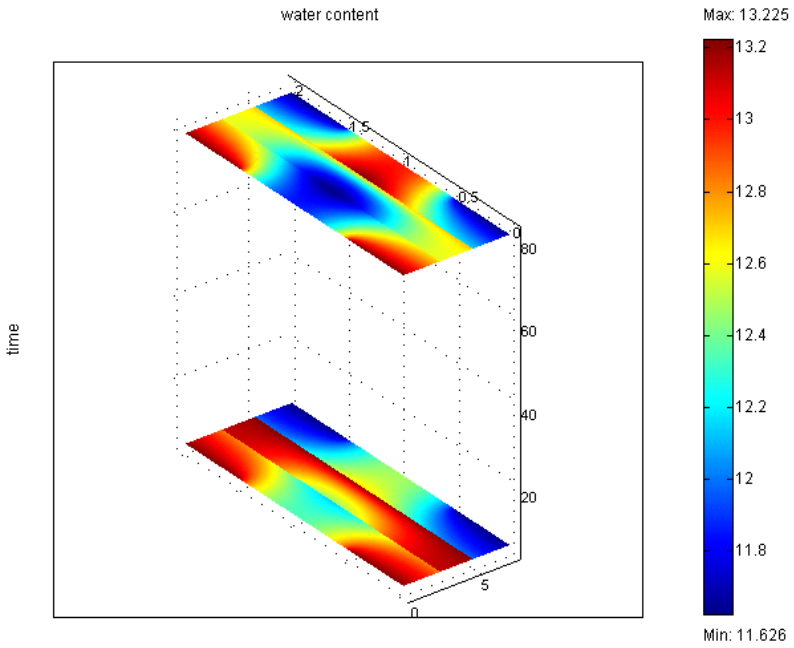

Figure 5.17: Distribution of membrane water content and water mole fractions at the electrodes at the initial (below) and the final (above) states for fully humidified air. (Color scale in each domain is different; the given one is for membrane).

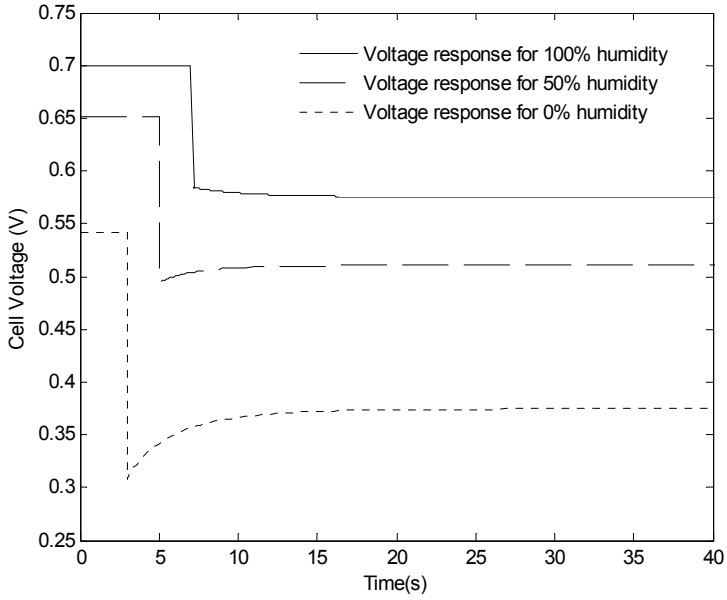

Figure 5.18: Dynamic responses of the average cell voltage for different values of relative humidity of the air to the same input as in Figure 5.16. (__) for 100% humidified air, (_ _) for 50% humidified air, (…) for dry air

Figure 5.18 compares the voltage responses for fully humidified air, 50% humidified air and dry air to the same input. At the steady state, prior to and after the transient, increasing relative humidity (RH) of the cathode air yields higher cell potentials for a given current density, which is akin to higher conductivity of the membrane from the relationship given for κ in Table 3.3. For 50% and 0% humidity at the cathode inlet, the cell voltage increases from its value immediately after the initial jump; the behavior reverses in the case of RH=100%. When the cathode RH is 100%, as the anode's, the membrane is almost fully hydrated, and when the current is drawn, electro-osmotic drag significantly increases and moves the membrane water into cathode. Despite the increased production at the cathode side, back-diffusion cannot compete with the increased rate of the electro-osmotic drag. This is the case where the cathode flooding is most likely to take place, which can only be captured with a multiphase model. As the water content of the membrane drops slightly, a very small but gradual decrease in the cell potential takes place during the transient. When the air is not fully humidified, membrane uptakes water that is generated at the cathode, resulting in a gradual increase in cell potential after the initial jump. Dynamics of average membrane water content is shown in Figure 5.19.

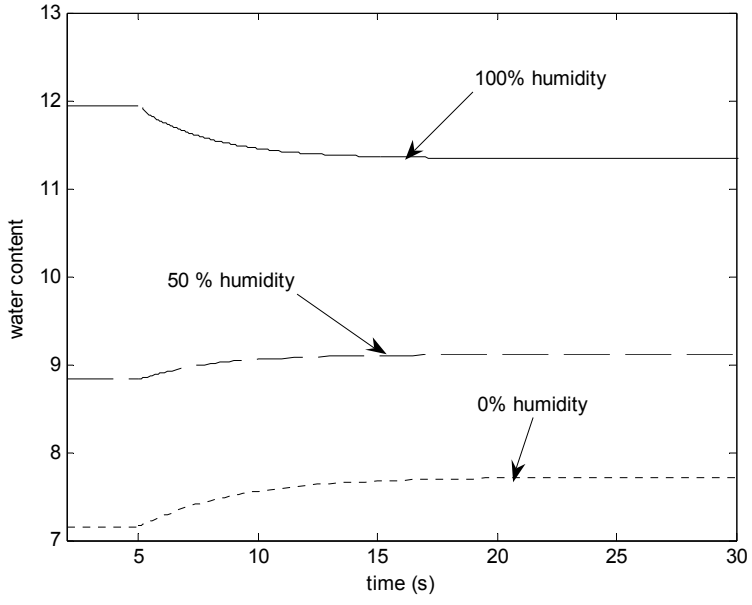

Figure 5.19: Dynamic responses of average membrane water content for different values of relative humidity of the air to the same input as in Figure 5.16.

However, admittedly, our model is far from demonstrating the realistic physical condition, which is governed by the phase transition at the cathode, when the partial pressure of water is above its saturation value. In fact, in some of our 2D simulations water activity levels are above one, for which the use a vapor only model is subject further experimental validation. For the sake of consistency model is studied in the range that water activity is below or slightly above one.

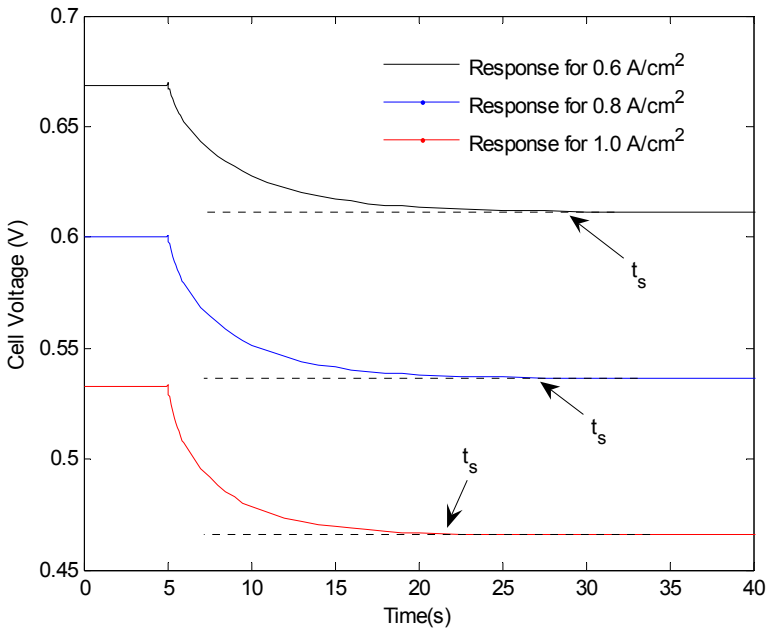

Figure 5.20: Dynamic responses of average cell voltage for different current densities (0.6 A/cm^2: black, 0.8 A/cm^2: blue, 1.0 A/cm^2: red) to a step change in relative humidity such that it changes from 100% to 50%.

Humidity of air is changed from 100% to 50% at t=5 s and dynamic responses of cell voltage at 0.6, 0.8 and 1 A/m^2 are seen in Figure 5.20. In all three cases, as the cathode's water concentration drops instantly, the membrane's water content, and the ionic conductivity of the membrane gradually decrease in the transient, and the cell voltage follows that. Thus, fast initial transients are not observed in this case. It is observed that settling time of the system is bigger for lower current densities. At lower current densities, cathode water content is less mainly due to the lower production rate so membrane releases more water to the cathode to satisfy the equilibrium. This makes the transient of the response be longer at lower current densities.

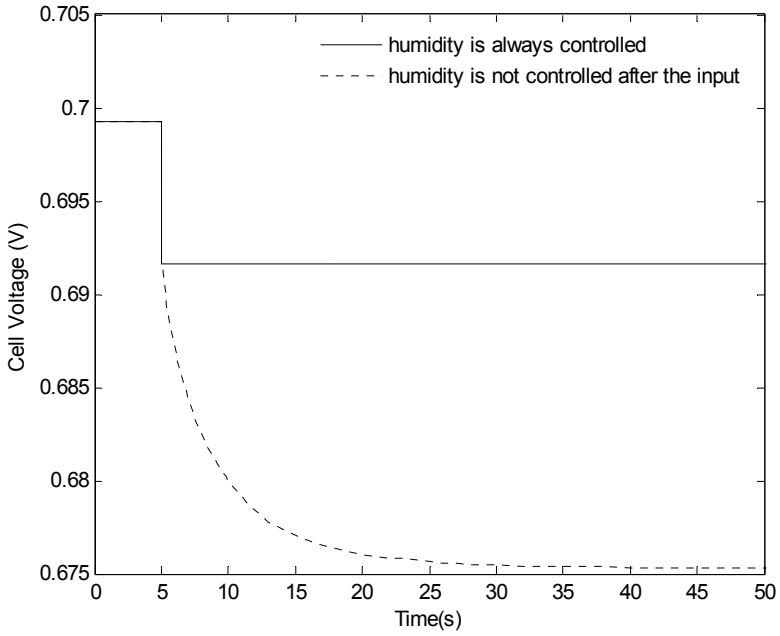

Figure 5.21: Dynamic responses of average cell voltage to a step input in pressure for the cases when inlet gases are always fully humidified (solid) and humidity is not controlled after the input is given (dashed). Pressure decreases from 5 atm to 4 atm.

Figure 5.21 shows the voltage response of the system to a step change in pressure of air from 5 atm to 4 atm at 0.5 A/cm^2 for two cases. In the first case, at the cathode inlet always fully humidified air is supplied. It is assumed that humidity of the air is controlled so as to maintain fully humidified gases at the inlet. In the other case, it is assumed that at the initial state, fully humidified air enters the cathode but there is no humidification control; so when the pressure drops to 4 atm. RH of air decreases from 100% to 80%. Dynamic responses show that for the humidity controlled case, responses are so fast that system settles down just after the input is given. For the second case, after the initial jump in the response, long transients are observed due to the dynamics of water transfer. In the first case since the humidity is controlled and constant values are always maintained, partial pressures of species does not change during the response. Dynamics of water transfer which is chiefly governed by the difference in partial pressure of water is not seen in the humidity controlled case. Concentration of oxygen changes when the pressure is altered which results in a sudden drop seen in the cell voltage response. This drop is also observed in the other case. Dashed line that takes apart the difference between two responses, actually shows the standalone effect of water transport transient.

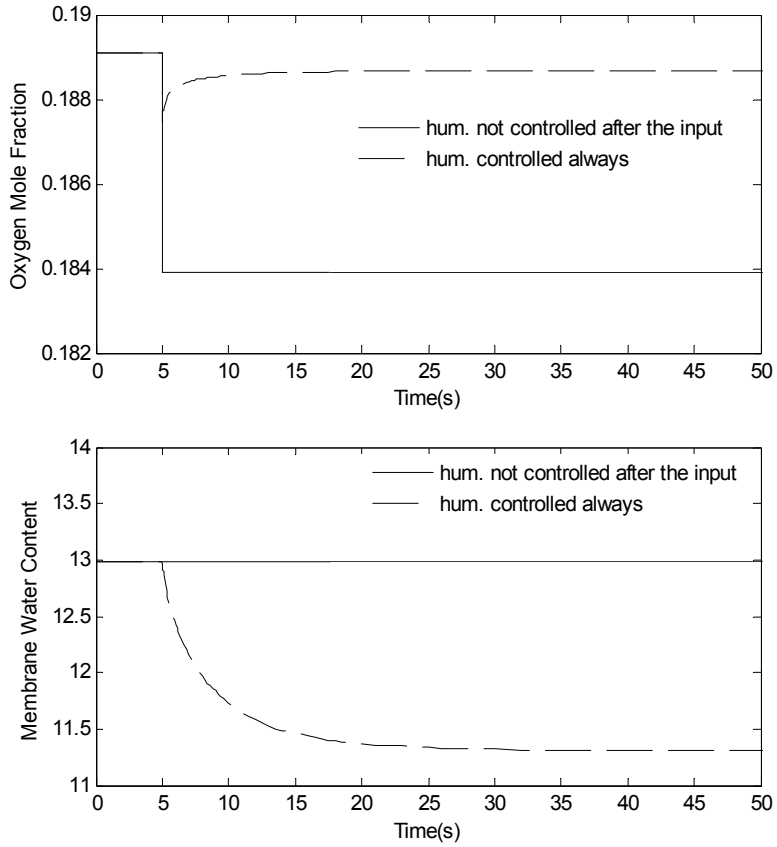

Figure 5.22: Dynamic responses of average oxygen mole fraction and membrane water content to the same input as in Figure 5.21.

Dynamic responses of membrane water content and oxygen mole fraction which explains overall transients are seen in Figure 5.22. Here it should be noted that the gradual increase in oxygen mole fraction after the initial jump is so small that it does not prevent the decrease in cell voltage due to the lessening of membrane water content.

Comparing Figures 5.4 and 5.21, it is observed that after the initial jump, there is a slightly slower transient in lumped model response than that of CFD model to the same input. A whole membrane electrode assembly is taken into consideration in lumped the model whereas a cross-section of MEA is considered in the CFD model. Thus, the settling times differ between two models. However, this difference is attributed to the time scales associated with the transport at the electrodes which are negligible with respect to the time scale of membrane water transport.

5.2 Analysis of a PEMFC with Interdigitated Flow Fields

5.2.1 Steady-State Analysis

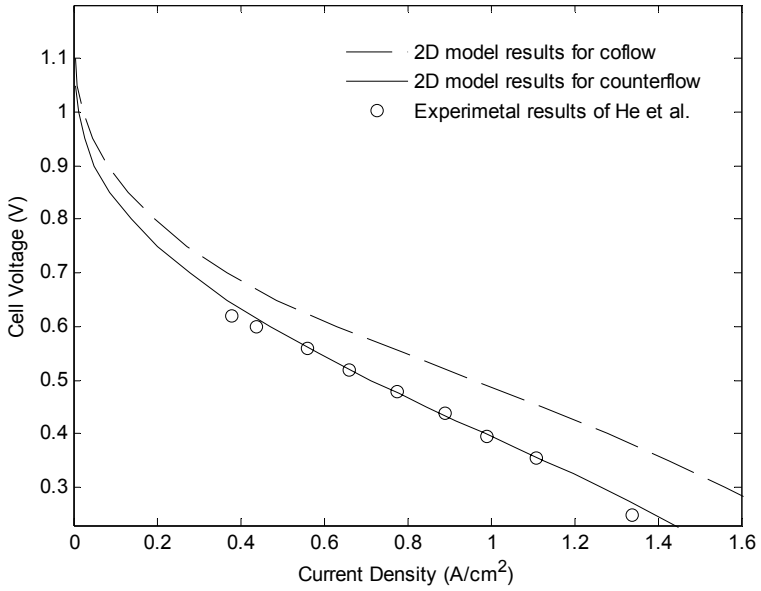

Figure 5.23: Polarization curves for counterflow (solid) and coflow (dashed) cases

With the experiments carried out by He et al with an interdigitated PEMFC [23], the model is validated. Since it is not mentioned in their study, it is assumed that the fuel cell employs counterflow. Dimensions of the cell and the operational parameters of the PEMFC are set to the values used in that study. They are listed in Table 3.9. The polarization curves of the model and the experiments are compared in Figure 5.23. For a considerable range, polarization curve for counterflow model is close to the experimental data. The model results show that at a particular current density, higher voltages are acquired for coflow than those acquired for counterflow. However, for lower current densities, results are approximately the same. The discrepancy between the curves for coflow and counterflow is mainly due to the ohmic losses in the membrane. In the coflow case membrane is more humidified, thus higher voltages are obtained for the same current drawn from the system. At higher current densities, there is not a drastic drop due to the concentration overpotential unlike many of those similar polarization curves. This can be attributed to the interdigitated flow field design, which not only allows more reactants reach the reaction sites but also prevents the product water to clog the electrode pores. However, to capture the exact behavior of the fuel cell in this region, phase transition of water must be included in the model.

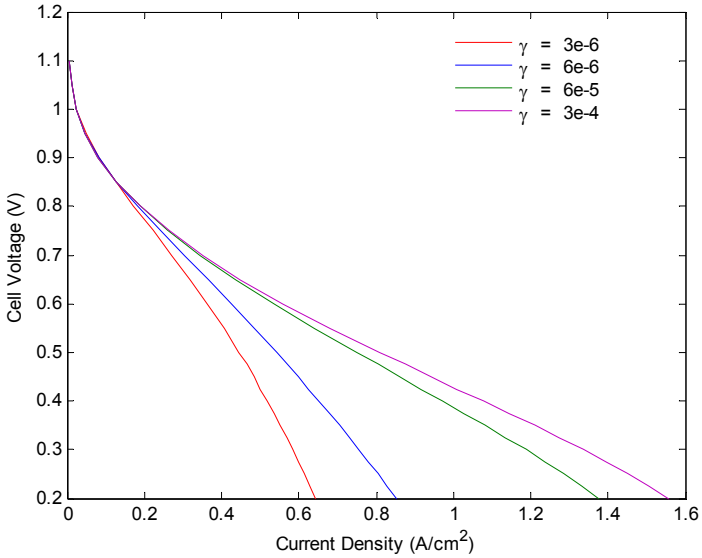

Figure 5.24: Effect of mass transfer coefficient on polarization curve

The effect of the mass transfer coefficient on the polarization curve is shown in Figure 5.24. For greater values of this parameter polarization curve is tilted up. Mass transfer coefficient of water defines the flux of water into and out of the membrane by equations 3.42 and 3.43. If bigger values are selected, it means that less water is lost to the surrounding stream and more water is transported through the membrane. As a result, membrane water content increases. Thus, for higher values of the parameter, ohmic losses diminish. Mass transfer coefficient characterizes the slope of the polarization curve.

Figure 5.25 shows the average membrane conductivity as a function of current density. Unlike the case in conventional design, membrane conductivity increases with the current density. It can be said that though at higher current densities ohmic loss gets bigger they are somehow alleviated by the relative decrease in the ohmic resistance and this will tilt up the polarization curve a bit at higher current densities. This may be another reason why concentration overvoltage is not observed sharply. Between the co-flow and counter-flow cases, there is a switch over in the membrane conductivity. At low current densities, co-flow configuration results in higher membrane conductivity due to higher water content of the membrane, and at higher current densities, counterflow configuration has larger membrane conductivity.

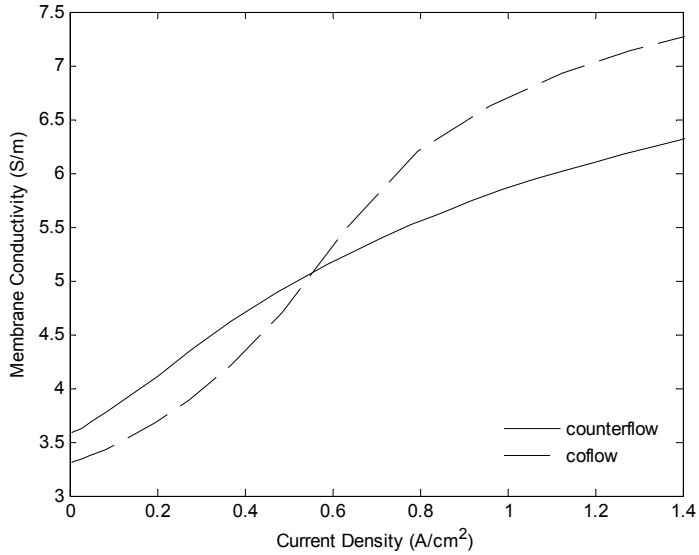

Figure 5.25: Average membrane conductivity at different current densities for counterflow (solid) and coflow (dashed) cases

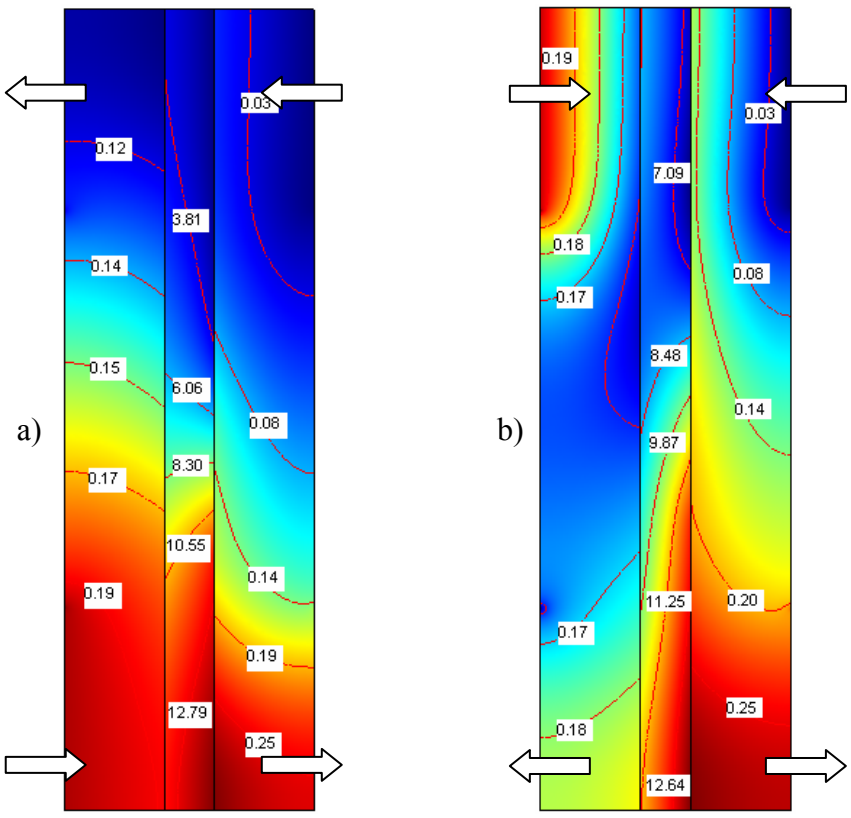

Figure 5.26: Surface and contour graphs of water mole fractions at the electrodes and membrane water contents at 0.5 V for a) counterflow and b) coflow. (Color scales are different at different domains of the MEA and can be figure out from the contour labels)

Figure 5.26 shows the distributions of water mole fraction at the electrodes and membrane water content for both counterflow and coflow cases. It should be noted that fully humidified gas enters the anode whereas dry air goes into the cathode. Thus, for the coflow case, near cathode inlet there is a greater concentration gradient between anode and cathode than that of counterflow case. Hence, at the parts near cathode inlet membrane water content is higher for the coflow case than the counterflow case because more water is transferred due to a greater concentration gradient.

On the other hand, due to the pressure gradient, there exists a convective flow inside the electrodes. This causes the water generated during the reaction to be dragged through the outlet of the cathode, causing the water concentration to be higher at the points of the membrane near cathode outlet than those near cathode inlet. That is the reason why for the coflow water accumulates in the parts near cathode outlet, though it is generated near cathode inlet. Due to this convective flow, parts of the membrane near the cathode outlet are more humidified for both cases. Consequently, transfer current density is higher near cathode outlet because of the overpotential distribution.

However, oxygen concentration which also affects the reaction rate is higher at the points near cathode inlet. Taking into consideration of these two facts, the distribution of the total reaction rate over the catalyst boundary is found to be greater in the middle parts of the electrode as it is depicted in Figure 5.27.

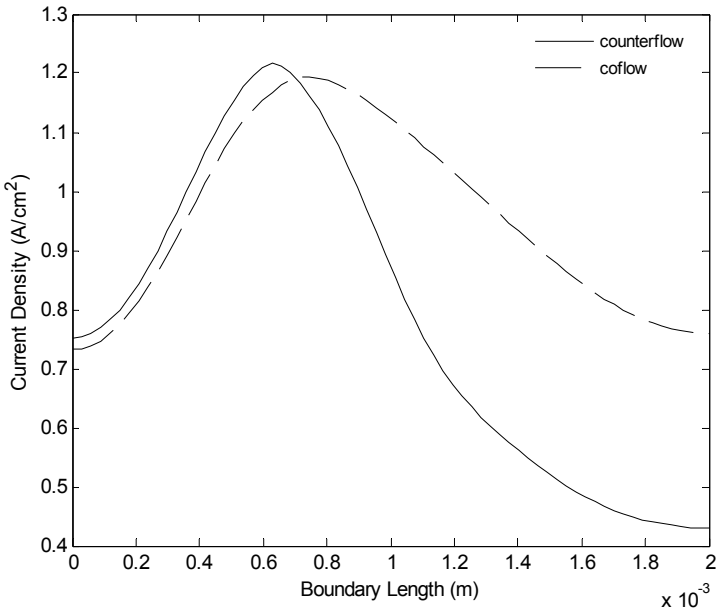

Figure 5.27: Distribution of the transfer current density over the membrane cathode boundary for both cases at 0.5 V.

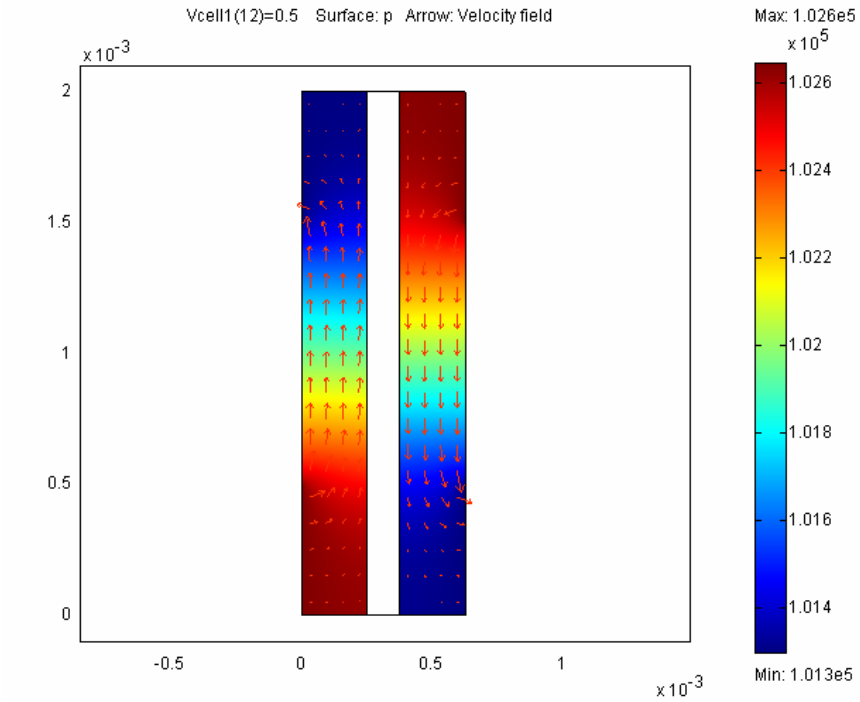

Figure 5.28 Distribution of pressure and vector field of velocity for counterflow

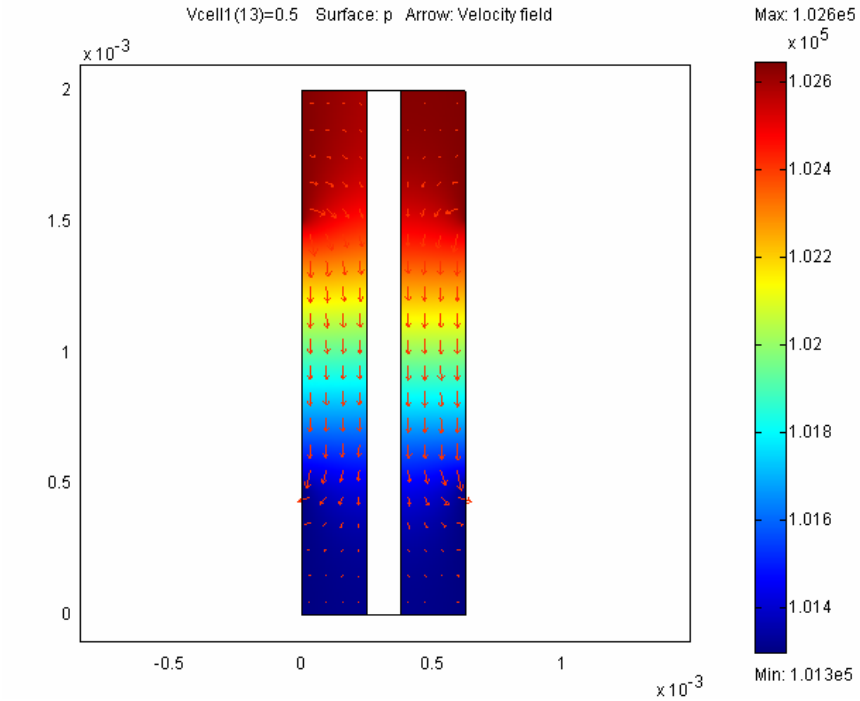

Figure 5.29: Distribution of pressure and vector field of velocity for coflow

The pressure distributions in the electrodes are shown in Figure 5.28 and 5.29 for counterflow and coflow respectively. Velocity field driven by the pressure difference in the electrodes are represented by the arrows in these figures. As it is seen for coflow the velocity field at both anode and cathode is in the same direction. The velocities near the

corners of inlet and outlet channels get very big because these corners are the shortest distance in the flow field. The pressure distribution for coflow is not symmetric due to the net mass transport to the cathode which makes the cathode total pressure a little bit higher.

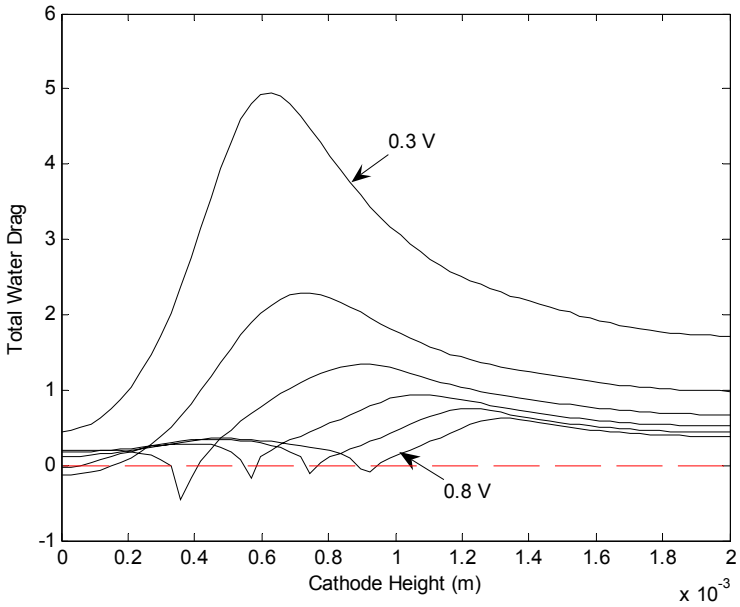

Figure 5.30: Profile of total water drag coefficient (α) on the cathode membrane interface for counterflow.

Figure 5.30 shows the total water drag coefficient profile for different operating voltages. It should be noted that if this coefficient is bigger than zero, the water is transferred from anode to cathode, in other words electro-osmotic drag is dominant. If it is less than zero back-diffusion is dominant and the water is transferred from cathode to anode. The change in the sign of this variable represents the switch-over in the governing water transport phenomena. Not surprisingly it is seen that for lower voltages the coefficient is bigger because of the enhanced electro-osmotic drag at higher current densities.

Notches seen in these profiles represent the local dominancy of the diffusive transport from cathode to anode. As it is seen in the Figure 5.31, which shows the distribution of water mole fractions at corresponding voltages, there are some local regions across the membrane where cathode water content is more than the anode's. As a result, at these points diffusion from cathode to anode is promoted and at specific operating voltages, diffusion overwhelms the electro-osmotic drag. At higher voltages,

notches are observed near the middle of the cathode height. With the decreasing cell voltage the switch-over of the mechanisms begins to occur near cathode outlet, because electro-osmotic drag becomes dominant at a bigger portion of the membrane. For the cell voltages higher than a specific value, all the water transport is utilized by electro-osmotic drag.

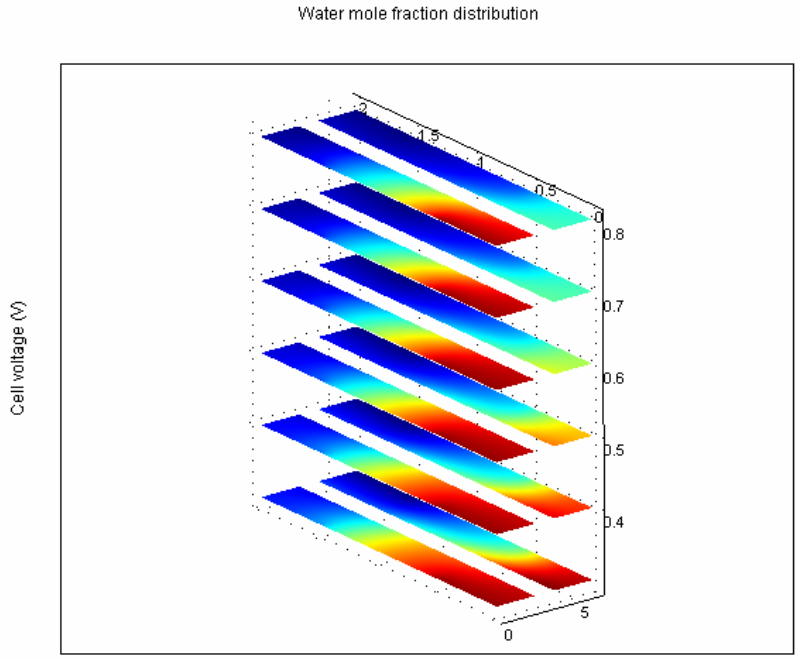

Figure 5.31: Distribution of water mole fractions at the electrodes for counterflow (color scale in each domain is different; the given one is for membrane).

As it is shown in Figure 5.32, for the coflow case, more water is transported near cathode inlet. With the fully humidified anode and dry cathode inlets, a concentration gradient from anode to cathode exists near cathode inlet. Along with the electro-osmotic drag, water is transported from anode to cathode also by diffusion. However, water is carried from cathode inlet to outlet by the convective flow. On the other hand, outlet of the anode is not as humid as the inlet because of the water left the anode. Thus, near outlets, diffusion from cathode to anode is enhanced and for some operating conditions it overwhelms the electro-osmotic drag. Nevertheless, for lower voltages, electro-osmotic drag is promoted and water is transferred from anode to cathode for a considerably big portion of the MEA.

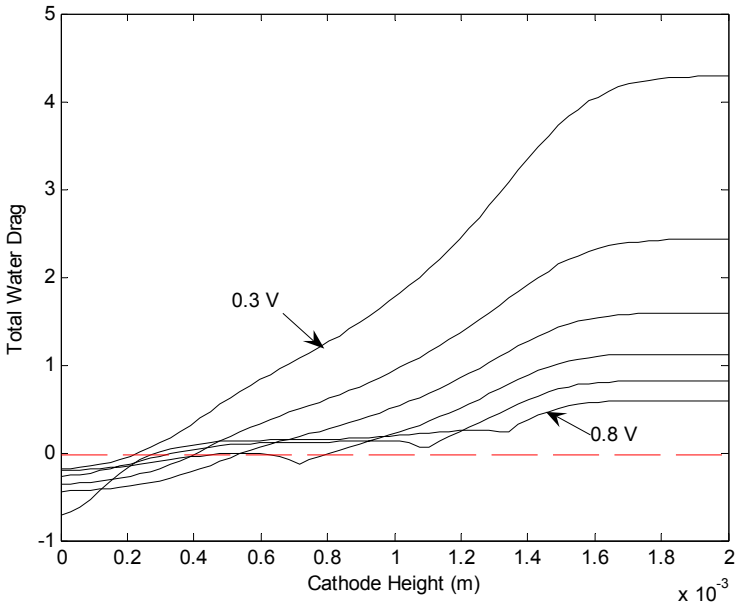

Figure 5.32: Profile of total water drag coefficient (α) on the cathode membrane interface for coflow.

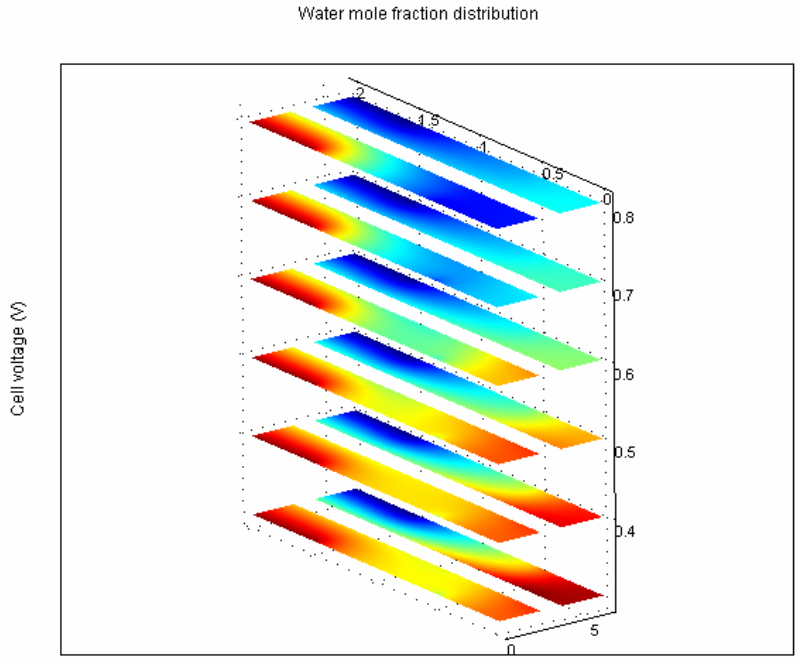

Figure 5.33: Distribution of water mole fractions at the electrodes for coflow (color scale in each domain is different; the given one is for membrane).

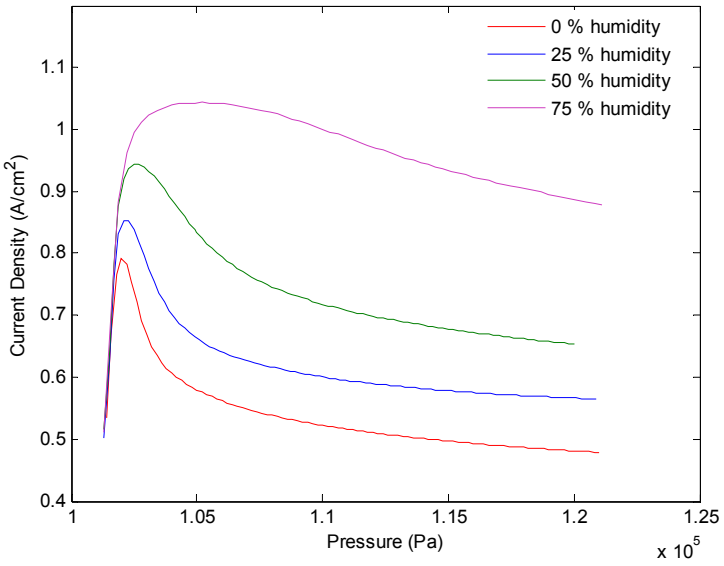

Figure 5.34: Average current density as a function of cathode inlet pressure at different relative humidity for counterflow

An interesting characteristic of an interdigitated fuel cell is observed in Figure 5.34. When the pressure of the air increases, up to a specific value, the current density also increases but afterwards it starts decreasing gradually. This is contrary to the characteristics of conventional fuel cells in which current density increases monotonously as long as the pressure does. The increase in current density is chiefly due to the rise in the oxygen concentration. The degradation of the performance after an optimum value can be attributed to the convective flow inside the electrodes. Despite the rise in the oxygen concentration, the convective flow is enhanced with the increased pressure difference between the inlet and the outlet of the cathode. A stronger convective flow begins to sweep the water out of the electrode. Consequently, membrane water is transferred to the cathode and ohmic losses increases. Thus the current density drops.

Figure 5.35 shows the water mole fraction at the cathode for inlet air pressures of 1.026 kPa and 1.150 kPa. As it is shown in the figure the mole fraction of water is bigger at 1.026 kPa. However cathode water content drops when the pressure difference between the inlet and outlet channels increases. The increase in oxygen concentration is effective in the total current density up to an optimum pressure and then water leaving the cathode kicks the performance of the fuel cell.

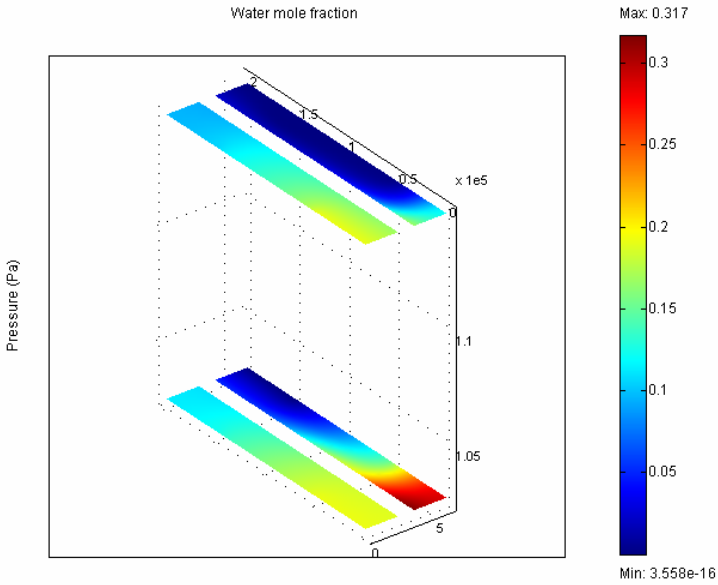

Figure 5.35: Comparison of the distributions of water mole fraction at 1.026 kPa (below) and 1.15 kPa (above) with dry air for counterflow

For different relative humidity values of inlet air, optimum value of the pressure varies. With the higher humidity values, negative effect of convective flow decreases. At 75 % humidity fuel cell can operate within a practical range of pressure without severe degradation of performance. The results taken for coflow are similar and are shown in Figure 5.49.

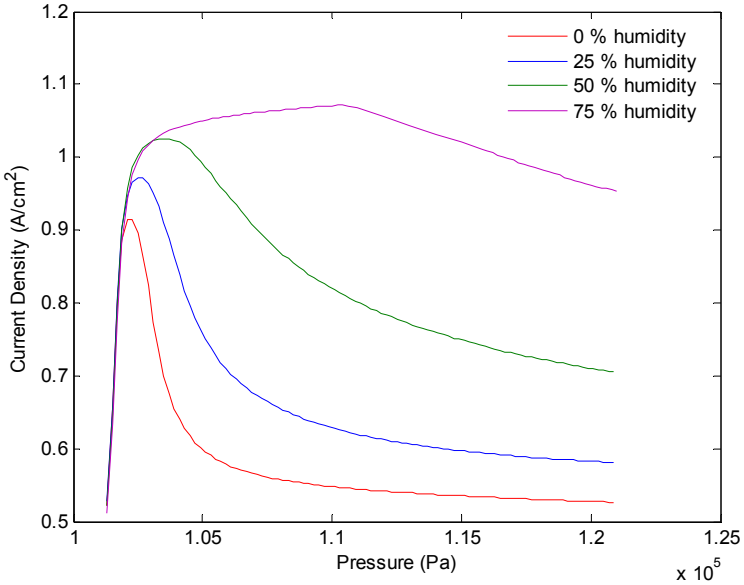

Figure 5.36: Average current density as a function of cathode inlet pressure at different relative humidity for coflow

The effect of RH on the optimum pressure drop that yields maximum current density for a given voltage in the interdigitated fuel cells is very important because it introduces constraints in the operation of the fuel cell and it makes the system difficult to be controlled by adjusting the pressure for different operating conditions

5.2.2 Dynamic Analysis

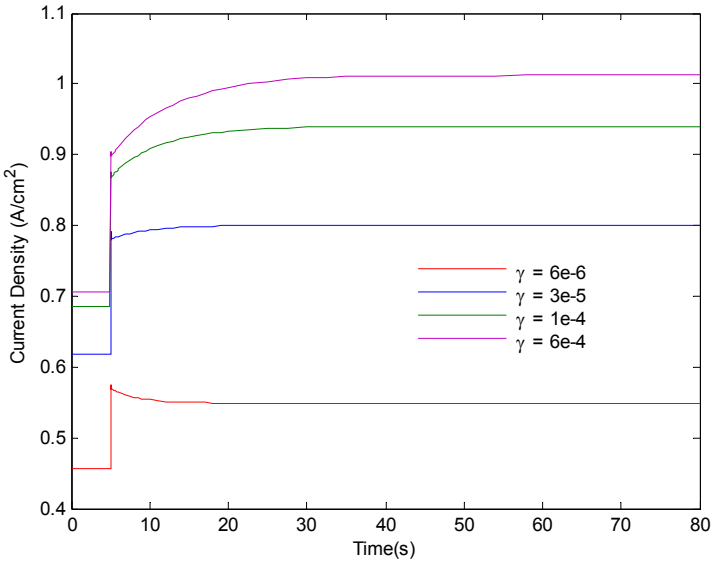

Figure 5.37: Effect of mass transfer coefficient on the average current density response to a step change in cell voltage from 0.6 V to 0.5 V.

Figure 5.37 shows the dynamic response of average current density to a step change in cell voltage such that it changes from 0.6 V to 0.5 V. Since for bigger values of this parameter, the water transport through the membrane increases so does the time scales of water transport. Thus, for larger values of mass transfer coefficient, longer transients are observed. For a small value of mass transfer coefficient such as 6.10^{-6} a different response is observed. Unlike the other cases, for this value of the parameter, current density decreases gradually after the initial jump. This can be explained by the definition of the flux into and out of the membrane. For example at the cathode interface water flux out of the membrane is defined as (Eq. 3.47),

$$j_{w,c} = m.\gamma.(c_w - c_w^c) - (n_d + 1/2)\frac{i_c}{F}$$

Mass transfer coefficient appears in the first term. For the smaller values of this parameter second term in this equation becomes dominant which is the electro-osmotic drag. As a result for smaller values of mass transfer coefficient, water is moved into cathode by electro-osmotic drag. Thus, current density drops after the initial jump.

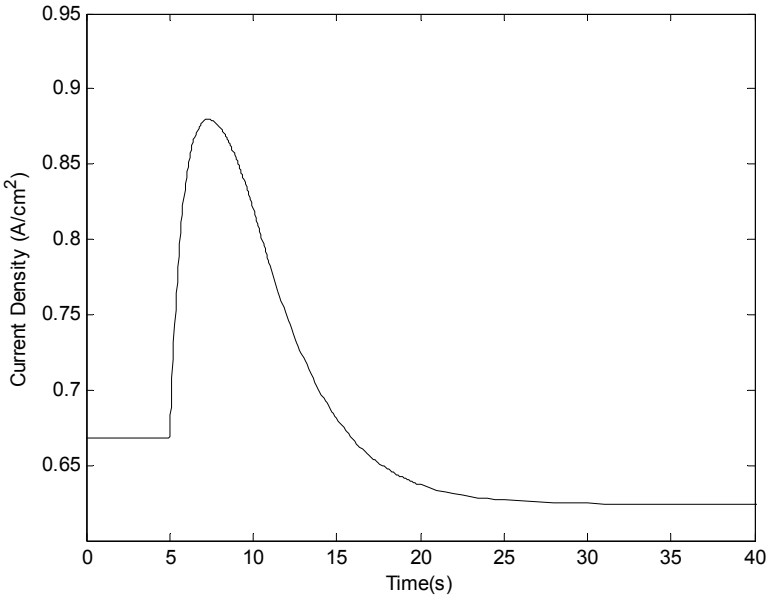

Figure 5.38: Dynamic response of average current density for counterflow to a ramp input in air pressure such that it changes from 1.016 kPa to 1.036 kPa in 5 s.

Figure 5.38 shows the dynamic response of average current density to a ramp input in air pressure which is shown in Figure 5.51. For dry air fed into the cathode, the optimum pressure is about 1.025 kPa. With the initial pressure below this value, current density increases but then it starts to drop gradually as it shifts from one regime to another as outlined in Figs. 5.34.

In Figure 5.39 dynamic responses of average current density to a step voltage drop from 0.5 V to 0.4 V for both 50 % humidified air and dry air are observed. An overshoot is observed in the response for 50 % humidified air. Oxygen is depleted in the reaction sites instantaneously increasing the current density. However, with the poor oxygen content, current density drops after this jump which happens in a fraction of a second. The transient which lags this overshoot is due to the water transport in the membrane. The transients observed in Figure 5.39 fade away in the range of the theoretical time scale estimates.

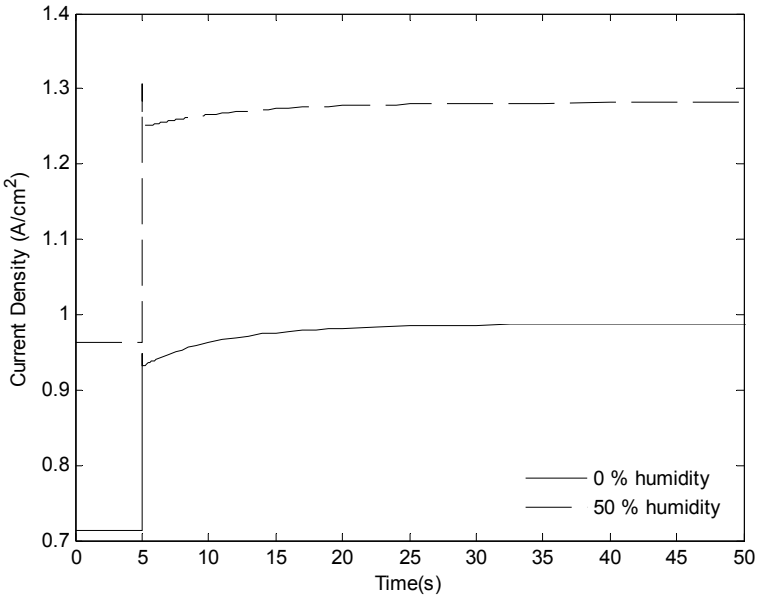

Figure 5.39: Dynamic responses of average current density with dry (solid line) and 50 % humidified air (dashed line) for counterflow to a step input in cell voltage from 0.5 V to 0.4 V.

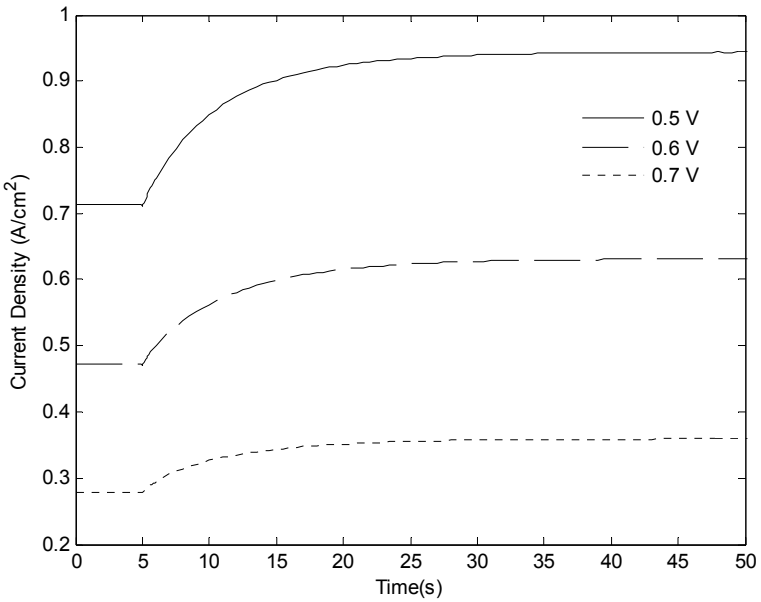

Figure 5.40: Dynamic responses of average current density at different cell voltages (__: 0.5 V, _ _: 0.6 V, …: 0.7 V) for counterflow to a step change in relative humidity such that it changes from 0% to 50%.

Dynamic responses of the average current density to the step input in humidity that is shown in Figure 5.40 are observed at 0.5 V, 0.6 V and 0.7 V. As the humidity of the cathode increases, water is transported to the membrane. If the operating voltage is higher, less water is produced during the reaction at the cathode and it takes more time to supply the necessary water for the membrane at the final state. Thus, time scales of the responses for lower voltages are longer.

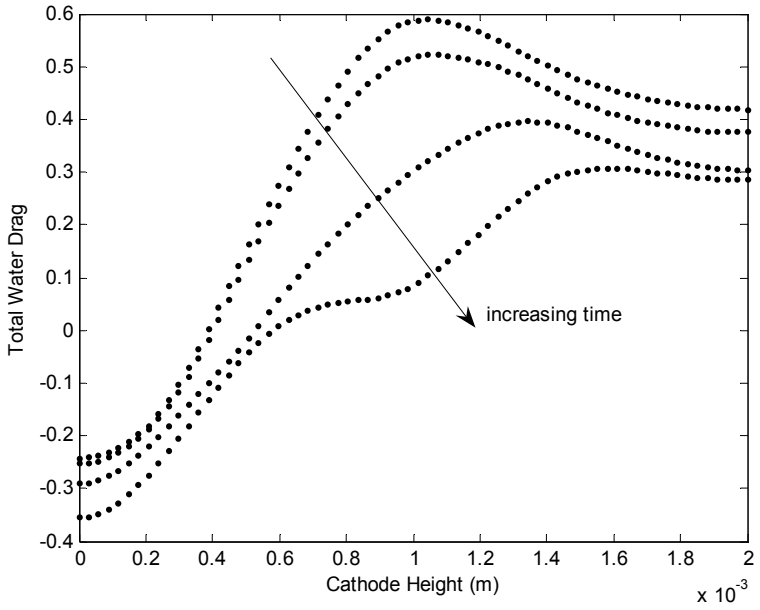

Figure 5.41: Evolution of total water drag coefficient on the cathode membrane interface for counterflow at 0.5 V to the same input as in Figure 5.40.

For 0.5 V operating point, the distribution in the total water drag over cathode membrane interface at 5th, 9th, 15th and 23rd seconds are seen in Figure 5.41. With the positive direction from anode to cathode it can be said that the water transferred from anode to cathode decreases gradually if humidity of air increases which is already expected because back diffusion of water becomes more dominant due to the raise in water concentration at the cathode.

The evolution of the water profiles at a horizontal line passing from the center of the membrane can be seen in Figure 5.42 for the same input. Dashed lines represent the water profiles for time values of t=5, 7, 8, 9, 10, 12, 15, 20, 30, 42 sec. Here the effect of two mode water transfer mechanism can be seen as jumps are observed across the electrode interfaces. These jumps are found to be greater when voltage is less. At higher

current densities, sinks and sources at these boundaries will be greater because both electro-osmotic drag and water generation is proportional to current density.

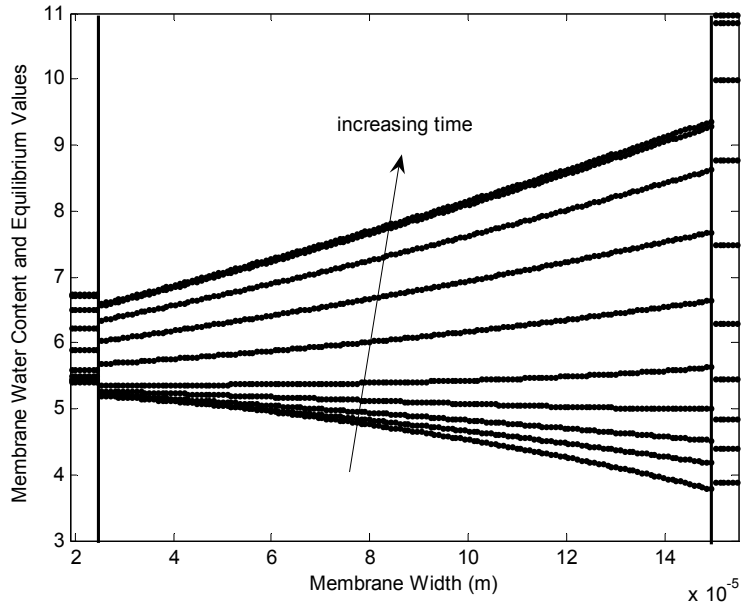

Figure 5.42: Evolution of water profiles in the membrane for counterflow at 0.5 V.

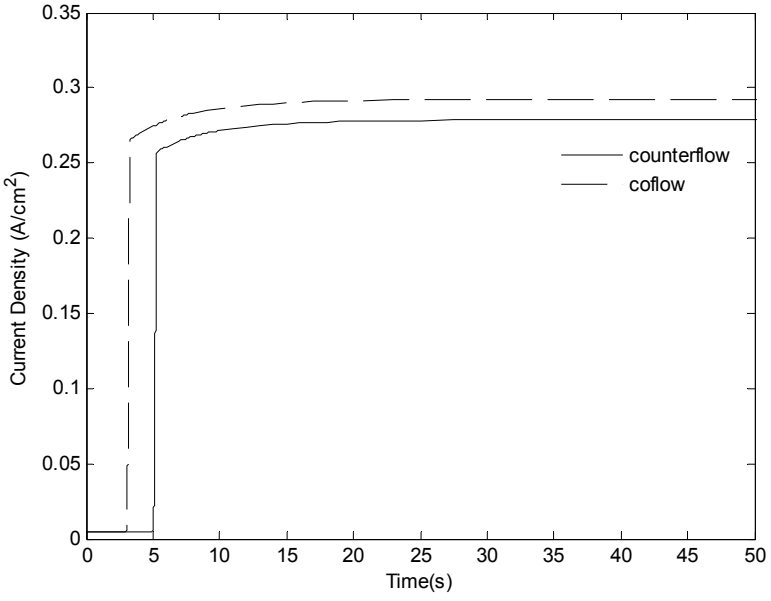

Figure 5.43: Dynamic responses of average current density at start-ups from 1.1 V to 0.7 V with dry cathode inlet air and 1.013 atm constant pressure for counterlow and coflow.

Figure 5.43 shows the dynamic response of the average current density to a step change in voltage from 1.1 V to 0.7 V for dry cathode air and cathode inlet pressure of 1.013 atm. The initial jump shown in the figure is due to the instantaneous chemical reaction. After this initial fast transient a transient of 15-20 seconds is needed for the system to settle down. As asserted in previous studies, this dynamics governed mainly by the water transfer through the membrane. Time scale for coflow is a bit longer than that of counterflow because as stated in Figure 5.26, for coflow more water is accumulated in the membrane under same operating cell voltage. So it takes the membrane longer time to uptake greater amount of water.

In Figure 5.44 dynamics of the system to a step change in both cell voltage from 1.1 V to 0.7 V and cathode inlet pressure from 1 atm to 1.013 atm is shown. Overshoots are observed in the average current density response. As it is seen in Figure 5.34, a rise in pressure from 1 atm to 1.013 atm increases the current density. Thus, if pressure is increased at the same time as the voltage is decreased; more current density is generated through the chemical reaction. This raises the curves in Figure 5.43 resulting in overshoots in the system responses.

If the magnitudes of the overshoots are considered, it can be seen that maximum current density values are approximately the same for both flow types. In fact, the main reason that different current densities are drawn from the system for two flow types under same operating voltage is the different amounts of water accumulated in the membrane. The flow and the diffusion of species in the electrodes play a secondary role. Since the transient of water transport lags the fast transient of chemical reaction, it is expected that same current is drawn for both flow types just after the immediate voltage demand from the system. After the transient associated with the water transport fade away, different steady state values of current densities are observed for each case.

Because of the overshoots in the responses, reaction rate is boosted for a period of time and oxygen is depleted more than needed and more water is generated than the steady state. This retards the water transfer through the membrane; thus it takes longer time for the system to settle down. Since the % overshoot is relatively bigger for counterflow, transient regime for this case is slightly longer than that of coflow.

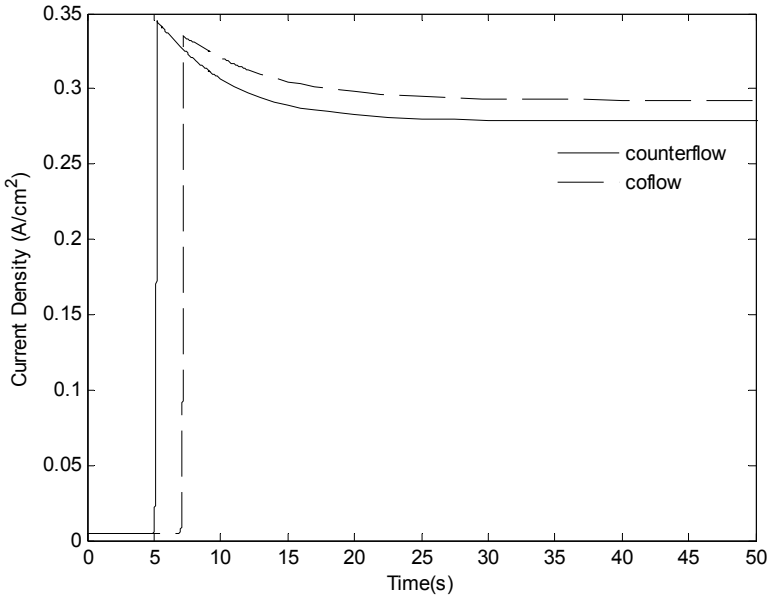

Figure 5.44: Dynamic responses of average current density at start-ups from 1.1 V to 0.7 V and a simultaneous change in air pressure from 1 atm to 1.013 atm with dry cathode inlet air for counterlow and coflow.

Figure 5.45 shows the dynamic responses in the average current density to inputs in both cell voltage and cathode air pressure for counterflow simulating the start-up of the system. The effect of the starting time of the compressor to change the air pressure from 1 atm to 1.013 atm is investigated in three cases; voltage input is given in the presence of steady state pressure of 1.013 atm, pressure is changed simultaneously with the voltage change, pressure is changed 1 second after the voltage input. In the cases when the pressure input is given at the same time of the voltage input and 1 second after the voltage input, overshoots are observed in the responses. Just after the voltage drop, current density increases. Since the pressure input is given at a higher current density, the overshoot is observed to be bigger in the third case. The overshoot would be bigger if the pressure input were given later. Because of the overshoots experienced in the second and third cases, settling times associated with them are bigger than that of the first case. If the start-up of the fuel cell is under consideration, concerning with the overshoot dynamics and the time scales of the responses, it can be concluded that voltage change should take place after the pressure is altered and the system is settled down.

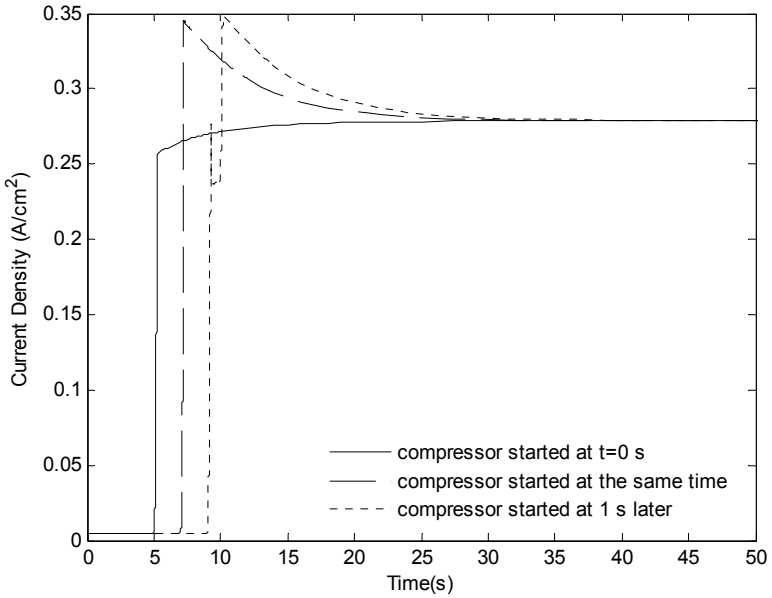

Figure 5.45: Comparison of start-ups for counterflow from 1.1V to 0.7 V with dry cathode inlet air for pressure inputs given before the voltage input (___), at the same time of the voltage input (_ _), given 1 s after the voltage input (…).

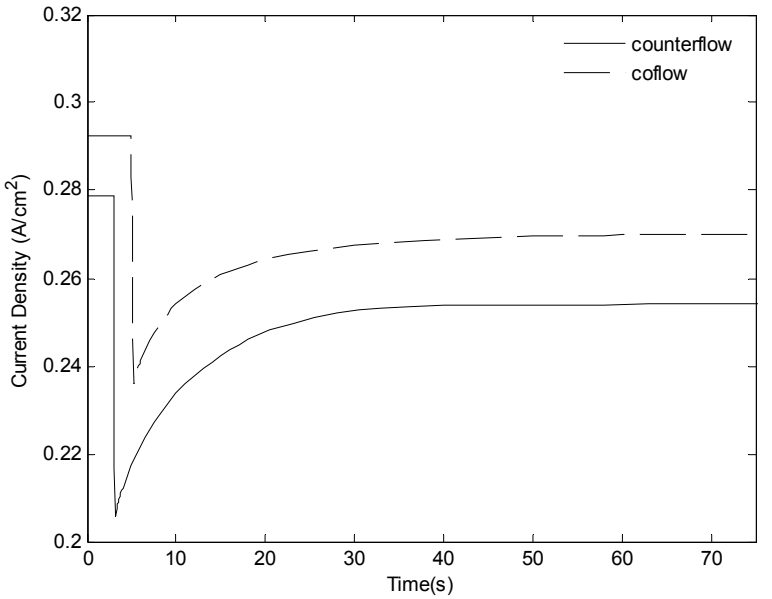

Figure 5.46: Dynamic responses of the average current density to a pressure drop from 1.013 atm to 1 atm for 0% humidity at 0.7 V

Figure 5.46 shows the failure condition such that the air pressure drops suddenly from 1.013 atm to 1 atm due to some malfunction in the air supply system. At 0.7 V operating voltage, the responses in average current density for coflow and counterflow

are similar. Maximum undershoots of almost 80% are observed in the system response for both cases. Due to these undershoots; transient regime of the system is prolonged. The undershoots can be explained as following: When the air pressure decrease the cathode gas mixture becomes poor with oxygen. Thus, sudden drops are observed in the current density responses just after the pressure drop. However, If the steady state plots in Figure 5.47 are considered, it can be seen that at t=80 s water content in the cathode is more than that of t=0 s. So, membrane water content increases, enhancing the current density gradually.

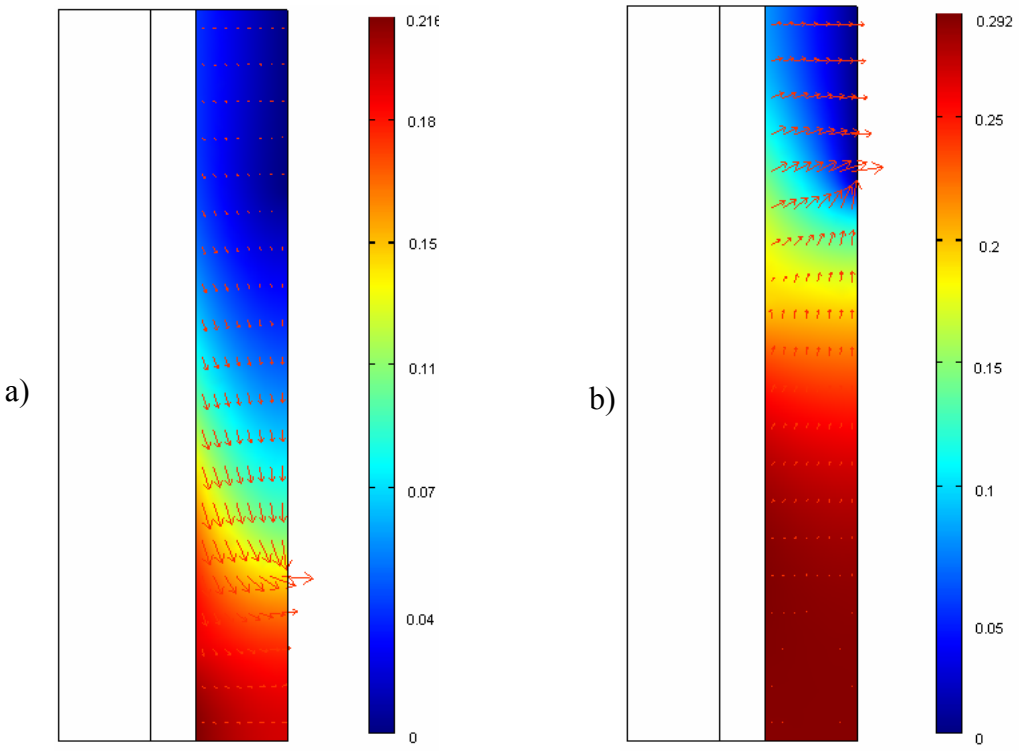

Figure 5.47: Distribution of water mole fraction at the cathode and arrow plot showing the total flux of water at the cathode for counterflow at a) t=0 s b) t=80 s for the conditions in Figure 5.63.

The distribution of water mole fraction in the cathode electrode at t = 80s is shown in Fig. 5.47-b. According to the arrow distribution for the total flux of water, there is no transport of the species with convection but diffusion because of the zero pressure difference between cathode inlet and outlet. Thus, eradicating the main advantage of the interdigitated PEMFC, product water can not be dragged with the advection of the fluid through the outlet channel. Because of the dry air boundary

condition at the cathode inlet, water produced at the membrane boundary diffuses through the cathode inlet. This result is an artifact of setting the boundary condition for the cathode inlet. More accurate boundary conditions must be used here, which is not straightforward. Further, as it can be concluded from Figure 5.47, increasing partial pressure of the water causes more liquid water to exist inside the cathode. In the actual flooding mechanism, liquid water clogs the pores of the cathode by which oxygen molecules are hindered to reach the catalyst sites resulting in concentration overvoltage. Undoubtedly, in order to cover the complete dynamics associated with this phenomenon, the model should include two-phase flow. However, single phase model is capable to give practical insights. Especially for the activity levels less than unity, the model results can be interpreted confidently.

Figure 5.48 shows the dynamic responses of average current density for counterflow and coflow to a drop in relative humidity of the air from 0.5 to 0 at 0.6 V constant operating voltage simulating a sudden failure in the humidity control system. It is seen that such a drop in the humidity of the air affects the system performance significantly. A drop of 35% in current density is observed for coflow whereas there is a drop in current density about 25% for counterflow. Thus, coflow is said to be more reliant on the robustness of the humidity control system.

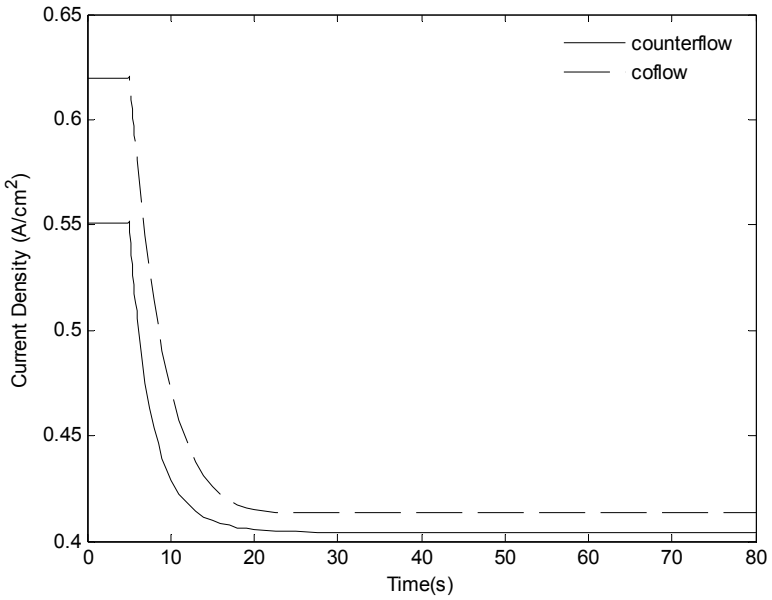

Figure 5.48: Dynamic responses of the average current density to a drop in cathode relative humidity from 0.5 to 0 for 1.05 atm at 0.6 V.

CHAPTER 6

CONCLUSIONS

A 2D finite element CFD model, including coupled partial differential equations of mass, momentum and charge conservation inside a membrane electrode assembly of a PEMFC is developed for the design and operational aspects of the system. The CFD model is solved for MEAs of PEMFCs with conventional and interdigitated gas distribution channels. For the PEMFC with interdigitated flow fields both coflow and counterflow designs are studied. Transient responses of the fuel cell system to changes in cell voltage, air pressure and relative humidity of air are investigated for each design in conjunction with the effects of these parameters on the steady-state behavior of the system. Furthermore a dynamic lumped model based on the formulation of Pukrushpan et al. (2003) is developed using the principles of electrochemistry, thermodynamics and mass transfer with the addition of membrane's transient water transport. Models are validated by comparing the polarization curves with the experimental data of Ticianelli et al. (1988) for MEAs with conventional gas distributors and He et al. (2000) for MEAs with counterflow interdigitated gas distributors along with the comparisons of the transient results with the theoretical estimates of time scales.

The results of the CFD model for conventional design and the lumped model results are found to be comparable. There are some small discrepancies between the lumped model results and the exact data due to neglecting of spatial variations. Lumped Model is also restricted with the assumption such that the inlet gases are fully humidified. However with the inclusion of the membrane water transients, it proves to be a good substitute for the 2D model in PEMFC's system integration and control studies.

Performances of the coflow and counterflow designs for a PEMFC with interdigitated flow fields are found to be similar, with a slight advantage for the coflow

design due to enhancement in the membrane water uptake mechanism in the light of the outcomes of the study of water profile evolutions for each flow types.

For the interdigitated flow fields, current density is observed to be enhanced up to a point with the increasing inlet air pressure; however, it diminishes gradually beyond that optimum level. This behavior is unlike the one observed for the conventional flow fields where the current density increases monotonously with the increasing air pressure. This contradiction is found to be due to the enhancement of the convective flow inside the cathode with the increasing pressure difference. This sweeps the water out of the cathode and consequently the membrane dehydrates resulting in degradation in current density

Water transport inside the membrane is the main interest of this study. The key point of water management in the model is the assumption that water vapor at the electrodes is not in equilibrium with the solute water in the membrane. A method for water management with a similar assumption proposed by Berg et al. (2004) is implemented into our model.

In all of the designs, it is observed that water transport in the membrane is the dominating phenomenon in dynamic behavior of PEMFC; transient responses are consistent with estimated theoretical time scales. Also, it is shown that transient of water transport is longer in a PEMFC with a thick membrane. However, transients shorten considerably in a PEMFC with a fully humidified membrane. Despite that diffusion of species in the electrodes has little effect in the transient response, it leads to sudden considerable overshoots in the output of the system.

Humidification control of inlet air is observed to be essential for a PEMFC especially working at varying pressures. For the conventional design it is observed that if the humidity is controlled, not only higher output power is maintained, but also longer transients due to water transport are prevented significantly.

The effect of inlet air humidity on the system response to a step current density is studied for conventional design. It is observed that dynamic responses of cell voltage for 100%, 50% and 0% humidified air vary substantially due to the reservoir effect of the membrane such that for the fully humidified case membrane releases water whereas for the other cases it uptakes water.

For the interdigitated case transient simulations regarding the ‘hot’ startups of the system are carried out. It was concluded that to avoid overshoots and longer transients

in the response, compressor should be turned on initially to provide enough air flow at the cathode, after which the cell might be loaded.

Furthermore, system responses concerning the failures in the auxiliary components are discussed for interdigitated case. In the presence of a malfunction in the air supply system such that the pressure of the inlet channel drops, up to 80% of the steady-state undershoots are observed in the system response. Moreover, water produced during the reaction would leave the cathode also from the inlet. Finally, a failure in the humidity control system is taken into consideration and a PEMFC employing the counterflow is found to be somewhat less susceptible to failures of this peripheral subsystem.

Future Work and Recommendations

Although the model results are consistent with the published data found in the literature, a rigorous model validation is needed with the experimental data. The fitting parameters, exchange current density and the mass transfer coefficient may be estimated through the experiments to increase the validity of the model. Also, for the completeness of the model's validity agreement of the polarization data may not be sufficient. Additionally, reactant concentration distributions obtained from the model should be validated by the data taken from in-situ measurements. Transient results should also be verified with the experiments conducted by a test station.

Admittedly, the model is far from demonstrating the realistic physical condition for higher current densities, which is governed by the condensation and evaporation in the electrodes, when the partial pressure of water is above its saturation value. Thus, the model results are limited with the water activity which is below one. To cover the governing phenomenon in the fuel cell with a better perspective, multiphase flow and phase transition should be included in the model. Multiphase mixture (M^2) formulation of [50] may be implemented into model so that the transport of liquid water and the effects such as flooding can be studied. The M^2 idea has been used in several studies [29], [36] and [49].

The model developed in this study is isothermal. However, studying the thermal effects in the fuel cell operation is very important because the life time of the membrane, performance of the cell and transients of the system all depend on

temperature. Including energy balance into the equation system will undoubtedly be insightful for the operational aspects of fuel cell.

The geometry modeled is a small cross-section of the MEA. Whole cross-section of the MEA with the entire flow fields can be modeled in order to observe the non-homogeneity of the distributions over the fuel cell.

REFERENCES

[1] Amali, S., Rolston, D.E., Yamaguchi, T., "Organic Chemicals in the Environment: Transient Multicomponent Gas-Phase Transport of Volatile Organic Chemicals in Porous Media" *Journal of Environmental Quality,* 25, 1041–1047, **1996.**

[2] Bard, A.J., Faulkner, L.R., "Electrochemical Methods", Wiley, New York, **1980.**

[3] Berg, P., Promislow, K., St. Pierre, J., Stumper, J., Wetton, B., "Water Management in PEM Fuel Cells", *Journal of Electrochemical Society*, 151, A341-A353, **2004.**

[4] Bernardi, D.M., Verbrugge, M.W., "Mathematical Model of Gas Diffusion Electrode Bonded to a Polymer Electrolyte", *AIChE J.*, 37(8), 1151–1163, **1991.**

[5] Bernardi, D.M., Verbrugge, M.W., "A Mathematical Model of the Solid-Polymer-Electrolyte Fuel Cell", *Journal of Electrochemical Society*, 139(9), **1992.**

[6] Berning, T., Lu D.M., Djilali, N., "Three-Dimensional Computational Analysis of Transport Phenomena in A PEM Fuel Cell", *Journal of Power Sources*, 106**, 2002**.

[7] Bird, R.B., Stewart, W.E., Lightfoot, E.N., "Transport Phenomena", Wiley, New York, **1960**.

[8] Bossell, U., "The Birth of the Fuel Cell 1835 – 1845", Switzerland,

[9] Cropper, M., "Fuel Cell Market Survey: Portable Applications", Prepared for Fuel Cell Today, 18 September **2002**

[10] Curtiss, C. F., Hirschfelder, J.O., *J. Chem. Phys.*, 17, 550-555, **1949.**

[11] Curtiss, C.F., Bird, R.B., "Multicomponent Diffusion", *Ind. Eng. Chem. Res.* 38, 2515-2522, **1999**.

[12] Davis, T., UMFPACK

[13] Deuflhard, P., "A Modified Newton Method for the Solution of Illconditioned Systems of Nonlinear Equations with Application to Multiple Shooting", *Numerical Mathematics*, 22, 289-315, **1974.**

[14] Dutta S., Shimpalee, S., Van Zee, J.W., "Numerical Prediction of Mass-Exchange between Cathode and Anode Channels in a PEM Fuel Cell", *International Journal of Heat and Mass Transfer*, 44, 2029-2042, **2001**.

[15] Fales, J.L., Vandeborough N.E., "The Influence of Ionomer Channel Geometry on Ionomer Transport", *Electrochemical Society Proceedings*, 86(13), 179-191, **1986**.

[16] FEMLAB 3.1 User Guide, COMSOL Inc., Burlington, MA, **2004**.

[17] Fuller, T.F., Newman, J., "Water and Thermal Management in Solid-Polymer-Electrolyte Fuel Cells", *Journal of Electrochemical Society*, 140(5), **1993**.

[18] Gelfi, G., Pukrushpan, J., Stefanopoulou, A.G., Peng, H., "Dynamics and Control of Low and High Pressure Fuel Cells", *IEEE American Control Conference Proceedings*, **2003**.

[19] Genevey, D.B., "Transient Model of Heat, Mass, and Charge Transfer as well as Electrochemistry in the Cathode Catalyst Layer of a PEMFC", MSc Thesis, Virginia Polytechnic Institute and State University, Blacksburg, Virginia, **2001**.

[20] Guvelioglu, G.H., Stenger H.G., "Computational Fluid Dynamics Modeling of Polymer Electrolyte Membrane Fuel Cells", *Journal of Power Sources*, (Article in Press by the time this thesis is written)

[21] Hamann, CH., Hamnett, A., Vielstich, W., “Electrochemistry”, Wiley-VCH, **1998.**

[22] He, W., Lin, G., Nguyen, T.V., “Diagnostic Tool to Detect Electrode Flooding in PEM Fuel Cells”, *AIChE Journal*, 49(12), 3221-3228, **2003**.

[23] He, W., Yi, J.S., Nguyen T.V., “Two-Phase Flow Model of the Cathode of PEM Fuel Cells Using Interdigitated Flow Fields”, *AIChE Journal*, 46(10)**,** 2053-2064, **2000**.

[24] Hu, M., Gu, A., Wang, M., Zhu, X., Yu, L., “Three Dimensional, Two Phase Flow Mathematical Model for PEM Fuel Cell, Part I. Model Development”, *Energy Conversion Management*, 45, 1861–1882, **2004**.

[25] Kazim, A., Liu, H., Forges, P., “Modeling of Performance of PEM Fuel Cells with Conventional and Interdigitated Flow Fields”, *Journal of App. Electrochemistry*, 29, 1409-1416, **1999**.

[26] Kenna, J., Nguyen, T.V., Promislow, K., Wetton, B., Presentation in Computational Fuel Cell Dynamics-II Meeting, April 19 - 24, **2003**.

[27] Krishna, R., "Problems and Pitfalls in the Use of the Fick Formulation for Intraparticle Diffusion”. *Chemical Engineering Science*, 48(5), 845–861, **1993**

[28] Marr, C., Li, X., “Composition and Performance Modeling of Catalyst Layer in a Proton Exchange Membrane Fuel Cell”, *Journal Of Power Sources*, 77, 17–27, **1999**.

[29] Mazumder, S., Cole, J.V., *Journal of Electrochemical Society*, 150, A1510, **2003**.

[30] Natarajan D., Nguyen, T.V., “A Two-Dimensional, Two-Phase, Multicomponent, Transient Mode for the Cathode of a Proton Exchange Membrane Fuel Cell Using Conventional Gas Distributors”, *Journal of Electrochemical Society*, 148(12), **2001**.

[31] Nguyen, P.T., "A Three-Dimensional Computational Model of PEM Fuel Cell with Serpentine Gas Channels", MSc Thesis, University of Victoria, **2003**.

[32] Nguyen, P.T., Berning, T., Djilali, N., "Computational Model Of A PEM Fuel Cell With Serpentine Gas Flow Channels," *Journal Of Power Sources,* 130**,** 14–157, **2004**.

[33] Nguyen T.V., White R.V., "A Water and Heat Management Model For Proton Exchange Membrane Fuel Cells", *Journal of Electrochemical Society*, 140(8), 2178-2186, **1993**.

[34] Panik, F., "Fuel Cells in Vehicle Applications in Cars – Bringing the Future Closer", *Journal of Power Sources*, 71, 36-38, **1998**.

[35] Parthasarathy, A., Srinivasan S., Appleby, A.J., "Temperature Dependence of the Electrode Kinetics of Oxygen Reduction at the Platinum/Nafion Interface - A Microelectrode Investigation", *Journal of Electrochemical Society*, 139, 2530–2537, **1992**.

[36] Pasaogullari, U., Wang, C.Y., "Two-Phase Modeling and Flooding Prediction of Polymer Electrolyte Fuel Cells", *Journal of the Electrochemical Society*, 152 (2) A380-A390, **2005**

[37] Pukrushpan, J., "Modeling and Control of Fuel Cell Systems and Fuel Processors", PhD dissertation, University of Michigan, Ann Arbor, 2003

[38] Pukrushpan, J., Peng, H., Stefanopoulou, A.G., "Control-Oriented Modeling and Analysis for Automotive Fuel Cell Systems*", Journal of Dynamic Systems, Measurement, and Control,* 126, 14-25, **2004**.

[39] Pukrushpan, J., Stefanopoulou, A.G., Peng, H., "Simulation and Analysis of Transient Fuel Cell System Performance Based on a Dynamic Reactant Flow Model", *Proceedings of IMECE*, **2002**.

[40] Rajashekera, K., "Propulsion System Strategies for Fuel Cell Vehicles", *SAE Paper,* 2000-01-0369.

[41] Rastler, D., "Fuel Cells For A Distributed Power market", Presentation at the Seventh Grove Fuel Cell Symposium, London, UK, 11 – 13 September **2001**.

[42] Reid, R.C., Prausnitz, J.M., Poling, B.E., "The Properties of Gases and Liquids", 3rd Edition, McGraw-Hill, New York, **1987**.

[43] Sivertsen, B.R., Djilali, N., "CFD-Based Modeling of Proton Exchange Membrane Fuel Cells", *Journal of Power Sources*, 141, 65–78, **2005**.

[44] Springer T.E., Zawodzinski T.A., Gottesfeld S., "Polymer Electrolyte Fuel Cell Model", *Journal Of Electrochemical Society*, 138(8), 2334-2342, **1991**.

[45] Stockie J.M., Promislow K., Wetton B.R., "A Finite Volume Method for Multicomponent Gas Transport in a Porous Fuel Cell Electrode", *International Journal for Numerical Methods in Fluids*, 41, 577-599, **2003**.

[46] Ticianelli, E.A., Derouin, C.R., Srinivasan, S., "Localization Of Platinum in Low Catalyst Loading Electrodes To Attain High Power Densities in SPE Fuel Cells", *Journal Of Electroanalytic Chemistry*, 251, 275–295, **1988**.

[47] Thomas, S., Zalowitz, M., "Fuel Cells – Green Power", Los Alamos National Laboratory, Los Alamos, NM, **1999**,

[48] Um, S., Wang, C.Y., Chen, K.S., "Computational Fluid Dynamics Modeling of Proton Exchange Membrane Fuel Cells", *Journal of Electrochemical Society*, 147(12), **2000**.

[49] Wang, Z.H., Wang, C.Y., Chen, K.S., *Journal of Power Sources*, 94, 40, **2001**.

[50] Wang, C.Y., Cheng, P., Advanced Heat Transfer, 30, 93, 1997.

[51] Wang, L., Liu, H., "Performance Studies Of PEM Fuel Cells with Interdigitated Flow Fields", *Journal of Power Sources*, 134, 185–196, **2004**.

[52] Wang, Y., Wang, C.Y., "Transient Analysis of Polymer Electrolyte Fuel Cells", *Electrochimica Acta*, 50**,** 1307-1315, **2005**.

[53] West, A.C., Fuller, T.F., "Influence of Rib Spacing in Proton-Exchange Membrane Electrode Assemblies", *Journal of Applied Electrochemistry*, 26**,** 557-565, **1996**.

[54] Yerramalla, S., Davari, A., Feliachi, A., Biswas, T., "Modeling and Simulation of the Dynamic Behavior of A Polymer Electrolyte Membrane Fuel Cell", *Journal of Power Sources*, 124, 104-113, **2003**.

[55] Yi, J.S., Nguyen, T.V., "An Along the Channel Model for Proton Exchange Membrane Fuel Cells", *Journal of Electrochemical Society*, 145(4), 1149-1159, **1998**.

[56] "Fuel Cell Handbook, 5th Edition", Report Prepared By EG&G Services, Parsons, Inc. And Science Applications International Corporation for the U.S. Department Of Energy, National Energy Technology Laboratory, October **2000**

[57] "Technology Characterization: Fuel Cells", Report Prepared By Energy Nexus Group For Environmental Protection Agency Climate Protection Partnership Division, Washington, DC, April **2002**.

[58] "2000 and Fuel Cells; Power for the 21st Century", US Dept of Energy, **2004**

[59] http://www.eere.energy.gov

[60] http://www.members.tripod.com/trungvannguyen